LIQUID-FEED FLAME SPRAY PYROLYSIS SYNTHESIS OF OXIDE NANOPOWDERS FOR THE PROCESSING OF CERAMIC COMPOSITES

by

Nathan John Taylor

A dissertation submitted in partial fulfillment
of the requirements of the degree of
Doctor of Philosophy
(Materials Science and Engineering)
in The University of Michigan
2015

Doctoral Committee:

Professor Richard M. Laine, Chair
Associate Professor Bart M. Bartlett
Professor John W. Halloran
Associate Professor Pierre F. Poudeu-Poudeu

Dedication

To my parents, family, and friends.

Acknowledgements

First I must acknowledge the support of my advisor, Rick Laine, who mentored me since I joined his group as an undergraduate. Without Rick's support and guidance and support I would not be here today. I'd also like to thank Professors Bart Bartlett, John Halloran, and Pierre Poudeu for helpful feedback and serving on my committee.

I must acknowledge the support of my colleagues in the Laine group, including Andrew Pottebaum, Dr. Joseph Furgal, and Eongyu Yi. I'd like to extend special thanks to my numerous undergraduate researchers, especially Sandra Stangeland-Molo and Catherine Haslam. I also would like to acknowledge my wonderful parents, family, and friends. This journey was only possible with their support.

Table of Contents

List of Figures

List of Tables

Abstract

In the liquid-feed flame spray pyrolysis (LF-FSP) process, alcohol solutions of metalloorganic precursors are aerosolized by O_2 and combusted. The metal oxide combustion products are rapidly quenched (< 10 ms) from flame temperatures of 1500°C to temperatures $< 400°$ C, limiting particle growth. The resulting nanopowders are typically agglomerated but unaggregated.

Our first studies included the production of yttrium aluminum garnet, $Y_3Al_5O_{12}$ (YAG), tubes which we extruded from a thermoplastic/ceramic blend. We approached YAG from two processing schemes, nanopowders with the exact chemical composition, and mixed single metal-oxide Y_2O_3 and Al_2O_3 nanopowders. At equivalent final densities, we found finer grain sizes in the from the mixed Y_2O_3 and Al_2O_3 nanopowders, which was attributed to densification occurring before full transformation to the YAG phase.

The enhanced densification in production of pure YAG from the reactive sintering process led us to produce composites in the $YAG/\alpha\text{-}Al_2O_3$ system. Again, we used nanopowders with the exact composite composition and compared the sintering and final microstructures to mixed single metal oxide nanopowders. Finally, a third Y_2O_3 stabilized ZrO_2 (YSZ) phase was added to further refine grain sizes using the same two processing approaches. In a separate study, single-phase metastable Al_2O_3 rich spinels with the composition $MO \cdot 3Al_2O_3$ where M = Mg, Ni, and Co were sintered to produce dense $MAl_2O_4/\alpha\text{-}Al_2O_3$ composites. All of these studies provide a test of the bottom-up approach; that is, how the initial length scale of mixing affects the final composite microstructure. Overall, the length scale of mixing is highly dependent upon the specific oxide composites

studied. This work provides a processing framework to be adopted by other researchers to further refine microstructural size.

Lastly, LF-FSP flame temperatures were mapped using different alcohols with different heats of combustion: methanol, ethanol, 1-propanol, and n-butanol. The effect of different alcohols on particle size and phase was determined through studies on Al_2O_3, Y_2O_3 and TiO_2 nanopowders. The final studies describe the morphology of composite nanopowders produced in the WO_3-TiO_2 and CuO-TiO_2 systems. The composite nanopowders have novel morphology, and may offer novel electronic, optical, or catalytic properties.

<div align="center">

Chapter 1

Introduction

</div>

1.1   Spray pyrolysis production of nanopowders

Spray pyrolysis has been described as dating back to cavemen painting cave walls with the soot formed from fires.[1] Most notably, the 1950's brought the introduction of the chloride process for TiO_2 pigment production, replacing the sulphate process.[1] In the chloride process, TiO_2 is dissolved in hydrochloric acid, and the resulting $TiCl_4$ is purified by distillation.[2,3] The purified TiO_2 is fed into premixed H_2/O_2 flames, producing TiO_2 which collects on the walls of a hot reactor or is collected by filtration. The combustion process produces HCl gas which is scrubbed from the gas feed at high efficiencies. By the same process, large amounts of SiO_2, ZnO, and Al_2O_3 are also produced annually. Even UO_2 is produced by combustion of UF_6 in an oxidizing flame.[1] The chloride process is described as a gas-to-particle spray pyrolysis process, in which the molecular precursor is combusted to the gas phase before nucleating and growing through coalescence processes. The chloride process can produce primary particles < 50 nm in size, but the high reactor temperatures allow for sintering of the particles to produce aggregates several hundred nanometers in size.[1] Mixed-metal oxides are difficult to produce by the chloride process, as the disparate hydrolysis rates of different metal chlorides leads to inhomogeneous particles.

Ulrich conducted some of the first serious investigations of gas-to-particle flame spray pyrolysis in the formation of fumed SiO_2 from $SiCl_4$.[4] Ulrich determined that the particle growth rate was a function of three factors: chemical reaction, nucleation, and Brownian motion. Using thermochemical data for SiO_2, Ulrich showed the critical nucleation radius at flame temperatures of 2000 K was less than that of a single molecule. This would suggest that any multimolecular species is thermodynamically stable in the flame. Ulrich further reasoned that the free energy of reaction of $SiCl_4$ (-19 kJ/mol) with H_2 and O_2 to create a single molecule of gas phase SiO_2 could not account for the exothermic nature of the combustion reaction, which must be a consequence of the production of condensation of SiO_2 (-586 kJ/mol) produced in the flame. Since any multimolecular species created by condensation of SiO_2 are above the critical nucleation radius, they are thermodynamically stable. As a consequence, no distinction can be made between nucleation and chemical reaction in the flame. In a follow-up publication, Ulrich et al sampled particles from the flame, finding that the particle growth could be well modeled using a simple Brownian collision-coalescence growth model.[5]

Comprehensive reviews have been provided by Pratsinis,[6] Stark and Pratsinis,[7] Pratsinis and Vemury,[8] Wooldridge,[9] and Roth.[10] Further theoretical and experimental studies have shown particle size can be described by a characteristic collision time, coalescence time, and residence time.[11,12,13,14,15] The collision time is the average time required for two particles to collide in the flame. The collision time is directly correlated to the concentration of particles in flame. The coalescence time is the time required for two particles to form a single particle. This reaction can occur through viscous flow or by solid-state sintering of the particles. When the collision and coalescence times are equal,

colliding particles do not form a single particle but instead are bound into fractal structures. If bound weakly by electrostatic forces, these groups of particles are called agglomerates. If bound physically by sintering, the groups of particles are called aggregates. The residence time is the time spent by particles in the flame. At long residence times beyond the coalescence time, aggregates are likely. At shorter residence times, the particles are quenched before sintering, favoring agglomerate formation. Aggregates are preferred for some applications such as fumed silica for integration into elastomers,[6] but unaggregated powders are preferred for powder processing.

1.1.1 Liquid-feed flame spray pyrolysis (LF-FSP)

Spray pyrolysis, as developed at the University of Michigan is described as liquid-feed flame spray pyrolysis. In LF-FSP, metalloorganic precursors are dissolved in alcohol solutions at <5 wt% ceramic loading. The alcohol solutions are fed into a simple spray nozzle and aerosolized with O_2. Pilot torches combust the fine atomized spray approximately 50 mm downstream of the spray nozzle. The nozzle design and pump flow rate operate such that the flame front velocity is not faster than the velocity of the atomized fuel flow, preventing the flame from "flashing" back to the headplate. A separate oxygen "shield gas" stream is fed from four nozzles around the flame. This O_2 ensures complete combustion of the organics. After complete combustion, the product moves from the combustion chamber into aluminum tubes with a pseudo 10 kV DC potential running "wire-in-tube" electrostatic precipitators. This potential drives a combined thermo/electrophoretic deposition of the nanoparticles onto the inner and outer electrode surfaces.

Unlike other spray pyrolysis techniques, in LF-FSP, the precursor is dissolved in the fuel itself. Like the chloride process, LF-FSP is a gas-to-particle flame spray pyrolysis method. The relatively uniform combustion rates lends LF-FSP to the production of mixed-metal oxides. Precursors are typically metal carboxylates or alkoxides. The most common precursors are propionate salts, which are typically produced from the reaction of metal hydroxides or carbonates with the propionic acid. Acetate salts are more available commercially but have lower solubility in alcohols, so are used sparingly or for doping. A second class of precursors are metal acetylacetonate salts, which also have limited solubility in alcohols. A third class of precursors are "atrane" molecules with three five member rings.[16] The most common atranes for LF-FSP are synthesized through the reaction of triethanolamine with SiO_2, TiO_2, or Al_2O_3.[17] These compounds are more easily synthesized from the room temperature reaction of triethanolamine with metal alkoxides.[18]

LF-FSP as developed in the Laine group at the University of Michigan have produced nanopowders such as Al_2O_3,[19] $MgAl_2O_4$,[20] SiO_2-Al_2O_3,[21] TiO_2,[22] TiO_2-Al_2O_3,[23] CoO-Al_2O_3,[24] NiO-Al_2O_3,[25] $Y_3Al_5O_{12}$,[26] upconverting Y_2O_3 phosphors,[27] CeO_2-Al_2O_3,[28] ZrO_2-Al_2O_3,[29] $BaTiO_3$,[30] and $Li_{1.7}Al_{0.3}Al_{1.7}Si_{0.4}P_{2.6}O_{12}$[31] among others. Through these studies, LF-FSP has demonstrated the production high quality metal oxide and mixed-metal oxide nanopowders that are agglomerated but unaggregated, making them ideal for ceramic processing. Notably, we find that LF-FSP often produces metastable "kinetic" phases that are outside the thermodynamic phase diagram.[19,32] These phases are formed because the particle flame residence times (< 100 ms) are insufficient to form the thermodynamic phase, and/or stabilization of kinetic phases at fine particle sizes.[33,34]

1.1.2 Fine grained ceramics

With the development of nanopowder synthesis techniques came efforts to produce monolithic ceramics with grain sizes far below that of traditional bulk scale techniques. Nanograined ceramics have improved mechanical properties, such as strength, hardness, and toughness.[35,36] Other nanograined ceramics have applications such as ballistic armor or transparency not achievable by traditional techniques.[37] One advantage in sintering of nanopowders is the reduction in sintering temperature when compared to micron sized powders.[38,39] Despite these efforts, obtaining fine grained < 500 nm dense ceramic materials by typical pressureless sintering methods has proven difficult.[40,41] Processing of nanopowders is often challenging for the reasons explained below.

One major consideration in the sintering of nanopowders is the degree of agglomeration of the starting powder. Agglomerates in the nanopowder starting material pack poorly compared to bulk materials, and the high surface areas of nanopowders leads to greater interparticle friction.[42] As a result, nanopowders require higher forming pressures to reach adequate green densities. For fine agglomerates, the primary green body pores are intraagglomerate pores, which can have relatively uniform pore size distributions, leading to the best sintering results.[43,44] The presence of aggregates is deleterious to sintering, as interaggregate pores are difficult to remove during the sintering process.[45]

Briefly, sintering can be divided into three distinct stages. In the first phase of sintering, surface diffusion along particle surfaces begins to neck particles that are touching. The particles may also rotate to align crystallographic directions with adjacent particles.[39,46] The second stage of sintering is where the bulk of densification occurs. In the second stage, a 3D continuous pore network is formed. In the third stage of sintering, the continuous pore

network collapses, producing isolated spherical pores. Further sintering eliminates final porosity, but the diffusional processes coincidentally cause grain growth. One technique for avoiding grain growth while eliminating closed porosity is hot isostatic pressing (HIPing). In HIPing, the samples are heated to temperatures below which grain growth is active, and gas pressure (typically 200 MPa) provides a driving force for the elimination of porosity.[43] Recently, spark plasma sintering has emerged as a sintering technique for nanopowders with relatively little grain growth.[47] Briefly, in SPS, pressure and a pulsed DC current are applied to samples. The rapid heating promotes densification without significant coarsening.

1.2 Ceramic composites

The field of ceramic/ceramic composites covers multiple types of composite materials most of which are strengthened by fibers or whiskers. Roy and Komarneni were among the first to use sol-gel chemistry to produce diphasic materials and the field of nanocomposite oxide materials.[48,49,50] Nomenclature established by Niihara defines four types of nanocomposites: intra, inter, intra/inter, and nano/nano.[51] The inter and intra nanocomposites describe a fine secondary phase located either inside the primary phase grains or at grain boundaries, respectively. The intra/inter nanocomposite is a mixed case of the two. Nano/nano composites consist of two or more phases that exist as discrete grains nearly the same size. The work described in this dissertation focuses on the production of dense nano/nano composites with well dispersed phases.

Early investigations of composites with duplex, or two-phase, microstructures determined that sintering to obtain fine-grained, dense composites is best achieved by pinning grain boundary migration using a second phase.[52] In single phase materials,

diffusion along grain boundaries or through the lattice can accommodate grain boundary migration or coarsening of the microstructure.[53] French et al found the grain growth rate constant in equivolumetric Al_2O_3-c-ZrO_2 was 160X smaller than that of undoped Al_2O_3 at 1650°C.[54] As a result, French et al reported grain sizes were reduced from 13 to 1.4 μm upon addition of 50 vol% Al_2O_3 to c-ZrO_2.[54] French and also postulated that diffusion occurs along interphase boundaries in high composites with high interconnectivity of phases.[54] As more phases are added, they present barriers to diffusion accommodating grain boundary migration.[53] Men and Mecartney determined that in an equivolumetric four-phase composite with perfect mixing, a grain of a single phase would have an adjacent grain of the same material.[53] Multi-phase ceramic nano/nano composites have applications as structural materials,[55,56] ferroelectrics,[57] or IR windows.[58] Kim et al showed superplastic strains up to 1000% in a three phase Al_2O_3-$MgAl_2O_4$-ZrO_2 composite, which is another application for multi-phase nanoceramics.[59]

The bottom-up approach to materials synthesis states that the best macroscopic properties will be obtained from materials in which the synthesis is controlled from the finest possible length scale.[60,61,62,63] In this dissertation, the majority of work focuses on expanding the bottom-up approach to the processing of two and three-phase ceramic composites. Our processing studies focused on the degree, or length scale of mixing. In one approach, nanopowders were produced by LF-FSP with the exact composition of the final composite. In the second approach, single metal oxide nanopowders or a mixed metal oxide and single metal oxide nanopowder were mixed by ball milling to produce the same composition composite. In the exact composition studies, or nanocomposite nanopowders, the stoichiometry is assumed to be contained within a single particle (< 50 nm). Further

discussion in Chapter 5 provides more data on the structure of the as-produced nanocomposite nanopowders. In the ball milled, or mixed nanopowder approach, the separation of particles with the overall composite stoichiometry is likely closer to the agglomerate size, or between 100-800 nm. At two length scales of mixing, we examine the sintering of the composites and determine what effect, if any, the length scale of mixing has on the final microstructure.

1.3 Common LF-FSP oxides

Here we provide an introduction to some oxides used in multiple chapters in this dissertation. One of these oxides, $Y_3Al_5O_{12}$ (YAG), having a garnet structure, is a technologically important laser host material. Nd and Er doped YAG are widely used solid-state laser materials.[64] Ce doped YAG is a phosphor for white LEDs.[65] As an optical window material, YAG shows high transparency across the visible spectrum.[66] YAG has a creep rate an order of magnitude lower than α-Al_2O_3 along with acceptable thermal shock resistance from operating temperatures > 1000° C.[67,68] For this reason it is a possible replacement candidate for polycrystalline alumina as a high-temperature window material, such as for high-pressure sodium vapor lamps. LF-FSP production of YAG produces a hexagonal $YAlO_3$ phase that transforms to YAG at temperatures as low as 800° C.[26] LF-FSP production of YAG has been previously described.[26]

LF-FSP production of Al_2O_3 nanopowders produces the transition Al_2O_3 phases: δ, δ*, and γ-Al_2O_3.[69] Most alumina nanopowder synthesis techniques produce a mixture of transition Al_2O_3 phases. All transition phases are based on FCC oxygen packing and can be idealized as lattice distortions of the cubic spinel-type γ-Al_2O_3 based on oxygen vacancy positions required to maintain the stoichiometry of the spinel structure.[69] These transition

Al_2O_3 powders transform with the general transformation sequence $\gamma \rightarrow \delta \rightarrow \theta \rightarrow \alpha\text{-}Al_2O_3$, with the $\theta \rightarrow \alpha$ transformation occurring around 1000-1200° C.[69] The transformation of the transition aluminas to $\alpha\text{-}Al_2O_3$ has a high energy barrier to nucleation, which once activated, leads to excessive growth into vermicular or "worm-like" grains.[70,71] These vermicular grains prevent densification at low temperatures, leading to difficulty in producing fine grained $\alpha\text{-}Al_2O_3$ from nanopowders.[72]

1.4   Scope of dissertation

LF-FSP provides access to single and mixed-metal oxide nanopowders well suited for processing into dense ceramic monoliths. Since the synthesis parameters of LF-FSP can be fixed, the size, chemical homogeneity, and degree of agglomeration are relatively constant. The fixed synthesis parameters allow us to focus on the formation of materials from both single-particle and multi-particle processing approaches, as discussed above.

Chapter 2 provides relevant experimental information for LF-FSP powder production and processing, as well as descriptions of characterization methods, including: X-ray diffraction, BET surface area analysis, dilatometry, thermogravimetric analysis, and electron microscopy.

Chapter 3 describes the development of thermoplastic/ceramic extrusion techniques capable of producing 10 mm tubes that retain dimensional uniformity throughout the sintering process. Next, the sintering of YAG tubes is examined through two processing approaches, reactive sintering of Y_2O_3-Al_2O_3 nanopowders and sintering of nanopowders having a $Y_3Al_5O_{12}$ composition.

Chapter 4 describes an extension of the two sintering approaches used in Chapter 3 to now approach three composite compositions in the YAG/α-Al$_2$O$_3$ two-phase system. Discussion specifically focuses on the effect of the processing approach on the final microstructures.

Chapter 5 is again an extension of the two processing approaches, mixed single phase nanoparticles, and nanocomposite nanoparticles having the final composition contained within a single particle. In Chapter 5, ZrO$_2$ is added to YAG/α-Al$_2$O$_3$ to produce a ternary phase composite. The effects of the two processing approach as well as the addition of ZrO$_2$ are discussed.

Chapter 6 describes dense MAl$_2$O$_4$/α-Al$_2$O$_3$ composites where M = Ni, Mg, or Co, where composites are produced from mixed nano-Al$_2$O$_3$ and MAl$_2$O$_4$ nanopowders or from single-phase metastable Al$_2$O$_3$ rich spinel particles.

Chapter 7 provides results and discussion on LF-FSP particle formation. First, flame temperatures are measured and the effect of flame length on particle size and crystalline phase is tested on Al$_2$O$_3$, TiO$_2$, and Y$_2$O$_3$ nanopowders. Next, LF-FSP studies on nanopowders in the immiscible oxide systems WO$_3$-TiO$_2$ and CuO-TiO$_2$ are presented, with focus on the as-produced particle morphologies.

Chapter 8 provides general conclusions of the work presented in this dissertation as well as recommendations for future work.

References:

[1] G.D. Ulrich, "Flame synthesis of fine particles," *Chem. Eng. News Archive*, **62** [32] 22–29 (1984).

[2] W.S. Clabaugh, R.T. Leslie, and R. Gilchrist, "Preparation of Titanium Tetrachloride of High Purity," *J. Res. Nat. Bur. Stand.*, **55** [5] 261-264 (1955).

[3] C.H. Gorski, "Preparation of Titanium Tetrachloride from Rutile," *Journal of Metals*, **3** [2] 131-133 (1977).

[4] G.D. Ulrich, "Theory of Particle Formation and Growth in Oxide Synthesis Flames," *Combust. Sci. Technol.*, **4** [1] 47–57 (1971).

[5] G.D. Ulrich, B.A. Milnes, and N.S. Subramanian, "Particle Growth in Flames. II: Experimental Results for Silica Particles," *Combust. Sci. Technol.*, **14** [4-6] 243–249 (1976).

[6] S.E. Pratsinis, "Flame aerosol synthesis of ceramic powders," *Pro. Energ. Combust. Sci.*, **24** [3] 197–219 (1998).

[7] W.J. Stark and S.E. Pratsinis, "Aerosol flame reactors for manufacture of nanoparticles," *Powder Technol.*, **126** [2] 103–108 (2002).

[8] S.E. Pratsinis and S. Vemury, "Particle formation in gases: A review," *Powder Technol.*, **88** [3] 267–273 (1996).

[9] M.S. Wooldridge, "Gas-phase combustion synthesis of particles," *Progress in Energy and Combustion Science*, **24** [1] 63–87 (1998).

[10] P. Roth, "Particle synthesis in flames," *Proc. Combust. Inst.*, **31** [2] 1773–1788 (2007).

[11] D.E. Rosner, "Flame Synthesis of Valuable Nanoparticles: Recent Progress/Current Needs in Areas of Rate Laws, Population Dynamics, and Characterization," *Ind. Eng. Chem. Res.*, **44** [16] 6045–6055 (2005).

[12] L. Mädler, H.K. Kammler, R. Mueller, and S.E. Pratsinis, "Controlled synthesis of nanostructured particles by flame spray pyrolysis," *J. Aerosol Sci.*, **33** [2] 369–389 (2002).

[13] R.P. Andres, "Homogeneous Nucleation from the Vapor Phase," *Ind. Eng. Chem.*, **57** [10] 24–31 (1965).

[14] W. Koch and S.K. Friedlander, "Particle Growth by Coalescence and Agglomeration," *Part. Part. Syst. Charact.*, **8** [1-4] 86–89 (1991).

[15] W. Koch and S.K. Friedlander, "The effect of particle coalescence on the surface area of a coagulating aerosol," *J. Coll. and Interf. Sci.*, **140** [2] 419–427 (1990).

[16] J.G. Verkade, "Main group atranes: chemical and structural features," *Coord. Chem. Rev.*, **137** 233–295 (1994).

[17] R.M. Laine, D.R. Treadwell, B.L. Mueller, C.R. Bickmore, K.F. Waldner, and T.R. Hinklin, "Processable aluminosilicate alkoxide precursors from metal oxides and hydroxides. The oxide one-pot synthesis process," *J. Mater. Chem.*, **6** [8] 1441–1443 (1996).

[18] K. Tadanaga, S. Ito, T. Minami, and N. Tohge, "Precursor structure and microstructure of Al2O3 xerogels prepared from aluminum-tri-sec-butoxide chemically modified with mono-, di-, tri-ethanolamines," *J. Non-Cryst. Sol.*, **201** [3] 231–236 (1996).

[19] T. Hinklin, B. Toury, C. Gervais, F. Babonneau, J.J. Gislason, R.W. Morton, and R.M. Laine, "Liquid-Feed Flame Spray Pyrolysis of Metalloorganic and Inorganic Alumina Sources in the Production of Nanoalumina Powders," *Chem. Mater.*, **16** [1] 21–30 (2004).

[20] C.R. Bickmore, K.F. Waldner, D.R. Treadwell, and R.M. Laine, "Ultrafine Spinel Powders by Flame Spray Pyrolysis of a Magnesium Aluminum Double Alkoxide," *J. Amer. Ceram. Soc.*, **79** [5] 1419–1423 (1996).

[21] R. Baranwal, M.P. Villar, R. Garcia, and R.M. Laine, "Flame Spray Pyrolysis of Precursors as a Route to Nano-mullite Powder: Powder Characterization and Sintering Behavior," *J. Amer. Ceram. Soc.*, **84** [5] 951–961 (2001).

[22] C.R. Bickmore, K.F. Waldner, R. Baranwal, T. Hinklin, D.R. Treadwell, and R.M. Laine, "Ultrafine titania by flame spray pyrolysis of a titanatrane complex," *J. Eur. Ceram. Soc.*, **18** [4] 287–297 (1998).

[23] S. Kim, J.J. Gislason, R.W. Morton, X.Q. Pan, H.P. Sun, and R.M. Laine, "Liquid-Feed Flame Spray Pyrolysis of Nanopowders in the Alumina−Titania System," *Chem. Mater.*, **16** [12] 2336–2343 (2004).

[24] J. Azurdia, J. Marchal, and R.M. Laine, "Synthesis and Characterization of Mixed-Metal Oxide Nanopowders Along the CoO_x–Al_2O_3 Tie Line Using Liquid-Feed Flame Spray Pyrolysis," *J. Amer. Ceram. Soc.*, **89** [9] 2749–2756 (2006).

[25] J.A. Azurdia, J. Marchal, P. Shea, H. Sun, X.Q. Pan, and R.M. Laine, "Liquid-Feed Flame Spray Pyrolysis as a Method of Producing Mixed-Metal Oxide Nanopowders of Potential Interest as Catalytic Materials. Nanopowders along the NiO−Al_2O_3 Tie Line Including $(NiO)_{0.22}(Al_2O_3)_{0.78}$, a New Inverse Spinel Composition," *Chem. Mater.*, **18** [3] 731–739 (2006).

[26] J. Marchal, T. John, R. Baranwal, T. Hinklin, and R.M. Laine, "Yttrium Aluminum Garnet Nanopowders Produced by Liquid-Feed Flame Spray Pyrolysis (LF-FSP) of Metalloorganic Precursors," *Chem. Mater.*, **16** [5] 822–831 (2004).

[27] T.R. Hinklin, S.C. Rand, and R.M. Laine, "Transparent, Polycrystalline Upconverting Nanoceramics: Towards 3-D Displays," *Adv. Mater.*, **20** [7] 1270–1273 (2008).

[28] M. Kim, T. R. Hinklin, and R.M. Laine, "Core−shell Nanostructured Nanopowders along $(CeO_x)_x(Al_2O_3)_{1−x}$ Tie-Line by Liquid-Feed Flame Spray Pyrolysis (LF-FSP)," *Chem. Mater.*, **20** [16] 5154–5162 (2008).

[29] M. Kim and R.M. Laine, "Liquid-feed flame spray pyrolysis (LF-FSP) for combinatorial processing of nanooxide powders along the $(ZrO_2)_{(1-x)}(Al_2O_3)_x$ tie-line. Phase segregation and the formation of core-shell nanoparticles," *J. Ceram. Proc. Res.*, **8** [2] 129-136 (2007)

[30] E. Yi, J.C. Furgal, J. Azurdia, and R.M. Laine, "Roll your own − nano-nanocomposite capacitors," *J. Mater. Chem. A*, **2** [11] 3766–3775 (2014).

[31] E. Yi, W. Wang, S. Mohanty, J. Kieffer, R. Tamaki, and R.M. Laine, "Materials that can replace liquid electrolytes in Li batteries: Superionic conductivities in $Li_{1.7}Al_{0.3}Ti_{1.7}Si_{0.4}P_{2.6}O_{12}$. Processing combustion synthesized nanopowders to free standing thin films," *J. Pow. Sources*, **269** 577–588 (2014).

[32] R.M. Laine, J. Marchal, H. Sun, and X.Q. Pan, "A New $Y_3Al_5O_{12}$ Phase Produced by Liquid-Feed Flame Spray Pyrolysis (LF-FSP)," *Adv. Mater.*, **17** [7] 830–833 (2005).

[33] J.M. McHale, A. Auroux, A.J. Perrotta, and A. Navrotsky, "Surface Energies and Thermodynamic Phase Stability in Nanocrystalline Aluminas," *Science*, **277** [5327] 788–791 (1997).

[34] P. Zhang, A. Navrotsky, B. Guo, I. Kennedy, A.N. Clark, C. Lesher, and Q. Liu, "Energetics of Cubic and Monoclinic Yttrium Oxide Polymorphs: Phase Transitions, Surface Enthalpies, and Stability at the Nanoscale," *J. Phys. Chem. C*, **112** [4] 932–938 (2008).

[35] A. Krell and A. Bales, "Grain Size-Dependent Hardness of Transparent Magnesium Aluminate Spinel," *Intl. J. App. Ceram. Tech.*, **8** [5] 1108–1114 (2011).

[36] J.G. Li and X. Sun, "Synthesis and sintering behavior of a nanocrystalline α-alumina powder," *Acta Mater.*, **48** [12] 3103–3112 (2000).

[37] A. Krell, J. Klimke, and T. Hutzler, "Advanced spinel and sub-μm Al_2O_3 for transparent armour applications," *J. Eur. Ceram. Soc.*, **29** [2] 275–281 (2009).

[38] R.W. Siegel, S. Ramasamy, H. Hahn, L. Zongquan, L. Ting, and R. Gronsky, "Synthesis, characterization, and properties of nanophase TiO_2," *J. Mater. Res.*, **3** [06] 1367–1372 (1988).

[39] P. Zeng, S. Zajac, P.C. Clapp, and J.A. Rifkin, "Nanoparticle sintering simulations," *Materials Science and Engineering: A*, **252** [2] 301–306 (1998).

[40] I.-W. Chen and X.-H. Wang, "Sintering dense nanocrystalline ceramics without final-stage grain growth," *Nature*, **404** [6774] 168-171 (2000).

[41] J.A. Eastman, Y.X. Liao, A. Narayanasamy, and R.W. Siegel, "Processing and Properties of Nanophase Oxides;" in *Symposium L – Processing Science of Advanced Ceramics*. 1989.

[42] A. Mukhopadhyay and B. Basu, "Consolidation–microstructure–property relationships in bulk nanoceramics and ceramic nanocomposites: a review," *Intl. Mater. Rev.*, **52** [5] 257–288 (2007).

[43] M.J. Mayo, "Processing of nanocrystalline ceramics from ultrafine particles," *Intl. Mater. Rev.*, **41** [3] 85–115 (1996).

[44] F.F. Lange, "Sinterability of Agglomerated Powders," *J. Amer. Ceram. Soc.*, **67** [2] 83–89 (1984).

[45] M. Kitayama and J.A. Pask, "Formation and Control of Agglomerates in Alumina Powder," *J. Amer. Ceram. Soc.*, **79** [8] 2003–2011 (1996).

[46] Y.U. Wang, "Computer modeling and simulation of solid-state sintering: A phase field approach," *Acta Materialia*, **54** [4] 953–961 (2006).

[47] Z.A. Munir, U. Anselmi-Tamburini, and M. Ohyanagi, "The effect of electric field and pressure on the synthesis and consolidation of materials: A review of the spark plasma sintering method," *J. Mater. Sci.*, **41** [3] 763–777 (2006).

[48] D.W. Hoffman, R. Roy, and S. Komarneni, "Diphasic Xerogels, A New Class of Materials: Phases in the System Al_2O_3-SiO_2," *J. Amer. Ceram. Soc.*, **67** [7] 468–471 (1984).

[49] R. Roy, "Purposive Design of Nanocomposites: Entire Class of New Materials," pp. 25-32 in Materials Science Research, vol 21, *Ceramic Microstructures '86, Role of Interface*, Edited by J.A. Pask and A.G. Evans, Plenum Press, New York, NY (1987). *21*, 25.

[50] S. Komarneni, "Feature article. Nanocomposites," *J. Mater. Chem.*, **2** [12] 1219–1230 (1992).

[51] K. Niihara, A. Nakahira, and T. Sekino, "New Nanocomposite Structural Ceramics;" in *Symposium J – Nanophase and Nanocomposite Materials*. MRS Proceedings, vol 261, Edited by J.C. Parker and G.J. Thomas, Cambridge Press, Cambridge, UK 1992.

[52] A. Okada, T. Sakuma, "The Role of Zener Pinning Effect on the Grain-Growth in Al_2O_3-ZrO_2," *J. Ceram. Soc. Jpn.*, **100** [4] 382-386 1992.

[53] D. Men and M.L. Mecartney, "Superplasticity and machinability in a four-phase ceramic," *Mater.s Res. Bull.*, **47** [8] 1925–1931 (2012).

[54] J.D. French, M.P. Harmer, H.M. Chan, and G.A. Miller, "Coarsening-Resistant Dual-Phase Interprenetrating Microstructures," *J. Amer. Ceram. Soc.*, **73** [8] 2508–2510 (1990).

[55] C. Oelgardt, J. Anderson, J.G. Heinrich, and G.L. Messing, "Sintering, microstructure and mechanical properties of Al_2O_3–Y_2O_3–ZrO_2 (AYZ) eutectic composition ceramic microcomposites," *J. Eur. Ceram. Soc.*, **30** [3] 649–656 (2010).

[56] L. Gao, H.Z. Wang, J.S. Hong, H. Miyamoto, K. Miyamoto, Y. Nishikawa, and S.D.D.L. Torre, "Mechanical Properties and Microstructure of Nano-SiC–Al_2O_3 Composites Densified by Spark Plasma Sintering," *J. Eur. Ceram. Soc.*, **19** [5] 609–613 (1999).

[57] T. Nagai, H.J. Hwang, M. Yasuoka, M. Sando, and K. Niihara, "Preparation of a Barium Titanate-Dispersed-Magnesia Nanocomposite," *J. Amer. Ceram. Soc.*, **81** [2] 425–428 (1998).

[58] D.C. Harris, L.R. Cambrea, L.F. Johnson, R.T. Seaver, M. Baronowski, R. Gentilman, C. Scott Nordahl, T. Gattuso, *et al.*, "Properties of an Infrared-Transparent MgO:Y_2O_3 Nanocomposite," *J. Am. Ceram. Soc.*, **96** [12] 3828–3835 (2013).

[59] B.-N. Kim, K. Hiraga, K. Morita, and Y. Sakka, "A high-strain-rate superplastic ceramic," *Nature*, **413** [6853] 288–291 (2001).

[60] C.M. Lieber, "Nanoscale science and technology: Building a big future from small things," *MRS Bull.*, **28** [7] (2003).

[61] M. Heule, S. Vuillemin, and L.J. Gauckler, "Powder-Based Ceramic Meso- and Microscale Fabrication Processes," *Adv. Mater.*, **15** [15] 1237–1245 (2003).

[62] R. Ramaseshan, S. Sundarrajan, R. Jose, and S. Ramakrishna, "Nanostructured ceramics by electrospinning," *J. App. Phys.*, **102** [11] (2007).

[63] R. Murugavel, H.G. Walawalkar, M. Dan, H.W. Roesky, and C.N.R. Rao, "Transformations of molecules and secondary building units to materials: A bottom-up approach," *Acc. Chem. Res.*, **37** [10] 763-744 (2004).

[64] A. A. Kaminskii, "Laser crystals and ceramics: recent advances," *Laser & Photon. Rev.*, **1** [2] 93–177 (2007).

[65] M. Veith, S. Mathur, A. Kareiva, M. Jilavi, M. Zimmer, and V. Huch, "Low temperature synthesis of nanocrystalline $Y_3Al_5O_{12}$ (YAG) and Ce-doped $Y_3Al_5O_{12}$ via different sol–gel methods," *J. Mater. Chem.*, **9** [12] 3069–3079 (1999).

[66] T.A. Parthasarathy, T.-I. Mah, and K. Keller, "Creep Mechanism of Polycrystalline Yttrium Aluminum Garnet," *J. Amer. Ceram. Soc.*, **75** [7] 1756–1759 (1992).

[67] G.C. Wei, "Transparent ceramic lamp envelope materials," *J. Phys. D: Appl. Phys.*, **38** [17] 3057-3065 (2005).

[68] T.-I. Mah, T.A. Parthasarathy, and H.D. Lee, "Polycrystalline YAG; structural or functional?," *J. Ceram. Proc. Res.*, **5** [4] 369-379 (2004).

[69] I. Levin and D. Brandon, "Metastable Alumina Polymorphs: Crystal Structures and Transition Sequences," *J. Am. Ceram. Soc.*, **81** [8] 1995–2012 (1998).

[70] M. Kumagai and G.L. Messing, "Controlled Transformation and Sintering of a Boehmite Sol-Gel by α-Alumina Seeding," *J. Amer. Ceram. Soc.*, **68** [9] 500–505 (1985).

[71] T.C. Chou and T.G. Nieh, "Nucleation and Concurrent Anomalous Grain Growth of α-Al2O3 During γ - α Phase Transformation," *J. Amer. Ceram. Soc.*, **74** [9] 2270–2279 (1991).

[72] P.A. Badkar and J.E. Bailey, "The mechanism of simultaneous sintering and phase transformation in alumina," *J. Mater. Sci.*, **11** [10] 1794–1806 (1976).

<div align="center">

Chapter 2

Experimental

</div>

2.1   Introduction

This chapter highlights the experimental techniques and characterization methods used in the course of this dissertation. More specific experimental techniques are provided in each chapter.

2.2   Liquid-feed flame spray pyrolysis

Nanopowder production by liquid feed-flame spray pyrolysis (LF-FSP) typically consists of metalloorganic precursors, metal alkoxides or metal carboxylates, dissolved in an anhydrous ethanol at 2-5 wt% ceramic loading. The precursor solutions are fed at 50-100 mL/min into an atomizing nozzle and atomized by dry oxygen at 80 psi with a flow rate of 3.5 mol/min. The atomized droplets are ignited by ceramic methane oxygen torches 40 mm from the nozzle face. Four separate nozzles feed shield gas which envelops the flame, providing mixing to the turbulent flame and ensuring complete combustion. The shield gas for all studies reported here was oxygen at 80 psi with an approximate flow rate of 11.9 mol/min. Figure **2.1** shows a schematic of the LF-FSP process.
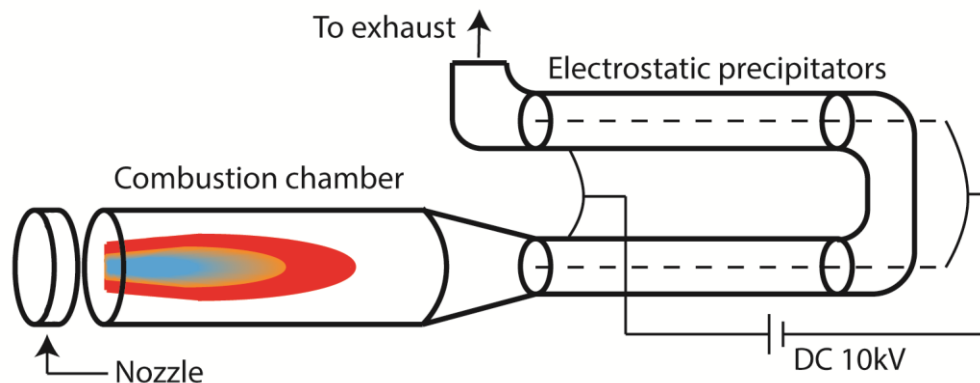
Figure 2.1. LF-FSP schematic

Nanopowders are drawn downstream of the combustion chamber by a whole laboratory exhaust system, providing 85 m^3/min of exhaust, of which approximately 5-10% is provided to the LF-FSP apparatus. Nanopowders entrained in the exhaust travel through two separate 120 cm aluminum tubes, which serve as electrostatic precipitators. Voltage is generated by a 10 kV AC oil burning furnace spark transformer. The output voltage is converted to DC with a custom bridge rectifier. The output DC potential is placed between 304 stainless steel rods placed in the center of the aluminum ESPs and the aluminum ESP tubes. The total potential is controlled by a variable transformer on the input of the AC transformer. Voltage is adjusted to provide maximum potential without arcing.

2.2.1   Precursor synthesis

Several common precursor syntheses are described here for general precursors used throughout this dissertation. More specific precursors are described in applicable chapters. Yttrium propionate, $(CH_3CH_2COO)_3Y$, was used as a precursor to all products containing Y_2O_3. Yttrium propionate was prepared by the dissolution of $Y_2(CO_3)_3$ or Y_2O_3 (PIDC,

Ann Arbor, MI) in propionic acid (Acros Organics, Geel, Belgium). Approximately 200 g (0.885 mol Y_2O_3) of starting material and 1 L (13.3 mol) of propionic acid was placed into a 3 L round bottom flask with magnetic strirring under dry N_2. The reaction was heated to 120° C for 10 h, distilling off water. Upon full dissolution of the starting material into the propionic acid to produce a yellow liquid, the reaction was heated 145° C and excess acid was distilled off. The reaction was cooled, and yttrium propionate precipitated from the supersaturated solution. Typical ceramic yields determined by TGA for yttrium propionate used in the course of these studies were 34-37%, which is consistent to the 36.6 % theoretical ceramic yield for $(CH_3CH_2COO)_3Y$.

Alumatrane was used as the precursor to all Al_2O_3 powders produced in the course of this study. Aluminum tri-*sec*-butoxide (870 g, 3.53 mol) was added to a 5 L mechanically stirred reactor under dry N_2 flow. Triethanolamine (631 g, 4.23 mol) was slowly added with an addition funnel. The reaction is exothermic, so triethanolamine was slowly added to maintain a temperature less than 80° C.

2.3   General powder processing

2.3.1   Powder treatment

Nanopowders processed for compaction into ceramic bodies typically follow the following procedure. Approximately 10 g of as-produced nanopowders are ball milled with 2 wt% bicine in 300 mL of anhydrous ethanol with 0.5 mm yttrium stabilized ZrO_2, 3 mm yttrium stabilized ZrO_2, or 3 mm 99% Al_2O_3 media for 24 hours. After 24 hours of milling, the suspension is ultrasonicated for 20 minutes at 100 W using a Vibracell VC-505 ultrasonic horn (Sonics & Materials, Newtown, CT). The suspension is then allowed to settle for 24 h and decanted to remove large settled particles. The suspension is dried, ground, and

19

sieved though 75 μm polypropylene mesh. The powder is redispersed in anhydrous ethanol with 4 wt % binder, typically polyethylene glycol (PEG) with a $M_w = 3400$. The suspension is then ultrasonicated for 20 minutes at 100 W of power. The suspension is then dried, ground, and sieved through 20 μm polypropylene mesh.

2.3.2   Pellet formation

Sieved powders are loaded into a 14.7 mm tungsten carbide die and pressed to 14 MPa to for 3 minutes to produce 700 to 1000 mg cylindrical pellets. Stearic acid is used as a die lubricant. Pellets are then vacuum sealed into latex gloves and cold isostatic pressed to in an Autoclave Engineers CIP (Avure, Lewis Center, OH) to 200 MPa for 30 minutes. A typical pressure building and release rate is 10 MPa/min.

2.3.3   Thermal processing

Pellets are typically burned out 800 °C for 4 h in dry flowing air, with a ramp rate of 3 °C/min. Burnout and sintering up to 1100 °C is conducted in a BlueM (Thermo Fisher Scintific, Waltham, MA) tube furnace with a sealed quartz tube. Sintering from 1100-1500 °C is conducted in an MTI GSL-1600X (MTI Corporation, Richmond, CA) tube furnace. For sintering from 1500-1600 °C, a BlueM muffle furnace is used.

2.3.4   Pellet densities

Pellets were first boiled for 4 h in deionized water, then were left for 24 h in room temperature water. Measurements were performed using an Archimedes density kit for an Ohaus Voyager Pro balance, with a sensitivity of 0.1 mg

2.3.5 Grain size measurements

Dense ceramic samples were polished with standard ceramographic techniques. Polished samples were thermally etched at a temperature 50° C under the sintering temperature for 30 minutes. ImageJ (NIH, Bethesda, MD) was used for grain size measurements. Two different grain size measurement techniques were used. For single phase materials or composites with relatively simple grain size distributions, the lineal intercept method was used across greater than 500 grain intercepts on at least five images. For composites with differing grain size distributions, at least 250 individual grains of each material were measured in ImageJ and adjusted by a proportionality factor of 1.56 for random slices through tetradecahedron grains.

2.4 General characterization techniques

2.4.1 X-ray diffraction (XRD)

Powder X-ray diffraction was performed on a Rigaku rotating anode diffractometer (Rigaku USA, The Woodlands, TX) at 40 kV and 100 mA. Typical continuous scan ranges were from 10-70 ° 2θ at 2°/min with a 0.02° interval. XRD patterns were analyzed using JADE 2010. Rietveld refinements were conducted within JADE using XX peak fitting model.

2.4.2 Scanning electron microscopy (SEM)

SEM was performed using a FEI Nova Nanolab dualbeam SEM/FIB or FEI Quanta 200 SEM/FIB (FEI Corporation, Hillsboro, OR). Typical accelerating voltages were 5-20 kV, depending on sample conditions. Powder samples (50 mg) were ultrasonicated in 20 mL of ethanol and dropped onto SEM sample stubs. Pellets were mounted on sample stubs with copper tape.

2.4.3 Transmission electron microscopy (TEM)

TEM was performed using a JEOL 3011 HREM (JEOL Ltd., Tokyo, Japan) at 300 kV. Powder (10 mg) was dispersed in 20 mL ethanol and wicked through a 400 mesh carbon coated copper grid.

2.4.4 Thermogravimetric analysis/differential thermal analysis (TGA/DTA)

TGA/DTA was performed on a TA Instruments Q600 TGA/SDT (TA Instruments, New Castle, DE). Precursor ceramic yields were determined by experimental runs at 10 °C/min to 1000 °C. Thermal behavior of ceramic particles or pellets was characterized by sample runs at 10 °C/min to 1400 °C. All experiments were performed with dry air flowing at 60 mL/min.

2.4.5 Surface area analysis

Specific surface areas were analyzed using a ASAP 2020 sorption analyzer (Micromeritics, Norcross, GA). Samples were degassed for 8 h at 400 °C under vacuum. An 11 point BET method analysis was conducted on 200 mg samples at relative pressures of 0.05-0.35. Nitrogen was used as the adsorbate gas and analysis was conducted in liquid nitrogen. Average particle sizes (APSs) were derived from BET SSAs per Equation **1**, where ρ is a the particle density.

Equation 1. Formula for particle size for spherical particles from SSA.

$$d = \frac{6}{(SSA) * \rho}$$

2.4.6 Dilatometry

Dilatometry was conducted with a Dilatronic II single pushrod dilatometer (Theta Industries, Port Washington, NY). Linear displacement was observed by a linear variable

differential transformer (LVDT) and recorded by a custom LabView program. Constant heating rate experiments were conducted from room temperature to 1500 °C with a 10°C/min ramp rate in static air.

2.4.7   Vickers microhardness

Microhardness measurements were made using a Clark CM-400AT equipped for Vickers hardness measurements. All measurements were taken at a load of 500 g. Values given are at least an average of ten separate indentation sites.

2.4.8   Diffuse reflectance infrared Fourier transform spectroscopy (DRIFTS)

DRIFTS samples were prepared by grinding 5 mg of nanopowder with 400 mg of spectroscopy grade KBr. Samples were analyzed on a ThermoScientific Nicolet 6700 FTIR spectrometer (Thermo Fisher Scientific, Waltham, MA) under dry flowing nitrogen. Recorded spectra were an average of 60 scans at 400-4000 cm^{-1} with a resolution of $\pm$ 4 cm^{-1}. A blank KBr served as the reference sample.

Chapter 3

Extrusion of YAG tubes

3.1   Introduction

There is a considerable driving force to develop highly transmissive materials for high-temperature transparent ceramics for applications ranging from armor, to lasers, to sodium vapor lamp envelopes.[1] The current material of choice for armor and lamp envelopes is α-Al_2O_3, whereas doped YAG has emerged as the material of choice for lasers.[2,3,4,5] While widely used, polycrystalline α-Al_2O_3 has significant optical losses due to the inherent birefringence of its hexagonal lattice.[5] As such, it is limited to translucent applications (as in vapor lamp envelopes, ave. grain sizes 20^+μm) or transparent applications if grain sizes are sub-500 nm, typically attained only by HIPping for long periods of time (12 h, 200 MPa, 1250°C).[2]

Polycrystalline YAG is a potential replacement material for polycrystalline α-Al_2O_3 due to its high transparency in the visible region, along with satisfactory thermal shock and chemical resistance.[1,4] In most applications, polycrystalline YAG is sintered at temperatures of 1700-1800° C in vacuum, taking advantage of excessive grain growth to limit porosity and grain boundary light scattering, but at the cost of both mechanical and optical properties.[6] YAG nanopowders are often made from solution based processes,

although reactive sintering of Y_2O_3 and Al_2O_3 powders also appears to be a viable route to high-quality YAG monoliths.[7]

Most laser-quality ceramic YAG is either cold pressed or slip cast to form the green body, which limits attainable geometries.[8,9] Thermoplastic extrusion is an attractive candidate for producing more complex shapes, with the drawback of much lower green densities than accessible via cold-pressing or slip casting.[10] The production of near-net shape ceramic monoliths is especially crucial in optical ceramics, where expensive and time consuming machining and polishing operations could be reduced. In addition, many demanding applications for transparent ceramics, such as missile radomes, have complicated geometries. Thermoplastic extrusion of nanopowders has rarely been studied, likely due to the challenges in obtaining high solids loadings due to the increased surface area interactions between particles in the melt leading to extremely high viscosities that prevent easy extrusion.[11,12]

Liquid-feed flame spray pyrolysis (LF-FSP) is a unique route to mixed-metal oxide nanopowders with elemental mixing at the atomic level.[13,14] In LF-FSP, ethanol solutions of metalloorganic precursors are combusted, producing nanopowder "soot" with average particle sizes (APSs) of 25-45 nm. The as-produced powders are unaggregated and lightly agglomerated. In principal, these powders offer the potential to sinter to high densities at low temperatures, with exceptional control of final grain sizes and according the bottom-up paradigm should permit ready optimization of final global properties including for example optical properties.

Indeed, the "bottom-up" approach to processing materials has received considerable support from numerous research groups in the past few years.[15,16,17,18,19,20,21,22] However, to

the best of our knowledge, no one has sought to test this concept. Thus, one major objective of the work reported here and in an accompanying paper is to attempt to validate this axiom.

We have previously used LF-FSP to produce $Y_3Al_5O_{12}$ composition nanopowders albeit finding a hexagonal phase that transforms to YAG with a low activation energy, referred hereafter to hex-$Y_3Al_5O_{12}$.[23, 24] In the work reported here, we explored the utility of using atomically mixed, single phase material as the basis for extruding tubes with the long term goal of making them transparent.

As part of this work, we also evaluated the maxim that optimal control of the scale of elemental mixing should provide the best control of sintering rates, final grain sizes and final densities. Thus, comparative studies using 3:5 molar mixtures of Y_2O_3:δ-Al_2O_3 were undertaken in an effort to process tubes using reactive sintering. In this case, nanopowders of both oxide nanopowders (APSs 30-40 nm) were mixed and then ball-milled, achieving what we estimate to be compositional homogeneity at the submicron scale at best.

Both sets of powders were thereafter mixed with an ethylene vinyl acetate polymer binder in a Brabender shear mixer and then thermoplastically extruded. Both approaches provided 10 mm diameter tubes with 0.7 mm wall thicknesses up to one meter in length. Ten cm sections were sintered to at least 95 % theoretical density (TD) with grain sizes of 0.5-3 μm. Surprisingly, nanosized Y_2O_3 and Al_2O_3 powders reactively sinter at lower temperatures and to finer final grain sizes than the YAG composition powders. This contrasts strongly with the commonly accepted maxim of "finer mixing is better."

3.2 Experimental

3.2.1 Powder processing

For reactive sintering, approximately 60 g of as-shot LF-FSP Y_2O_3 was added to 750 mL of ethanol, with 2 wt % bicine as a dispersant. The suspension was ultrasonicated for 20 minutes using a Vibracell VC-505 ultrasonic horn (Sonics & Materials, Newtown, CT) at 100 W of power. After a 24 hour settling period, the supernatant was decanted and dried. The same process was repeated using 60 g of NanoTek Al_2O_3. The dried powders were mixed in a 3:5 stoichiometric ratio, and added to 750 mL of ethanol. The suspension was ultrasonicated 20 minutes at 100 W, and dried. The resulting powders were then used for thermoplastic processing. The as-produced YAG composition powders were processed using the same conditions.

3.2.2 Shear mixing

Thermoplastic-ceramic powder extrusion mixtures were produced at volumes of 42 cm^3. The mixture consisted of 1 vol% polyethylene glycol with a M_n = 3400, 1 vol % stearic acid, 3 vol % heavy mineral oil, 48-50 vol % nanopowder, and the remainder was an ethylene vinyl acetate based hot-melt adhesive (3M #3792LM B).

Powders were mixed on a Brabender Plasti-Corder 2100 (C.W. Brabender, Hackensack, N.J.) twin-screw shear mixer. The mixing chamber was preheated to 120 °C. Approximately 80% of the hot-melt adhesive was added to the mixing chamber and allowed to melt. With the shear mixer running at approximately 60 rpm, the powder was slowly added. Powders were allowed to mix in fully before more powder was added. Upon saturation of the hot-melt adhesive with powder, the final amount of hot-melt adhesive was added. After approximately 90% of the powder had been added to the thermoplastic melt,

27

the minor components were added. Following the full addition of all the powder, the thermoplastic-ceramic melt was mixed for approximately 15 min at 60 rpm. The mixer was stopped, and the melt was cooled before it was removed from the chamber. The hardened melt was granulated, and slowly added back into the chamber at 120 °C to ensure complete homogeneity of the melt. The powder was mixed at 60 rpm for an additional 30 min. The cooled melt was manually granulated prior to extrusion.

3.2.3   Extrusion

Prior to extrusion, the thermoplastic-ceramic mixture was degassed in a vacuum oven at 110 °C for 2 h. The vacuum level was estimated to be around 10^{-3} torr. Extrusion was performed on a Bradford Small Scale Extrusion Unit (Bradford University Research, Ltd., West Yorkshire, U.K.) ram extrusion machine using a spider die. The 31 mm diameter extrusion die was preheated to 140 °C, and the granulated thermoplastic-ceramic mixture was added to the die. The bottom of the die was blocked, and the ram was pressed to a pressure of 2.3 MPa. The die was cooled to 50 °C, and the stop was removed from the end of the die. A smaller heating mantle was then applied to the spider region of the die. The spider was heated to 120-130 °C, and tubes were extruded at typical rates of 2 mm min^{-1}, with die pressures averaging 1 MPa. Dimensionally uniform tubes up to 0.7 m in length were extruded.

3.2.4   Burnout

Tubes were burned out at 3 °C min^{-1} to 400 °C for 4 h in dry N_2. Tubes were then burned out at 3 °C min^{-1} to 600 °C for 4 h in dry air. Tubes were then burnt out to 800 °C for 3 h under flowing O_2. Gas flow rates were kept constant at 50 ml/min.

3.2.5 Sintering

Tubes were sintered in rough vacuum in a MTI GSL-1600X tube furnace up to 1500° C or in a BlueM muffle furnace for temperatures above 1500° C. Two different sintering schedules were investigated, a two-step 1500° C 0 h peak with 20-30 h holds at 1300° C, or up to 35 h holds at 1500° C followed by 5 h at 1600° C.

3.2.6 Density measurements

Sample densities were tracked during sintering by monitoring the average tube diameter, which was converted into a linear shrinkage value that was correlated to the final density. Final densities were calculated using Archimedes density measurements. Samples were first boiled in deionized H_2O for 5 h and left to sit for 24 h in H_2O at room temperature. Measurements were performed using an Archimedes density kit for an Ohaus Voyager Pro balance, with a sensitivity of 0.1 mg. Dry masses were determined after heating the samples to 110° C for 24 h. All densities were compared to that of YAG, 4.55 g cm^{-3}.

3.3 Results and discussion

In the following sections, characterization of the powders used in tube processing are presented. We first characterize the powders used in tube processing, followed by discussion of the tube extrusion, binder burnout and final densification. Thereafter, the processes that lead to faster densification for the reactive sintered powders than the stoichiometrically correct single-phase powders are discussed. Thereafter we discuss the processes that occur leading to faster densification for the reactive sintered powders than the stoichiometrically correct single-phase powders. This latter discussion is presented in light of work described in chapter 6 where processing of an atomically mixed nickel, magnesium, and cobalt aluminate spinel also does not equate to better control of final

densities or grain sizes in a composite system vs mixtures of δ-Al_2O_3 and stoichiometrically correct $NiAl_2O_4$.[25]

3.3.1   Powder Characterization

Table **3-1** records the BET derived SSAs and the corresponding calculated APSs for the LF-FSP and commercial nanopowders used in this study. $Y_3Al_5O_{12}$ composition nanopowders produced by LF-FSP are a hexagonal phase as described previously, as confirmed by XRD.[24] Figure **3.1** provides SEM and TEM micrographs representative of hex-$Y_3Al_5O_{12}$ composition powders. Figure **3.2** provides an SEM micrograph representative of the LF-FSP Y_2O_3 powders. The SEM micrographs show uniform particles with typical APSs < 50 nm, which agrees with BET SSAs. The SEMs also do not reveal any particles > 200 nm. In Figure **3.1**, the TEM micrograph shows partially crystalline spherical particles. Some necking can be seen between the particles; however, this does not represent the majority of the powder.

Table 3-1. BET SSAs, and corresponding APSs, assuming spherical particles.

	Al_2O_3	Y_2O_3	$Y_3Al_5O_{12}$
BET SSA [m^2 g^{-1}]	30	30	36
APS [nm]	56	40	37
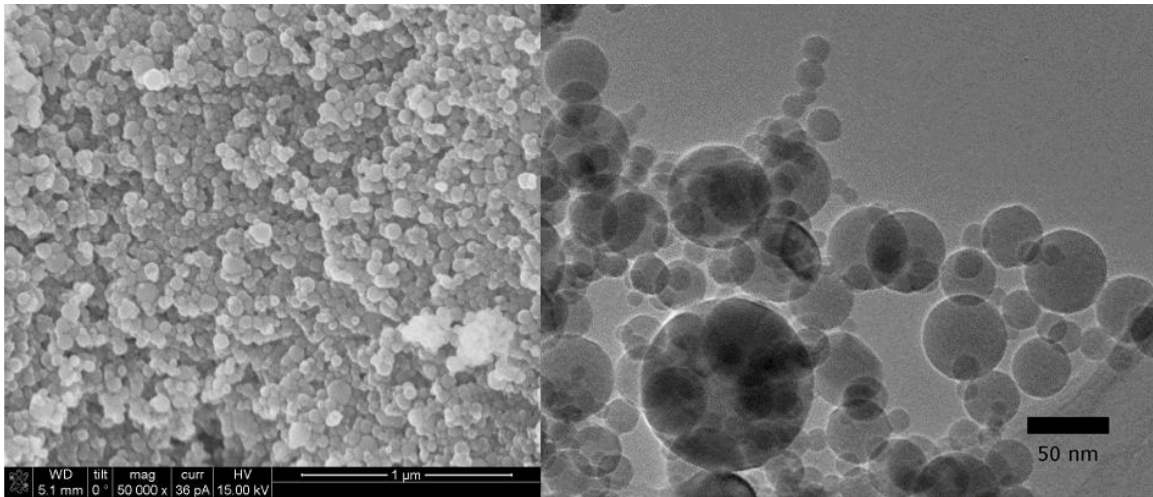
Figure 3.1a. SEM and **b**. TEM of LF-FSP produced $Y_3Al_5O_{12}$ powders.
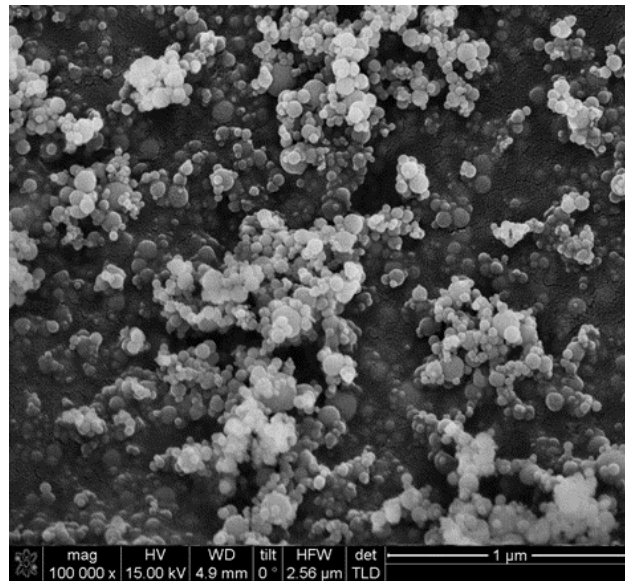
Figure 3.2. Representative SEM of as-produced LF-FSP Y_2O_3.

3.3.2 Tube Extrusion and Burnout

Through trial and error, we identified a binder, consisting primarily of a polyethylene-vinyl acetate based hot-melt adhesive that offers the viscoelastic properties needed to melt extrude powder/binder mixtures (see experimental). The adhesive materials were characterized by TGA and solvent solubility and were found not to contain any insoluble inorganic materials; therefore, no ceramic residue would be retained following binder burnout.

Tubes could be extruded up to 1 m in length with typical diameters of 10 mm with 0.7 mm thick walls. The tube lengths were limited only by the volume of melt loaded into thedie. Figure **3.3** provides a schematic of the extruder and spider extrusion die. Thermoplastic melts for extrusion were loaded at 50 vol % powder, corresponding to an approximate solids loading of 82 wt %. Powder loadings < 45 vol % were insufficient to maintain a tubular geometry through burnout. Thermoplastic melts with higher ceramic loading were difficult to extrude into defect free bodies. The high amounts of binder required a first burnout step in dry N_2, followed by dry air and then O_2. The final O_2

burnout was performed at 800 °C to impart mechanical strength to the debindered bodies.
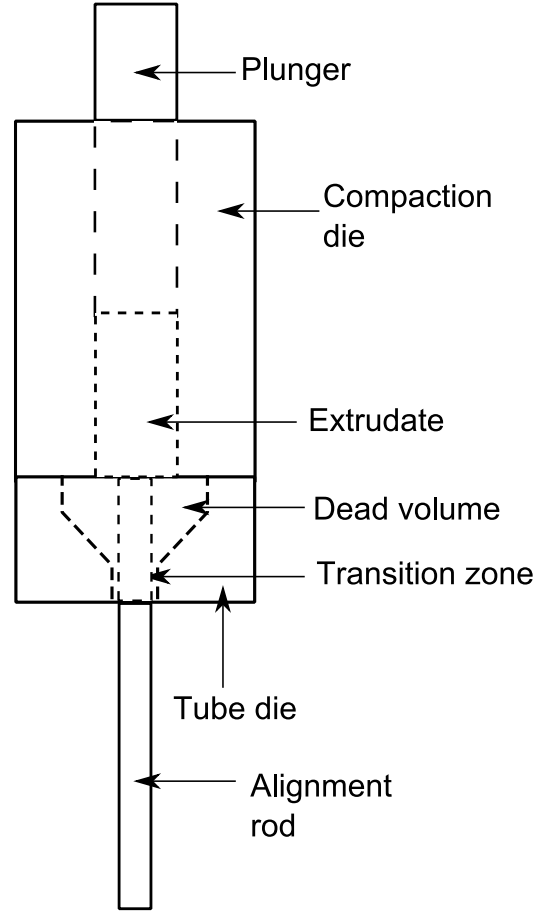
Figure 3.3. Schematic of extruder and spider extrusion die.

Figure **3.4** shows cross-sections of an as-extruded tube, a fully debindered tube, and a tube sintered to 95 % TD. Cross-sectional geometry was maintained from the as-extruded tubes through to the final sintered product. Figure **3.4b** provides a view of longer extruded sections, along with a debindered tube and a sintered tube. Some deviations from linearity along the tube axis are seen in the as-extruded tubes. However, the extrusion process did not use a guide rod, which is expected to improve overall straightness.
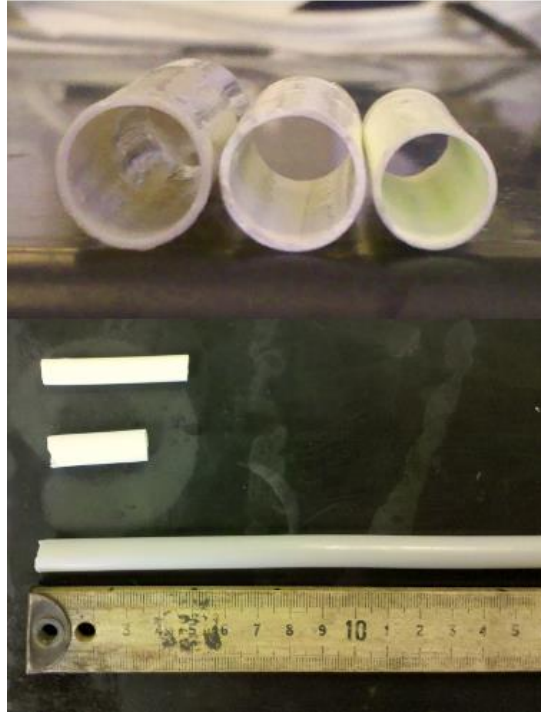
Figure 3.4a. Optical photograph of tubes, from left to right: as-extruded, burnt-out, and 95% TD. **b**. Images of tubes, from top to bottom, 95% TD sintered, burned-out, and as-extruded.

3.3.3 Tube sintering

Two different routes to 95% dense YAG tubes were examined to ensure that one processing approach did not favor one set of materials over the other. Thus, reactive sintering of Al_2O_3 and Y_2O_3 and simple sintering of hex-$Y_3Al_5O_{12}$ tubes were run under a 10^{-3}-10^{-4} torr vacuum. All samples were first heated in vacuum at 1000 °C for 2 h, which has previously been found to improve pore size distributions.[26]

One processing approach followed the two-step method of Chen and Wang, that involves ramping to a peak temperature followed by a long isothermal hold at a lower temperature.[27] Two-step sintering is an effective way to minimize grain size, and has been used successfully in processing YAG.[28][28] Reactive Y_2O_3-Al_2O_3 tubes sintered easily using two-step sintering with an initial peak temperature of 1500 °C, followed by isothermal

holds of 20-30 h at 1300 °C. Tubes sintered to a final density of at least 96 %TD after 30 h holds.

Ball milled, reactive Y_2O_3-Al_2O_3 pellets of the same composition did not sinter well below 1500 °C. This difference in sintering behavior may arise because of the intensive shear mixing of the thermoplastic mixer or simply because the binder used in forming the pellets was simply PEO rather than the vinylacetate polymer. The Figure **3.5** microstructure is typical of reactive sintered YAG and offers grain sizes of 500 ± 30 nm by lineal intercept.
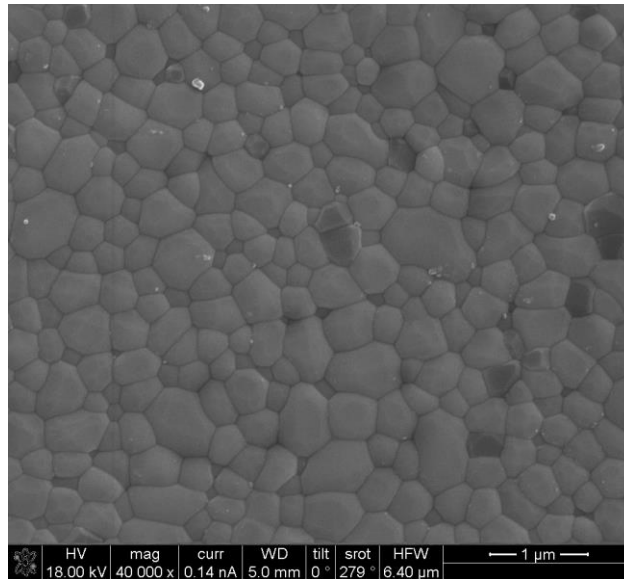
Figure 3.5. Y_2O_3-Al_2O_3 tube fracture surface SEM; two-step heated to 1500/1300°C (96 % TD).

Hex-$Y_3Al_5O_{12}$ powder tubes sinter only to ≈ 70 % TD using the same two-step scheme (Figure **3.6a**) and were only found to sinter on heating to 1500 °C for extended periods (Figure **3.6b**). After 35 h at 1500 °C in vacuum, sintering of hex-$Y_3Al_5O_{12}$ composition tubes stalled at ≈ 93 %TD. Further sintering at 1600 °C/5 h/air brought the tubes to 98 %TD with typical microstructures per Figure **3.6b**. This microstructure is characterized by

a distribution of grains much larger (3-5 µm) than seen in Figure **3.5**. For optical applications, subsequent hot isostatic pressing is mandated by the need to eliminate the remaining closed porosity.[2]
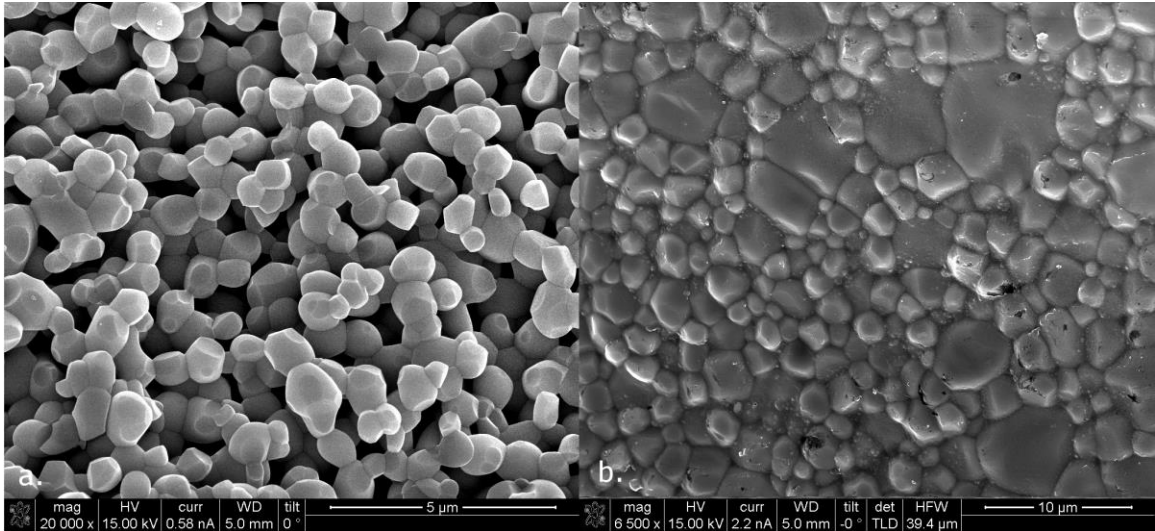
Figure 3.6. SEMs of $Y_3Al_5O_{12}$ composition **a**. tube surface two step heated to 1500/1300°C (70% TD), **b**. Fracture surface at 98 %TD after heating to 1600°C/5 h/air.

Figure **3.7** and Figure **3.8** provide time/temperature XRDs for hex-$Y_3Al_5O_{12}$ and Y_2O_3-Al_2O_3 powders mixtures, respectively. As-produced hex-$Y_3Al_5O_{12}$ powders show a diffraction pattern indicating yttrium aluminum monoclinc (YAM), $Y_4Al_2O_9$, as well as a pattern similar to hexagonal $YAlO_3$ but actually the hexagonal $Y_3Al_5O_{12}$ phase.[24] YAM, hexagonal-$Y_3Al_5O_{12}$, and $YAlO_3$ (YAP) phases are commonly present in nano-YAG synthesized by a variety of solution based processes.[29] After 3 h at 1100° C, the powders transform fully to YAG. Y_2O_3-Al_2O_3 reactive sintering consists of a mixture of Y_2O_3 and δ-Al_2O_3 at low temperatures. Heating to 1100°C causes formation of YAP and YAM. Then at 1200° C/3 h, the Y_2O_3-Al_2O_3 powders fully transform YAG.
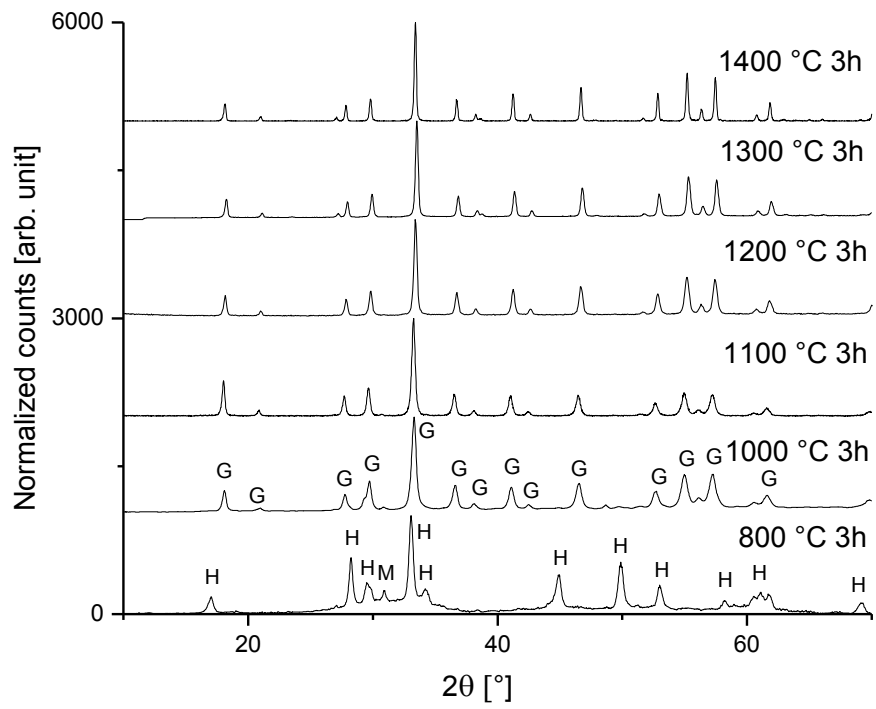
Figure 3.7. XRDs of $Y_3Al_5O_{12}$ ground tubes on sintering for 3 h at 800-1400 °C. (Hexagonal $YAlO_3$, M-$Y_4Al_2O_9$, G-$Y_3Al_5O_{12}$ garnet).
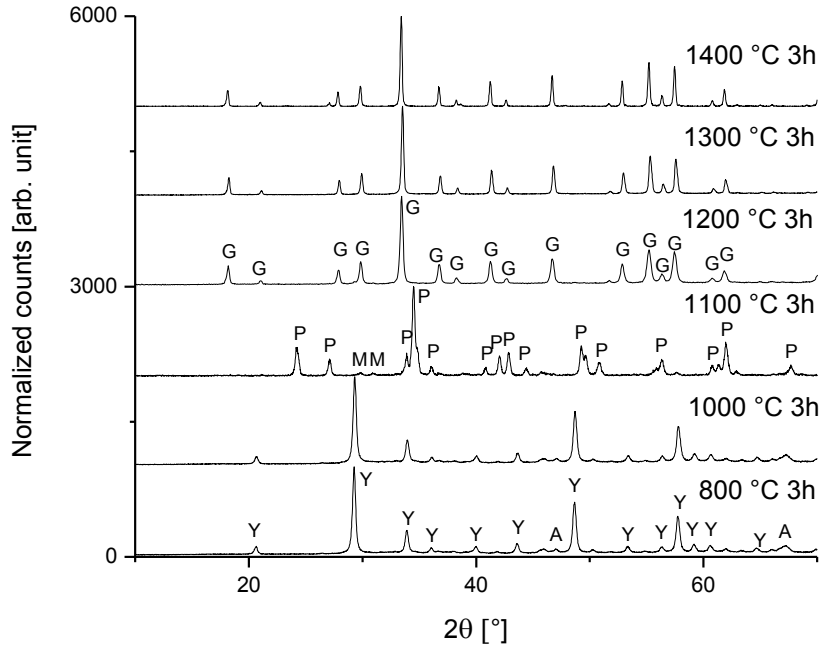
Figure 3.8. XRDs for Y_2O_3-Al_2O_3 ground tubes on sintering for 3 h at 800-1400 °C. (Y-Y_2O_3, A-transtion-Al_2O_3, P-YAP, M-YAM).

As previously shown, the activation energy for transformation of the hexagonal phase to YAG is ≈110 kJ/mol, compared to 550 kJ/mol for transformation of $YAlO_3$ to YAG. This accounts for the full transformation of the hexagonal powders at 1100° C/3 h.[24,30] DTA traces (supporting information) for both $Y_3Al_5O_{12}$ and Y_2O_3-Al_2O_3 give the Table **3-2** phase transformation temperatures.

Table 3-2. Table 2. DTA phase formation temperatures for $Y_3Al_5O_{12}$ and Y_2O_3-Al_2O_3 samples.

Material	Phase formed	
	YAP, YAM	YAG
Y_2O_3-Al_2O_3	1160° C	1307° C
$Y_3Al_5O_{12}$	915° C	1061° C

Although both samples show similar YAG nucleation temperatures, the XRD patterns suggest different rates to full transformation, likely determined by the diffusion distances. The differences in densification rates between the reactive and exact composition samples is unusual. One explanation is that densification occurs prior to full phase transformation in the Y_2O_3-Al_2O_3 system. At a low temperature, the hex-YAG powders were shown by XRD to fully transform to YAG. As such, any sintering can be explained mechanistically as that of YAG. In YAG, anion diffusion has been shown to be the rate determining species for lattice diffusion.[31] For the reactive sintering case, the mechanics are more complicated. O is the rate limiting species in Al_2O_3, and Y is the rate limiting species in Y_2O_3.[31,32][31,32]. Diffusional couples of Al_2O_3 and Y_2O_3 have shown the reaction occurs when Al diffuses into the Y_2O_3 lattice.[33][33] As such, the reaction between Al_2O_3 and Y_2O_3 should produce yttrium rich phases before YAG stoichiometry is reached. This is reflected by the XRD patterns from the reactive Y_2O_3-Al_2O_3 tubes, where yttrium rich YAP and YAM are formed prior to transformation to YAG. It should be noted that the lattice mobility of Al in Y_2O_3 is 5X that of Al in YAG[33].

Thus, there is a basis to claim low temperture densification of reative Y_2O_3-Al_2O_3 powders represents densification seen prior to full transformation to the garnet phase.

However, diffusion in some yttrium aluminate phases (YAP,YAM) has not been well characterized. As such, a number of phases with different diffusion mechanisms may exist at any one time in the sintering process.

An alternate explanation may exist for the sintering behavior seen in the Y_2O_3-Al_2O_3 system. Indeed, the micrographs shown in Figure 5 reveal small numbers of darker grains that result from less electron dense materials. Element mapping studies (**Fig. S3**) suggest that these darker grains are primarily aluminum with little or no yttrium; although we see no evidence of α-Al_2O_3 in any XRD studies. This suggests that the presence of a small amount of a secondary phase; however, it is not clear if this is responsible for the difference in sintering behavior. For 50 vol% Al_2O_3-YAG composites, Palmero et al. found a reduction in sintering temperature from 1600 °C to as low as 1370 °C with mechanical activation of powders through ball milling and an optimized pre-calcination step.[34][34] In another study, Palmero et al. found a 100 °C lower onset of sintering in 5 vol% YAG in Al_2O_3.[35][35] These studies provide a possible explanation for the low-temperature sintering behavior seen here, but the high Al_2O_3 contents studied preclude direct correlation to our work. However, if it is the basis for rapid sintering, then this represents an alternative to the use of SiO_2 as a sintering aid in the generation of transparent YAG materials. Clearly future studies should focus on exploring the effects of different excesses of Al_2O_3.

Dilatometry studies were conducted to follow densification for both systems.

3.3.4 Dilatometry studies.

Powder compacts (pellets) were pressed, CIPped and debindered to provide samples for the Figure **3.9** dilatometry studies (see experimental). There is considerable contrast between the two systems.
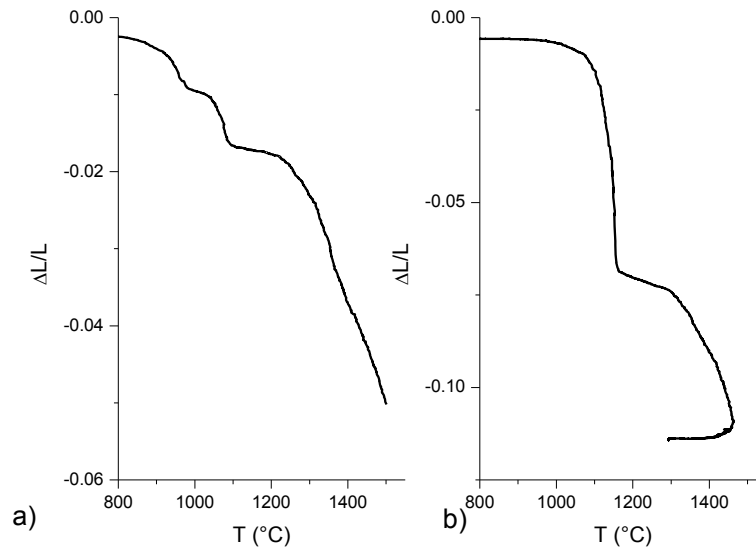
Figure 3.9. Dilatometry traces of pellets (after debindering at 800 °C) of **a**. $Y_3Al_5O_{12}$ at 5 ° and 10°C/min/air, **b**. $3Y_2O_3$:5δ-Al_2O_3, heated at 10°C/min/air to 1500° C, 1300° C for 3 h in vacuum.

The Figure **3.9a** early densification changes in the hex-$Y_3Al_5O_{12}$ powders (900-1100 °C) likely result from both reorientation of powder particles combined with crystallization of the YAG phase, based on Figure **6a** SEM and XRD studies. Thereafter, densification is slow because of the diffusion rates in YAG, as previously discussed. Indeed, as we have reported elsewhere, the only way to get high density, relatively fine grained YAG is to sinter at very high heating rates (up to 30 °C/min).[36][36]

In contrast, $3Y_2O_3$:5δ-Al_2O_3 densifies rapidly beginning at 1100-1150°C then densifying more slowly per Figure **3.9b**. The likeliest explanation is that the YAG phase forms with sintering but it is not complete even on heating to 1500°C briefly. This permits relatively rapid densification in time frames and at temperatures well below those needed to fully densify the atomically mixed $Y_3Al_5O_{12}$ materials. This is again quite contrary to the maxim that atomic mixing should provide optimal processing of ceramic materials.

41

3.3.5 Tube processing.

Figure **3.10a** is an optical micrograph of a 98% TD sintered tube (1600° C/5 h/air) that is straight and has a nearly circular cross-section, Figure **3.10b**. Samples were cut from 1 m long extruded tubes to simplify processing. Figure **3.11** shows that the tube is translucent, retaining a bluish-tint, assumed to originate from contaminants in the original powder or from shear mixing and extrusion.
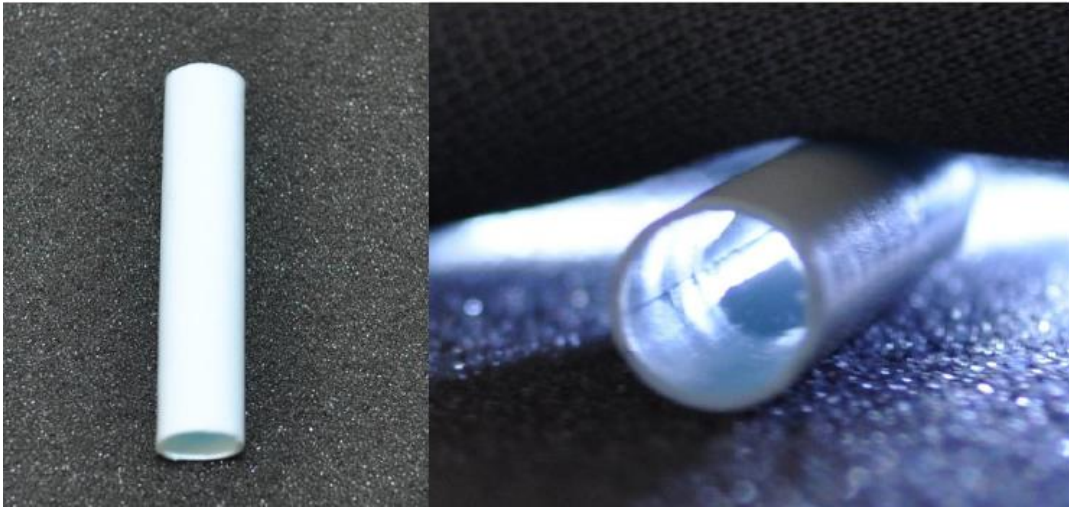
Figure 3.10. Optical micrograph of sintered 98% TD $Y_3Al_5O_{12}$ composition tube with excellent dimensional uniformity.
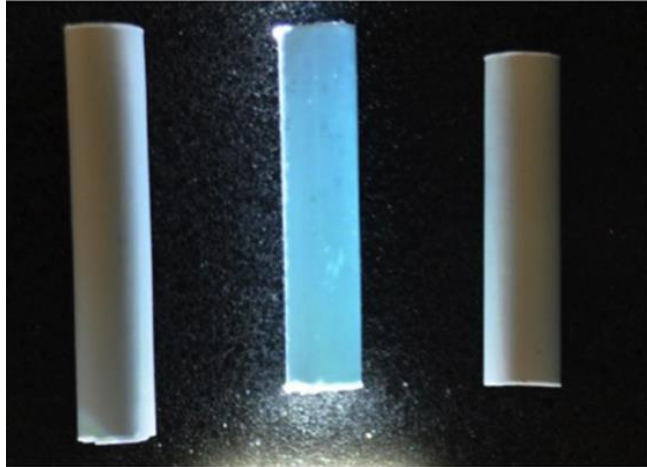
Figure 3.11. Optical micrograph of sintered, 98% TD $Y_3Al_5O_{12}$ composition tube. The light shining through the sample gives an idea of the translucency.

3.4 Conclusions

The work described above provides a rare example of thermoplastic extrusion and processing of nanooxide powders to high density ceramic tubes. More importantly it provides an example that contrasts greatly with the general maxim that atomic mixing (bottom-up approach) offers superior opportunities to control time, temperature and rates of densification in processing ceramic materials. In this paper, a single phase, atomically mixed hex-$Y_3Al_5O_{12}$ nanopowder crystallizes rapidly to YAG faster than it densifies. In contrast a shear mixed $3Y_2O_3:5\delta-Al_2O_3$ set of nanopowders, where the compositional homogeneity is closer to submicron volumes, sinters much faster because densification occurs much faster than diffusion leading to the formation of the final stoichiometric YAG phase. This work contrasts with work discussed in chapter 6, where phase segregation occurs much faster than densification leading to equivalent submicron compositional uniformity prior to processes that result in full densification.

It should be noted that our goal was to achieve densities > 95 % of theory as this represents a practical objective of researchers exploring densification mechanisms and routes to optimizing such processes.

References:

[1] G.C. Wei, "Transparent ceramic lamp envelope materials," *J. Phys. D: Appl. Phys.*, **38** [17] 3057-3065 (2005).

[2] A. Krell, P. Blank, H. Ma, T. Hutzler, and M.P. B. van Bruggen, R. Apetz, "Transparent sintered corundum with high hardness and strength," *J. Am. Ceram. Soc.*, **86** [1] 12-18 (2003).

[3] H. Yagi, T. Yanagitani, T. Numazawa, and K. Ueda, "The physical properties of transparent $Y_3Al_5O_{12}$ elastic modulus at high temperature and thermal conductivity at low temperature," *Ceram. Intl.*, **33** [5] 711-714 (2007).

[4] T.-I. Mah, T.A. Parthasarathy, and H.D. Lee, "Polycrystalline YAG; structural or functional?," *J. Ceram. Proc. Res.*, **5** [4] 369-379 (2004).

[5] R. Apetz and M.P. B. van Bruggen, "Transparent alumina: A light scattering model," *J. Am. Ceram. Soc.*, **86** [3] 480-486 (2003).

[6] A.K. Pradhan, K. Zhang, and G.B. Loutts, "Synthesis of neodymium-doped yttrium aluminum garnet (YAG) nanocrystalline powders leading to transparent ceramics," *Mater. Res. Bull.*, **39** [9] 1291-1298 (2004).

[7] A. Ikesue, I. Furusato, and K. Kamata, "Fabrication of polycrystalline, transparent YAG ceramics by a solid-state reaction method," *J. Am. Ceram. Soc.*, **78** [1] 225-228 (1995).

[8] S. Kochawattana, A. Stevenson, S.-H. Lee, M. Ramirez, V. Gopalan, J. Dumm, V.K. Castillo, G.J. Quarles, and G.L. Messing, "Sintering and grain growth in SiO_2 doped Nd:YAG," *J. Eur. Ceram. Soc.*, **28** [7] 1527-1534 (2008).

[9] K.A. Appiagyei, G.L. Messing, and J.Q. Dumm, "Aqueous slip casting of transparent yttrium aluminum garnet (YAG) ceramics," *Ceram. Intl.*, **34** [5] 1309-1313 (2008).

[10] M. Trunec, J. Cihlar, S. Diethelm, and J. Van herle, "Tubular $La_{0.7}Ca_{0.3}Fe_{0.85}Co_{0.15}O_3$-δ perovskite membranes, part I: Preparation and properties," *J. Am. Ceram. Soc.*, **89** [3] 949-954 (2006).

[11] R. C. Svedberg, R. K. Sievers, J. F. Ivanenok, T. K. Hunt, D. A. Butkiewicz, J. E. Pantolin, K. D. Swift, M. Schuller, and M. A. Ryan, "Design and Testing of AMTEC Mini-Cells," *AIP Conf. Proc.*, **301** 379-382 (1994).

[12] C. Kaya and S. Blackburn, "Extrusion of ceramic tubes with complex structures of non-uniform curvatures made from nano-powders," *J. Eur. Ceram. Soc.*, **24** [14] 3663-3670 (2004).

[13] R.M. Laine, R. Baranwal, T. Hinklin, D. Treadwell, A. Sutorik, C. Bickmore, K. Waldner, and S.S. Neo, "Making nanosized oxide powders from precursors by flame spray pyrolysis," *Key Engin. Mater.*, **17** 159-160 (1999).

[14] T. Hinklin, B. Toury, C. Gervais, F. Babonneau, J.J. Gislason, R.W. Morton, and R.M. Laine, "Liquid-feed flame spray pyrolysis of metalloorganic and inorganic alumina sources in the production of nanoalumina powders," *Chem. Mater.*, **16** [1] 21-30 (2004).

[15] C.M. Lieber, "Nanoscale science and technology: Building a big future from small things," *MRS Bull.*, **28** [7] (2003).

[16] L. Zhi and K. Mullen, "A bottom-up approach from molecular nanographenes to unconventional carbon materials," *J. Mater. Chem.*, **18** [13] 1472-1484 (2008).

[17] R. Murugavel, H.G. Walawalkar, M. Dan, H.W. Roesky, and C.N.R. Rao, "Transformations of molecules and secondary building units to materials: A bottom-up approach," *Acc. Chem. Res.*, **37** [10] 763-744 (2004).

[18] L.G. Hubert-Pfalzgraf, "To what extent can design of molecular precursors control the preparation of high tech oxides?," *J. Mater. Chem.*, **14** [21] 3113-3124 (2004).

[19] W. Lu and C.M. Lieber, "Nanoelectronics from the bottom up," *Nature Mater.*, **6** [11] (2007).

[20] J. Binner and B. Vaidhyanathan, "Processing of bulk nanostructured ceramics," *J. Eur. Ceram. Soc.*, **28** [7] (2008).

[21] R. Ramaseshan, S. Sundarrajan, R. Jose, and S. Ramakrishna, "Nanostructured ceramics by electrospinning," *J. App. Phys.*, **102** [11] (2007).

[22] S. Komarneni, "Nanocomposites," *J. Mater. Chem.*, **2** [12] 1219-1230 (1992).

[23] J. Marchal, T. John, R. Baranwal, T. Hinklin, and R.M. Laine, "Yttrium aluminum garnet nanopowders produced by liquid-feed flame spray pyrolysis (LF-FSP) of metalloorganic precursors'" *Chem. Mater.*, **16** [5] 822-831 (**2004**).

[24] R.M. Laine, J. Marchal, H. Sun, X.Q. Pan, "A new $Y_3Al_5O_{12}$ phase produced by liquid-feed flame spray pyrolysis (LF-FSP)," *Adv. Mater*., **17** [7] 830-833 (2005).

[25] N.J. Taylor, A.J. Pottebaum, V. Uz, and R.M. Laine, "The Bottom Up Approach is Not Always the Best Processing Method: Dense α-Al_2O_3/$NiAl_2O_4$ Composites," *Adv. Func. Mater.*, **24** [22] 3392-3398 (2014).

[26] J.C. Marchal, *Ph.D Thesis*, University of Michigan, USA (2008).

[27] I.-W. Chen and X.-H. Wang, "Sintering dense nanocrystalline ceramics without final-stage grain growth," *Nature*, **404** [6774] 168-171 (2000).

[28] Z.-H. Chen, J.-T. Li, J.-J. Xu, and Z-G. Hu, "Fabrication of YAG transparent ceramics by two-step sintering," *Ceram. Intl.*, **34** [7] 1709-1712 (2008).

[29] S. M. Sim, K. A. Keller, and T. I. Mah, "Phase formation in yttrium aluminum garnet powders synthesized by chemical methods," *J. Mater. Sci.*, **35** [3] 713-717 (2000).

[30] R. Chaim, "Superfast densification of nanocrystalline oxide powders by spark plasma sintering," *J. Mater. Sci*., **41** [23] 7862-7871 (2006).

[31] T. A. Parthasarathy, T.-I. Mah, and K. Keller, "Creep Mechanism of Polycyrstalline Yttrium-Aluminum Garnet," *J. Amer. Ceram. Soc.*, **75** [7] 1756-1759 (1992).

[32] M. F. Berard and D. R. Wilder, "Self-Diffusion in Polycrystalline Yttrium Oxide," *J. App. Phys.*, **34** [8] 2318-2321 (1963).

[33] V.B. Glushkova, V.A. Krzhizhanovskaya, O.N. Egorova, Yu. P. Udalov, and L.P. Kachalova,, "Interaction of Yttrium and Aluminum-Oxides," *Inorg. Mater.*, **19** [1] 80-84 (1983).

[34] P. Palmero, A. Simone, C. Esnouf, G. Fantozzi, and L. Montanaro, "Comparison among different sintering routes for preparing alumina-YAG nanocomposites," *J. Eur. Ceram. Soc.*, **26** [6] (2006).

[35] P. Palmero, V. Naglieri, J. Chevalier, G. Fantozzi, and L. Montanaro, "Alumina-based nanocomposites obtained by doping with inorganic salt solutions: Application to immiscible and reactive systems," *J. Eur. Ceram. Soc.*, **29** [1] 59-66 (2009).

[36] Y. Liu, Z.-F. Zhang, J. Halloran, and R.M. Laine, "Yttrium aluminum garnet fibers from metalloorganic precursors," *J. Am. Ceram. Soc*., **81** [3] 629-645 (1998).

Chapter 4

Processing routes to YAG/α-Al$_2$O$_3$ composites

4.1 Introduction

Liquid feed-flame spray pyrolysis (LF-FSP) is a combustion synthesis technique for the production of single metal and mixed-metal oxide nanopowders. In LF-FSP, metalloorganic precursors are dissolved in alcohols at the desired composition, and aerosolized with O$_2$. Typical oxide precursors are metal alkoxides, carboxylates, or β-diketonates. The aerosol is ignited using pilot torches and combusted. The resultant oxide nanopowders are rapidly (< 100 ms) quenched and collected downstream in electrostatic precipitators. The LF-FSP powders are typically agglomerated but unaggregated with specific surface areas (SSAs) from 30-120 m^2/g. As a gas-phase process, LF-FSP makes atomically mixed nanopowders. We term the distance separating atoms which must react in the course of synthesis to be the degree of mixing. In contrast to LF-FSP, other oxide nanopowder synthesis methods such as coprecipitation and sol-gel synthesis may have lower degrees of mixing due to inhomogeneous rates of precipitation or hydrolysis, respectively.[1] LF-FSP is scalable and has been well-studied.[2]

In the previous chapter, ball milled reactive sintering of Y$_2$O$_3$-Al$_2$O$_3$ extruded tubes densified prior to fully transforming to YAG leading to finer grain sizes than tubes synthesized from single phase Y$_3$Al$_5$O$_{12}$ composition powders. The continued densification of reactive sintered tubes at temperatures below that of typical YAG sintering led us to

more closely examine our results. Although XRD showed no secondary phases, SEM indicated inclusions that were determined to be α-Al_2O_3. This astoichiometry, along with the reactive sintering results at temperatures below that of typical YAG sintering temperatures, provided motivation for the work reported in this chapter where describe the production of YAG/α-Al_2O_3 composites, where fine grain sizes may lead to enhanced mechanical properties. In keeping with the results of Chapter 3, we again approached the same compositions from mixed Y_2O_3 and Al_2O_3 nanopowders as well as powders having the exact composition of the final composite. We will refer to the samples by their composition in vol % and mol % Al_2O_3 of the final composition.

As described in Chapter 1, multi-phase ceramic composites are a technically important class of ceramic materials. The YAG/α-Al_2O_3 composite system has seen considerable attention, especially the eutectic which showed promise as a high-temperature structural material in oxidizing environments.[3,4,5,6]

A number of methods have been used to process Al_2O_3-YAG (AY) composites via powder processing. Schehl et al. found yttrium alkoxide doping to be effective in pinning exaggerated grain growth in α-Al_2O_3 through YAG phase formation along grain boundaries.[7] The resultant micro/nano composites had well dispersed 200 nm YAG particles at α-Al_2O_3 grain boundaries. Sommer et al. produced 5, 10, and 15 vol% YAG-Al_2O_3 composites from both alkoxide coated Al_2O_3 powders and mixtures of YAG and Al_2O_3 nanopowders.[8] Sommer et al. found composites sintered at 1500° C for 3 h had theoretical densities that dropped from 98 % to 94 %TD as YAG was increased from 5 to 20 vol %. Sommer et al. reported alkoxide coated Al_2O_3 and mixed YAG and Al_2O_3 nanopowders produced composite with grains in the 3-5 μm size range.

Waku et al. synthesized eutectic composition, 45 vol% (80 mol%) Al_2O_3 YAG/α-Al_2O_3 composites from submicron Y_2O_3 and α-Al_2O_3 powders.[9] These composites exhibited a sharp reduction in flexural strength above 1000°C, likely due to amorphous material at grain boundaries. Palmero et al. produced 50 vol% YAG/α-Al_2O_3 composites from nanopowders produced by the reverse-strike-precipitation method.[10] Mechanical activation of the reverse-strike powders by planetary milling gave powders that sintered to 98% theoretical density (TD) after 2 h at 1420° C with grain sizes < 200 nm. No mechanical properties were reported. For nanopowders, the energy required to create new surfaces is beyond the energy input of ball milling, so the primary particles sizes are not reduced. Ball milling does break up agglomerates, and in this case, only mixes the powders. If perfectly mixed, the length scale of mixing would be the distance between two adjacent nanoparticles of Y_2O_3 and Al_2O_3. In practice, the length scale of mixing provided by ball milling is at least the size of agglomerates, which could be 100-800 nm in size. In LF-FSP powders that are synthesized from solutions that contain Y_2O_3 and Al_2O_3 precursors with the exact final desired composition, the length scale of mixing is assumed to be within a single particle. More credibility is given to this assumption by TEM studies of single multi-phase particles described in Chapter 5.

4.2 Experimental

Precursors were dissolved in ethanol solutions at less than 5 wt% ceramic loading. Yttrium propionate, $(CH_3CH_2CO_2)_3Y$, was used as a precursor to Y_2O_3. Alumatrane, $[N(CH_2CH_2O)_3Al]$, was used a precursor to Al_2O_3. Yttrium propionate was produced from the reaction of propionic acid with yttrium carbonate (PIDC, Ann Arbor, MI). Alumatrane was produced from the reaction of aluminum tri-sec-butoxide (Chattem Chemicals,

Chattanooga, TN) with triethanolamine. The syntheses of these precursor compounds are described in depth in Chapter 2.

Approximately 20 g of powder was ball milled with 99.5% Al_2O_3 media in ethanol for 24 h with 2 wt% bicine, $(HOCH_2CH_2)N(CH_2COOH)$, in a 500 mL Nalgene polypropylene at ¼ media loading by volume. Powders were milled on a Labmill 8000 (Gardco, Pompano Beach, FL). Powders were then ultrasonicated for 20 min at 100 W of power with a Vibracell VC-505 ultrasonic horn (Sonics & Materials, Newtown, CT). The powders were settled for 24 h, after which the remaining suspended powder was decanted. Approximately 10 wt % powders settled, and were disposed after the suspended powders were decanted. The decanted powders were dried, ground in an agate mortar and pestle, and sieved through 79 μm mesh. The powders were dispersed in ethanol with 4 wt % PEG 3400 as binder and ultrasonicated for 20 min at 100 W of power. The powders were dried, ground, and sieved through 30 μm mesh. Powders were divided into approximately 700 mg portions and pressed into 14.1 mm diameter pellets at 14 MPa. Pellets were double sealed into latex gloves and cold isostatically pressed at 200 MPa.

4.3 Results and discussion

The major objective of the work reported in this chapter is to synthesize fine-grained oxide composite materials with final microstructures consisting of well dispersed YAG and α-Al_2O_3. The secondary objective is to determine the effect, the length scale of mixing in the original nanopowder compact has on the final composite microstructure and mechanical properties. Two-phase materials were produced from both LF-FSP nanopowders synthesized at the desired composition and LF-FSP nanopowders of the constituent oxides mixed by ball milling to study the effects of phase development and

sintering on the final microstructure. As noted, we find drastically different sintering behavior and final grain sizes in YAG tubes produced with these two processing techniques, which we mainly attribute to the difference in phase development due to the initial length scale of mixing.

4.3.1 Powder characterization

Three compositions were synthesized, as detailed in Table **4-1**. The phase diagram, shown in Figure **4.1**, indicates that 88.5 mol % Al_2O_3-Y_2O_3 corresponds to the YAG/α-Al_2O_3 eutectic at 45 vol% Al_2O_3, making it a popular composition in the literature for YAG/α-Al_2O_3 composites. Although we are not accessing the eutectic, several examples of powder processed composites exist at this composition. The other two compositions synthesized here are ca. ±7 mol% from this composition, and all three compositions are within the YAG/α-Al_2O_3 two phase region.

Reactive sintering of Y_2O_3 and Al_2O_3 nanopowders will be referred to as mixed nanoparticle approach. Sintering of LF-FSP nanoparticles produced at the exact composition will be referred to as the nanocomposite approach. To avoid confusion, we will refer to the samples by their composition in vol % and mol % Al_2O_3 of the final composition. Both synthesis processes start from metastable states, so the final composition is used as the sample nomenclature to avoid confusion. As in the previous chapter, we targeted densities 95 % theoretical density (TD) as a starting point for hot isostatic pressing (HIPing) for final densification with limited grain growth.

Table 4-1. Composition table for YAG-Al_2O_3 composites.

mol% Y_2O_3	mol % Al_2O_3	mol % Al_2O_3	mol% YAG	wt% Al_2O_3	wt% YAG	vol% Al_2O_3	vol% YAG
11.5	88.5	90.0	10.0	60.8	39.2	63.9	36.1
18.5	81.5	80.4	19.6	41.4	58.6	44.6	55.4
25.3	74.7	65.8	34.2	24.9	75.1	27.4	72.6

Nanopowders were synthesized under standard LF-FSP conditions. Figure **4.2** provides a SEM micrograph of 45 vol % (80 mol %) Al_2O_3 as-produced nanocomposite nanopowder, and is typical of all powders produced in this study. Particles are all generally < 100 nm, with no fraction of large particles present. Table **4-2** gives BET SSAs for powders produced in the course of this study. APSs were calculated using $\rho = 3.58$ g/cm^3, representative of a low-density Al_2O_3-Y_2O_3 amorphous material since the true density of the powder is unknown, likely giving APSs slightly larger than their true values, as a low density would reflect a higher surface area for an equivalent mass.[11] BET derived APSs are within 20-50 nm, so the differences in particle size between nanocomposite nanoparticle and mixed nanoparticles are likely negligible.
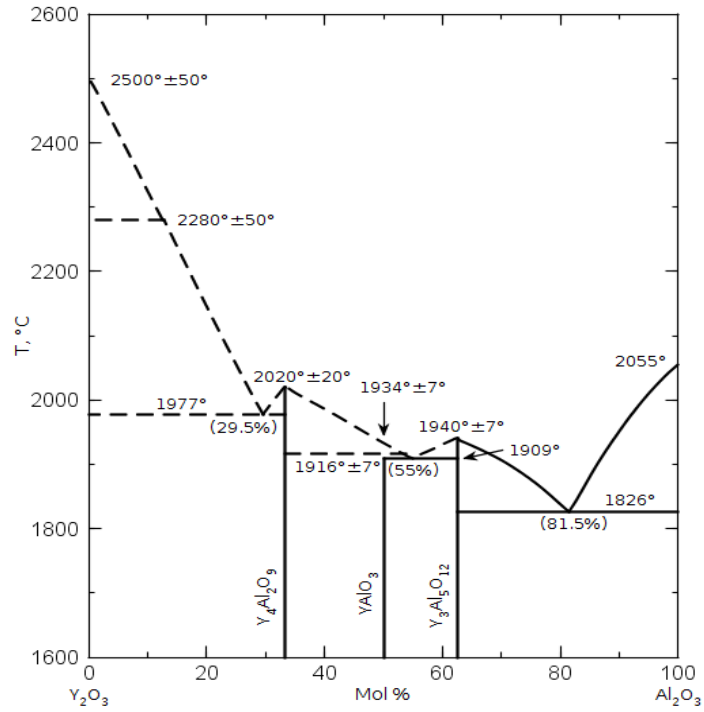
Figure 4.1. Phase diagram for Y_2O_3-Al_2O_3.[12]

Table 4-2. BET SSAs for all powders used in this study. (NN = nanocomposite nanopowders)

	BET [m^2/g]	APS [nm]
Al_2O_3	65	26
64 vol% NN	41	41
45 vol% NN	38	44
27 vol% NN	36	47
Y_2O_3	53	23
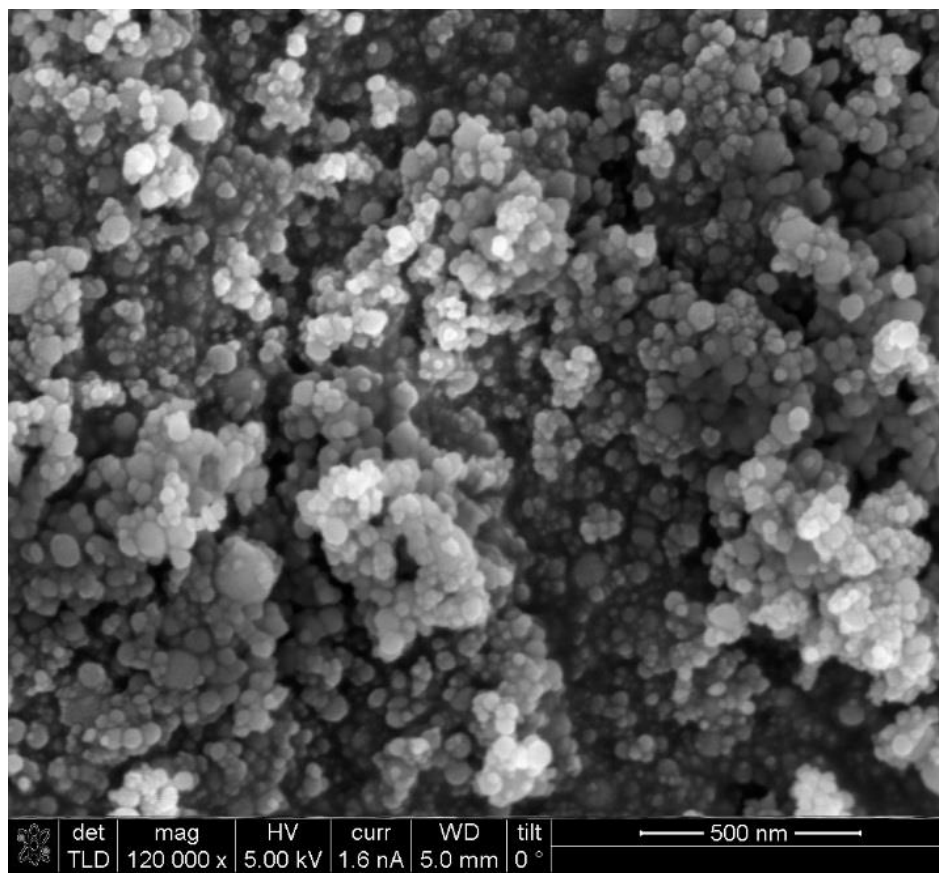
Figure 4.2. SEM micrograph of as-produced 45 vol% (80 mol%) Al_2O_3 nanocomposite nanoparticles.

Figure **4.3** provides XRDs of as-produced nanocomposite powders. At 27 vol % Al_2O_3, δ-Al_2O_3, δ^*-Al_2O_3, and hexagonal $YAlO_3$ are present, along with an amorphous hump centered at 33° 2θ. Hexagonal $YAlO_3$ is an intermediate phase, seen in almost all nano-YAG syntheses.[13] δ-Al_2O_3 and δ^*-Al_2O_3 are transition-Al_2O_3 phases, typical of nano-Al_2O_3, and the two most common phases in LF-FSP Al_2O_3.[14] At 45 and 64 vol % (80 and 90 mol %) Al_2O_3, δ-Al_2O_3 is not seen, with only δ^*-Al_2O_3 and hexagonal $YAlO_3$ observed. Both retain a significant amorphous fraction, indicated by an amorphous hump centered on 33° 2θ. Rietveld refinement of the XRD pattern for pure LF-FSP Y_2O_3 powders used in this study gives 77% cubic and 23% monoclinic. XRD shows LF-FSP Al_2O_3 to be a mixture of transition Al_2O_3 phases, mostly δ and δ^*.
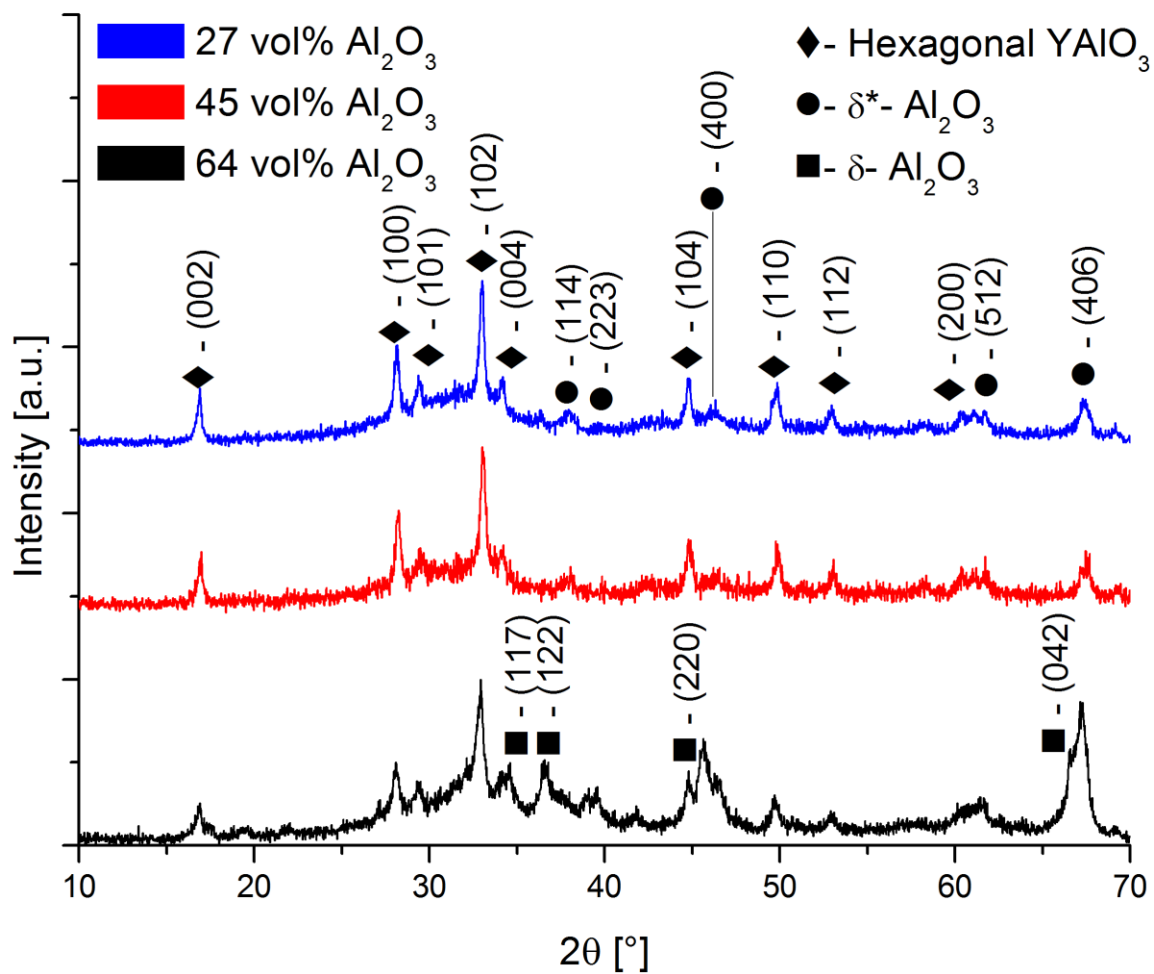
Figure 4.3. XRD patterns for 27, 45, and 64 vol % (66, 80, and 90 mol %) Al_2O_3 as-produced nanopowders.

4.3.2 Thermal analysis
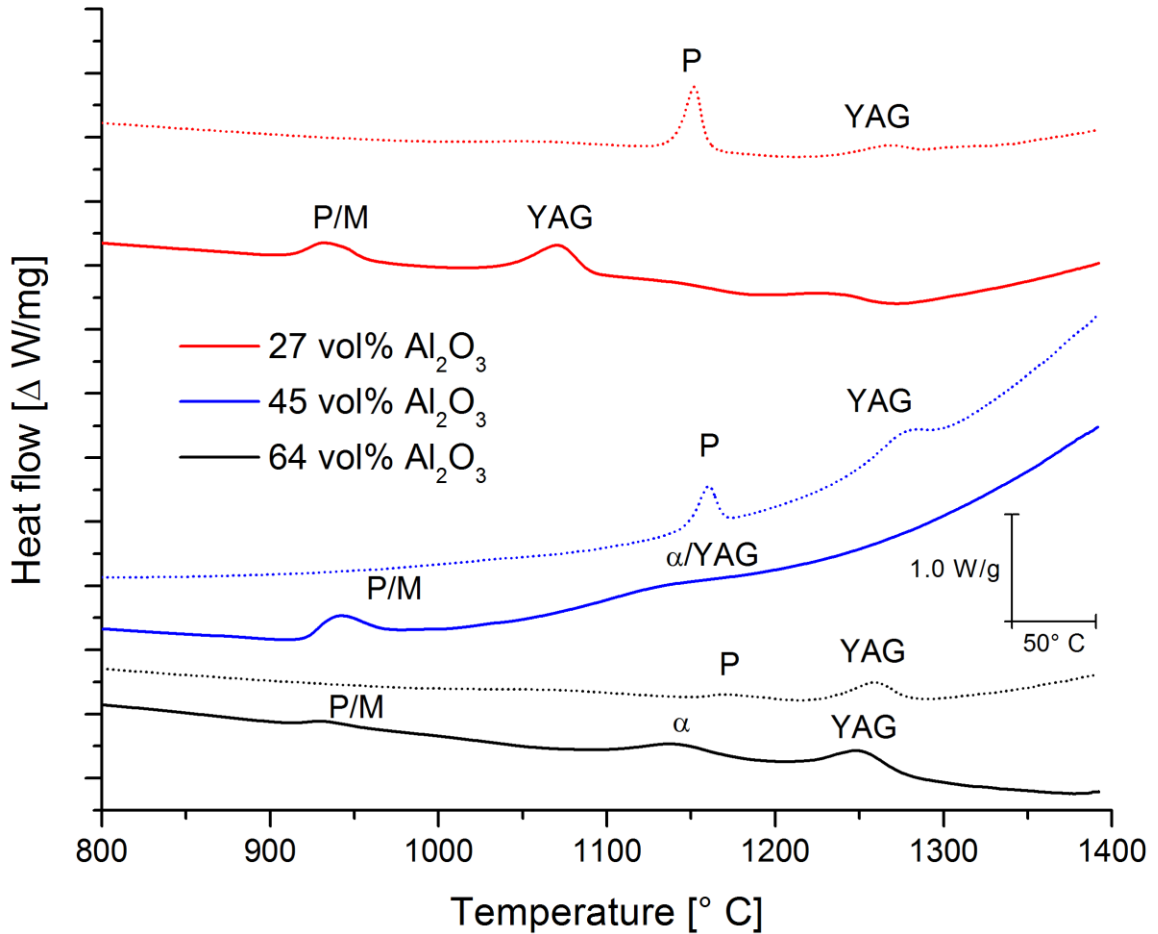
Figure 4.4. DTA traces of both mixed nanoparticle (dotted lines) and nanostructure nanoparticle pellets (solid lines). (P = $YAlO_3$ perovskite, M = $Y_2Al_4O_9$ monoclinic, YAG = $Y_3Al_5O_{12}$, α = α-Al_2O_3).

Figure **4.4** shows DTA traces from TGA/DTA analyses of pellets after binder burnout. Dotted traces correspond to the mixed nanoparticle approach, and solid lines to nanocomposite nanoparticles. It is important to note that YAP or $YAlO_3$ perovskite, and YAM, monoclinic $Y_2Al_4O_9$, are often intermediate products in YAG synthesis. Microdiffraction of TGA samples was used to identify the phase transformations associated with the exotherms. The increasing background for both 45 vol % (80 mol %) Al_2O_3 samples are a function of DTA baseline calibration and do not indicate any real thermal

affect. All three nanocomposite nanoparticle samples show an exotherm at $\approx 935°$ C, corresponding to the transformation from hexagonal $YAlO_3$, δ-Al_2O_3, δ*-Al_2O_3 to YAP and/or YAM as both are indicated by XRD. In the 27 vol % (66 mol %) Al_2O_3 nanocomposite nanoparticle sample, an exotherm centered at 1070° C corresponds to the transformation to YAG. In the 45 vol % (80 mol %) Al_2O_3 nanocomposite nanoparticle sample, an exotherm around 1130° C corresponds to either the YAG and/or α-Al_2O_3 transformation, as both phases are present by XRD after the exotherm. In the 64 vol % (90 mol %) Al_2O_3 nanocomposite nanoparticle sample, an exotherm at 1140° C is typical of the transformation to α-Al_2O_3, and the exotherm around 1250° C corresponds to the transformation to YAG from YAP/YAP and Al_2O_3.

All three compositions show similar YAP/YAM transformation temperatures, but note that the YAG transformation is suppressed as Al_2O_3 content increases. Per the phase diagram in Figure **4.1**, both YAP and YAM are Y_2O_3 rich in comparison to YAG, so the transformation is diffusional. As Al_2O_3 content increases, the local composition is more Al_2O_3 rich, and the reaction is delayed up to 180°C due the diffusion necessary for YAG transformation. Alternately, the reduction in YAG transformation temperature as Al_2O_3 increases suggests large YAP/YAM concentrations within a particle react with small amounts of Al_2O_3 more quickly than small amounts of YAP/YAM react with large amounts of Al_2O_3 to form YAG. This suggests a shift in the morphology of the particles as the composition is changed. Diffusional couples of Y_2O_3 and Al_2O_3 show the dominant mass transport is Al_2O_3 diffusion into Y_2O_3, so small islands of Al_2O_3 adjacent to YAP/YAM within a single particle may more quickly react to form YAG.[15] Hay studied YAG formation from diphasic Y_2O_3-Al_2O_3 gels and found diffusion of Al_2O_3 is rate-controlling

in YAG formation.[16] At high volumetric loading of Al_2O_3, the diffusion rate of Al_2O_3 may be less than the diffusion rate into YAP/YAM, leading to the delay in YAG transformation seen here. Hay also observed the presence of YAG at temperatures as low as 800° C, indicating our DTA transformation temperatures are typical for this system.

In the mixed nanoparticle materials, an exotherm around 1160° C corresponds to the transformation to YAP, and the 1250-1270° C exotherm corresponds to the transformation to YAG, as seen by XRD. No change in thermal behavior is seen with compositional changes for the mixed nanoparticle processing approach. For mixed nanoparticles, the reaction occurs as a diffusion couple between adjacent Y_2O_3 and Al_2O_3 nanoparticles. The local Y_2O_3-Al_2O_3 interface is unchanged regardless of the global composition, so little change is seen in the DTA indicated phase transformations. In contrast, the local composition of the nanocomposite nanoparticles closely matches the global composition. As a result, the DTA indicates phase transformations are dependent on the global concentrations.

4.3.3 Dilatometry

Figure **4.5** provides dilatometric traces for all three compositions from both nanocomposite nanoparticle and mixed nanoparticle samples. All samples had green densities of 53 ± 2% TD. Both the mixed nanoparticle and nanocomposite 64 vol % (90 mol %) Al_2O_3 composites show the most densification up to 1500° C at 15 and 14% linear strain, respectively. Both the 45 and 27 vol % (80 and 66 mol %) Al_2O_3 mixed nanoparticle samples show similar densification levels of 12 and 13 % linear strain. The nanocomposite 45 and 27 vol % Al_2O_3 samples showed similar densification of ≈ 8 % linear strain up to 1500° C, below that of the their respective mixed-nanoparticle counterparts. The

nanocomposite sintering curves for 45 and 27 vol % (80 and 66 mol %) Al_2O_3 are similar to those seen in Chapter 3 for pure LF-FSP YAG nanopowders. This may indicate once YAG is the volume majority phase, the sintering of the continuous 3D connected YAG grains may be rate limiting for composite densification.
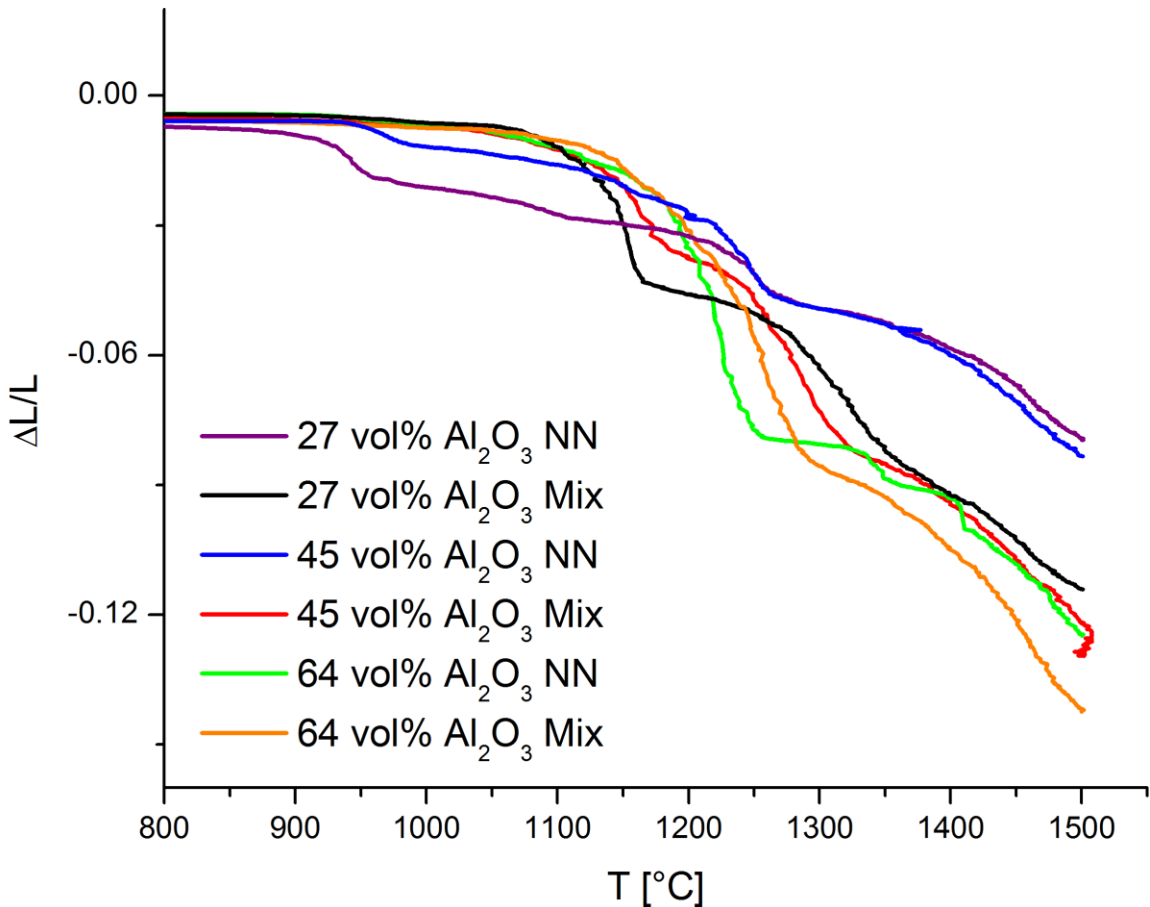
Figure 4.5. Dilatometry traces for all compositions studied.

The sintering of the Al_2O_3-YAG composites reflects the dilatometry curves. Our sintering targeted densities of 95 % TD reflecting a practical density with closed porosity for further processing by hot isostatic pressing (HIPing) to high densities with minimal grain growth. Different sintering temperatures were used, but the data here are presented

as an iso-density case. Figure **4.6** gives polished SEM micrographs for all three compositions for both processing methods.

4.3.4 Final microstructure
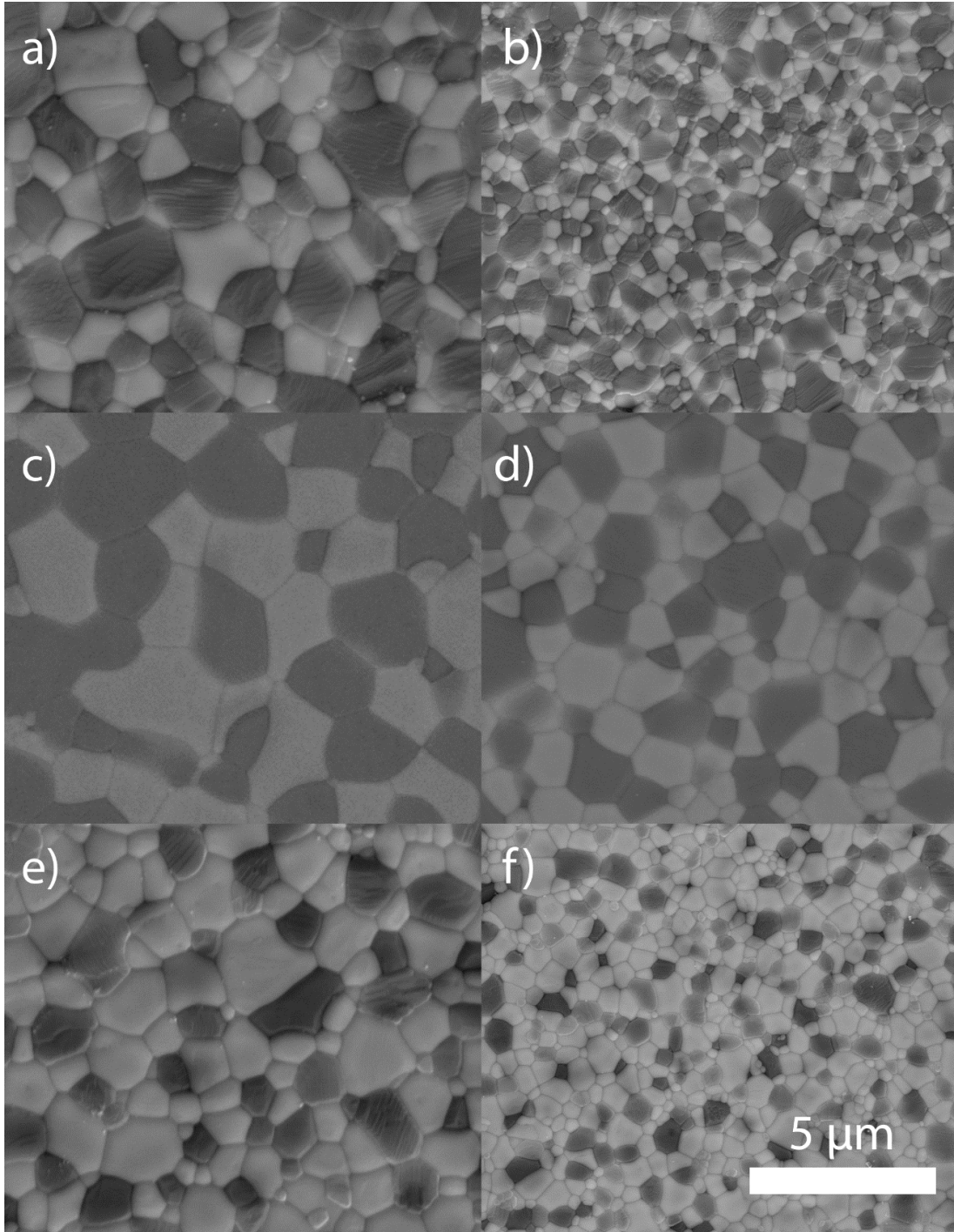
Figure 4.6. SEM micrographs at 95 %TD for a) 64 vol% Al_2O_3 nanocomposite b) 64 vol% Al_2O_3 mixed c) 45 vol% Al_2O_3 nanocomposite d) 45 vol% Al_2O_3 mixed e) 27 vol% Al_2O_3 nanocomposite f) 27 vol% Al_2O_3 mixed.

In a reflection of the higher densification at lower temperatures, the mixed nanoparticle composites sinter to much finer grain sizes than the nanocomposite nanoparticle composites at equivalent densities of 95±1 %TD. In general, the larger grain sizes observed for the nanocomposite nanoparticle case is likely a consequence of the higher sintering temperatures used. Table **4-3** gives the measured grain sizes from the polished SEM micrographs. Average grain sizes do not differ significantly with composition. All of the mixed nanoparticle composites have average grain sizes for both phases of ≈ 1000 nm. The nanocomposite nanoparticle samples have grain sizes for both phases of ≈ 1700 nm.

Table 4-3. Average grain sizes in nm for all three compositions (NN = nanocomposite nanoparticle, Mix = mixed nanoparticle).

	YAG [nm]	Al_2O_3 [nm]	%TD	Schedule
64 vol% Al_2O_3 NN	1800 ± 310	1600 ± 400	95	1500 °C 8h
64 vol% Al_2O_3 Mix	730 ± 270	1100 ± 460	95	1500 °C 8h
45 vol% Al_2O_3 NN	1800 ± 370	1700 ± 300	94	1600 °C 4h
45 vol% Al_2O_3 Mix	980 ± 250	1000 ± 280	95	1600 °C 4h
27 vol% Al_2O_3 NN	1700 ± 420	1700 ± 380	95	1600 °C 4h
27 vol% Al_2O_3 Mix	910 ± 380	1000 ± 320	95	1500 °C 8h

4.3.5   Vickers microhardness

Microhardness data for each sample are tablulated in Table **4-4**. Larrea et al. suggest that the Al_2O_3 content dominates the hardness in YAG/α-Al_2O_3 eutectic composites, and our results fit well with this observation.[17] Here we note higher indicated hardness values are observed as volume fraction of Al_2O_3 increases. No significant differences between the nanocomposite nanoparticle and mixed nanoparticle samples were observed. The hardness of bulk Al_2O_3 is commonly cited as 17.7 GPa, but values as high as 20 GPa have been

obtained from nanopowder processed Al_2O_3 with 1 μm AGS.[18] The bulk Al_2O_3 hardness is equivalent to our 64 vol % (90 mol %) Al_2O_3 mixed nanoparticle sample, and below the nanocomposite nanoparticle sample of the same composition, but both are below the 20 GPa for nanopowder derived Al_2O_3. For reference, Li and Gao obtained a hardness of 16.15 GPa for 75 vol% Al_2O_3-YAG composites.[19] Although these results suggest enhanced hardness due to a pseudo-Hall-Petch grain size effect, the high hardness values here may also be a consequence of the low loading used in microhardness testing.[20] Our microhardness testing used a load of 500 g, where Vickers hardness tests for true hardness measurements are recommended to use 5-10 kg loads. Comparative hardness studies with higher loads should be performed in the future to determine if a true grain size hardness effect is present.

Table 4-4. Vickers microhardness results (NN = nanocomposite nanoparticle, Mix = mixed nanoparticle.

Material	Hardness [GPa]
64 vol% Al_2O_3 NN	18.6 ± 1.7
64 vol% Al_2O_3 Mix	17.8 ± 1.5
45 vol% Al_2O_3 NN	16.5 ± 1.7
45 vol% Al_2O_3 Mix	16.5 ± 1.4
27 vol % Al_2O_3 NN	15.1 ± 1.3
27 vol% Al_2O_3 Mix	14.7 ± 0.8

The results shown here indicate that as in Chapter 3, the low temperature transformation to YAG in the nanocomposite nanoparticle processing scheme prevents densification, and as a result the mixed nanoparticle reactive sintering processing scheme provides finer grain sizes. In the YAG/α-Al_2O_3 system, the mixed nanoparticle case provides finer microstructures, with no indication that particle mixing affected the final phase dispersion. The AGSs are consistent with literature, except for Palmero et al. who

found < 200 nm AGSs from planetary milled powders.[7] Although not well explored here, the finer grain size of the mixed nanoparticle samples may lead to better mechanical properties.

4.4 Conclusions

YAG/α-Al$_2$O$_3$ composites were prepared by two processing schemes, the mixing of the constituent oxide nanopowders, or mixed nanopowders, and nanocomposite nanoparticles containing the overall stoichiometry of the composite. In all cases, the mixed nanoparticle case sintered to microstructures with significantly finer grain sizes than that of the nanocomposite nanoparticle processing scheme at equivalent densities. These results are similar to that of Chapter 3, in which the mixed nanoparticle case sintered to much finer grain sizes than that of Y$_3$Al$_5$O$_{12}$ composition powders. Similarly, we find here that transformation to the YAG phase prevents low temperature densification in the nanocomposite nanoparticle materials here.

In the nanocomposite nanoparticle samples, thermal analysis by DTA indicated a significant reduction in the YAG nucleation temperature from 1250° C to 1070°C as Y$_2$O$_3$ content was increased. Since YAG is formed from the Al$_2$O$_3$ reaction with YAP/YAM, this suggests the particle morphology may allow for smaller diffusion distances for rate-limiting Al$_2$O$_3$ species as Y$_2$O$_3$ is increased. In the mixed nanoparticle processing scheme, no change in the thermal behavior is seen with changing composition, which is consistent with a fixed reaction front between adjacent Al$_2$O$_3$ and Y$_2$O$_3$ nanoparticles.

Hardness testing showed no significant increase in the hardness between the nanocomposite nanoparticle and mixed nanoparticle processing schemes. Hardness did

increase as the volume fraction increased, to a peak of 18.6 ± 1.7 GPa for the 64 vol% Al_2O_3 nanocomposite nanoparticle sample. This value is above that of bulk Al_2O_3, but lower than that of some fine-grained Al_2O_3. Future testing with higher Vickers hardness loads should be performed to determine if we are seeing a true Hall-Petch type increase in hardness due to grain size.

As we test the bottom-up approach to composite synthesis, we find the mixed nanoparticle processing case to be superior to that of the nanocomposite nanoparticle processing scheme. This runs contrary to the idea that controlling the composite composition at the finest possible length scale leads to the best composites. In addition, the results described here indicate powder processing is likely much more important the powder chemical homogeneity. Despite the advantage of the mixed nanoparticle approach, the AGSs are around 1 μm. To reduce the grain size into the nanometer range, we explored the addition of a third phase to both further pin grain boundary movement and provide lower temperature sintering. These studies are described in Chapter 5, where we add a Y_2O_3 stabilized ZrO_2 phase to YAG/α-Al_2O_3 composites.

References

[1]M. Kakihana, "Invited review 'sol-gel' preparation of high temperature superconducting oxides," *Journal of Sol-Gel Science and Technology*, **6** [1] 7–55 (1996).

[2]S.E. Pratsinis, "Flame aerosol synthesis of ceramic powders," *Progress in Energy and Combustion Science*, **24** [3] 197–219 (1998).

[3] T.A. Parthasarathy, T.-II Mah, and L.E. Matson, "Processing, structure and properties of alumina-YAG eutectic composites," *J. Ceram. Proc. Res.*, **5** [4] 380-390 (2004).

[4] K. Hirano, "Application of eutectic composites to gas turbine system and fundamental fracture properties up to 1700 °C," *Journal of the European Ceramic Society*, **25** [8] 1191–1199 (2005).

[5] Y. Waku, N. Nakagawa, T. Wakamoto, H. Ohtsubo, K. Shimizu, and Y. Kohtoku, "A ductile ceramic eutectic composite with high strength at 1,873 K," *Nature*, **389** [6646] 49–52 (1997).

[6] J. LLorca and V.M. Orera, "Directionally solidified eutectic ceramic oxides," *Progress in Materials Science*, **51** [6] 711–809 (2006).

[7] M. Schehl, L.A. Díaz, and R. Torrecillas, "Alumina nanocomposites from powder–alkoxide mixtures," *Acta Materialia*, **50** [5] 1125–1139 (2002).

[8] F. Sommer, F. Kern, H.F. El-Maghraby, M.A. El-Ezz, M. Awaad, R. Gadow, and S.M. Naga, "Effect of preparation route on the properties of slip-casted Al2O3/YAG composites," *Ceramics International*, **38** [6] 4819–4826 (2012).

[9] Y. Waku, N. Nakagawa, H. Ohtsubo, A. Mitani, and K. Shimizu, "Fracture and deformation behaviour of melt growth composites at very high temperatures," *Journal of Materials Science*, **36** [7] 1585–1594 (2001).

[10] P. Palmero, A. Simone, C. Esnouf, G. Fantozzi, and L. Montanaro, "Comparison among different sintering routes for preparing alumina-YAG nanocomposites," *Journal of the European Ceramic Society*, **26** [6] 941–947 (2006).

[11] M.C. Wilding, C.J. Benmore, and P.F. McMillan, "A neutron diffraction study of yttrium- and lanthanum-aluminate glasses," *Journal of Non-Crystalline Solids*, **297** [2–3] 143–155 (2002).

[12] T.-II Mah and M.D. Petry, "Eutectic Composition in the Pseudobinary of $Y_4Al_2O_9$ and Y_2O_3," *J. Amer. Ceram. Soc.*, **75** [7] 2006-2009 (1992).

[13] S.-M. Sim, K.A. Keller, and T.-I. Mah, "Phase formation in yttrium aluminum garnet powders synthesized by chemical methods," *Journal of Materials Science*, **35** [3] 713–717 (2000).

[14] T. Hinklin, B. Toury, C. Gervais, F. Babonneau, J.J. Gislason, R.W. Morton, and R.M. Laine, "Liquid-Feed Flame Spray Pyrolysis of Metalloorganic and Inorganic Alumina Sources in the Production of Nanoalumina Powders," *Chem. Mater.*, **16** [1] 21–30 (2004).

[15] V.B. Glushkova, V.A. Krzhizhanovskaya, O.N. Egorova, Yu. P. Udalov, and L.P. Kachalova,, "Interaction of Yttrium and Aluminum-Oxides," *Inorg. Mater.*, **19** [1] 80-84 (1983).

[16] R.S. Hay, "Phase transformations and microstructure evolution in sol-gel derived yttrium-aluminum garnet films," *Journal of Materials Research*, **8** [03] 578–604 (1993).

[17] A. Larrea, V.M. Orera, R.I. Merino, and J.I. Peña, "Microstructure and mechanical properties of Al_2O_3–YSZ and Al_2O_3–YAG directionally solidified eutectic plates," *Journal of the European Ceramic Society*, **25** [8] 1419–1429 (2005).

[18] X. Teng, H. Liu, and C. Huang, "Effect of Al_2O_3 particle size on the mechanical properties of alumina-based ceramics," *Materials Science and Engineering: A*, **452–453** 545–551 (2007).

[19] W.Q. Li and L. Gao, "Processing, microstructure and mechanical properties of 25 vol% YAG-Al_2O_3 nanocomposites," *Nanostructured Materials*, **11** [8] 1073–1080 (1999).

[20] A. Krell, "Comment: The Effect of Grain Size on the Mechanical and Optical Properties of Spark Plasma Sintering-Processed Magnesium Aluminate Spinel $MgAl_2O_4$ (Rothaman et al.)," *Int. J. Appl. Ceram. Technol.*, **12** E174–E175 (2015).

Chapter 5

Al$_2$O$_3$-YAG-YSZ composites

5.1   Introduction

In Chapter 3, we showed that the reactive sintering of Al$_2$O$_3$ and Y$_2$O$_3$ nanopowders produced dense, fine-grained tubes at lower temperatures than nanopowders with the exact Y$_3$Al$_5$O$_{12}$ composition. We attributed these results to densification that occurred during the transformation to the YAG phase. A secondary factor was a small α-Al$_2$O$_3$ excess which may explain the low-temperature sintering of the reactive tubes. The densification enhancement, along with the possibility to reduce grain size by pinning grain boundary motion, led us to consider YAG/Al$_2$O$_3$ two-phase composites. In Chapter 4, we showed that mixing of constituent Al$_2$O$_3$ and Y$_2$O$_3$ nanopowders produces composites that sinter to finer grain sizes than those made from LF-FSP nanopowders produced at the desired composition of the final composite. We term these two approaches either "mixed nanoparticle or mixed nanopowder" for ball mill mixing of the constituent single metal oxides, and "nanocomposite nanoparticle or nanocomposite nanopowder" for individual particles having the composition of the final composite. As in Chapter 4, this approach tests the bottom-up approach to composite formation. The bottom-up is a paradigm of materials synthesis in which the best global properties are expected from materials that are built from the smallest possible length scale. In this study, the nanocomposite nanoparticle processing method represents bottom up processing, where the length scale of mixing is

68

within the average particle size, APS, or < 30 nm. At best, the mixed nanoparticle processing approach gives a length scale of mixing within the volume of three adjacent particles of each separate material. However, perfect mixing is unlikely, and the length scale of mixing is likely on the order of agglomerate size, which can vary from 100-800 nm.

In Chapter 4, α-Al_2O_3/YAG composite AGSs were > 1 μm in size, despite starting from < 50 nm nanopowders. In a single phase material, diffusion through the lattice or along grain boundaries can easily provide mass transport to facilitate grain boundary migration. In a multi-phase material, an adjacent grain of dissimilar phase provides a barrier to diffusion that would facilitate grain boundary migration. Equivolumetric four-phase composites would theoretically provide complete isolation in 3D space, i.e. a grain of one material should not share a grain boundary with a grain of the same phase.[1] An additional phase should decrease grain sizes, as adjacent grains of dissimilar material require longer diffusion distances for grain growth.[1] This provides the motivation for the work described in this chapter. Starting from the YAG/α-Al_2O_3 composites synthesized in Chapter 4, we produced composites with a third phase, Y_2O_3 stabilized c-ZrO_2. Previously, LF-FSP core-shell ZrO_2-Al_2O_3 powders were shown to sinter to fully dense composites at 1120° C with AGSs < 200 nm.[2] The studies described here sought to test: the pinning effect of a third phase on grain size, the effect of a phase with a lower sintering temperature, and the effect of the so called "bottom-up" approach to composite processing. As in Chapter 4, we will refer to the composites in terms of their vol% (and mol%) YSZ fraction.

Several groups have produced eutectic composites in the Al_2O_3-YAG-YSZ system.[3,4,5,6] As with the YAG/Al_2O_3 composites discussed in Chapter 4, eutectic

composites are typically produced as prospective high-temperature structural materials.[3,4,6] A few examples of powder processed Al_2O_3-YAG-YSZ or AYZ composites have been reported. Palmero et al. synthesized AYZ composites from $Y(Cl)_3$ and $Zr(Cl)_4$ decomposition on nanosized transition Al_2O_3 nanopowders.[7] Palmero et al. produced composites of 90 Al_2O_3- 5 YAG-5 vol% YSZ, 60 Al_2O_3- 20 YAG-20 vol % YSZ, and 34 Al_2O_3-33 YAG-33 vol % YSZ. In sintering 34:33:33 vol % slip cast composites, they demonstrated grain sizes < 500 nm after 3 h at 1500° C at 98 % TD.

Oelgardt et al. synthesized AYZ composites at the same composition as reported here by milling < 300 nm commercially available powders of Al_2O_3-Y_2O_3-Al_2O_3 (AYZ) and Al_2O_3-YAG-YSZ (YAG-AZ).[8] Oelgardt et al. reported 95 % TD after sintering 1 h at 1500° C with average grain sizes (AGSs) of 0.55 μm for Al_2O_3, 0.56 μm for YAG, and 0.46 μm for YSZ. The YAG-AZ of Oelgardt et al sintered to 98 % TD after 1 h at 1500° C with AGSs of 0.64 μm for Al_2O_3, 0.78 μm for YAG, and 0.50 μm for YSZ. Kim and Kriven synthesized 34:33:33 vol % AYZ composites from nanopowders produced by the steric entrapment method.[9] Samples sintered to full density after 3 h at 1550 ° C with AGSs > 1 μm.

5.2 Experimental

Precursors were dissolved in ethanol solutions at less than 5 wt% ceramic loading. Yttrium propionate, $(CH_3CH_2CO_2)_3Y$, was used as a precursor to Y_2O_3. Alumatrane, $[N(CH_2CH_2O)_3Al]$, was used a precursor to Al_2O_3. Syntheses for yttrium propionate and alumatrane are described in Chapter 2. Zirconium isobutyrate was used as a precursor to ZrO_2. Zirconium isobutyrate was produced from the reaction of isobutyric acid with

zirconium basic carbonate at 130° C. Dried zirconium basic carbonate, $Zr(OH)_2CO_3 \cdot ZrO_2$, (200 g, 0.49 mol) was added to a 1 L round bottom flask with 600 mL (6.6 mol) and the reaction was heated to 140° C for 5 h until all of the zirconium basic carbonate was dissolved. Isobutyric anhydride was added and the reaction was continued for 8 h at 155° C until a dark brown solution was obtained. The obtained zirconium isobutyrate had a TGA ceramic yield of 42.0%, which means the precursor likely had a formula of $[((CH_3)_2CHCO_2)_2(OH)Zr]O[Zr(OH)(O_2CCH(CH_3)_2)]$, with a theoretical ceramic yield of 42.4%.

Approximately 20 g of powder was ball milled with 99.5% Al_2O_3 media in ethanol for 24 h with 2 wt% bicine. Powders were then ultrasonicated for 20 minutes at 100W of power with a Vibracell VC-505 ultrasonic horn (Sonics & Materials, Newtown, CT). The powders were settled for 24 h, after which the remaining suspended powder was decanted. For mixtures of single metal oxides, powders were first dispersed in ethanol and settled for 24 h prior to milling to account for any differences in settling rate. The powders were dried, ground, and sieved through 79 μm mesh. The powders were dispersed in ethanol with 4 wt% PEG 3400 as binder and ultrasonicated for 20 minutes at 100W of power. The powders were dried, ground, and sieved through 30 μm mesh. The powders were pressed at 14 MPa and cold isostatically pressed at 200 MPa.

5.3   Results and Discussion

The major objective of work in this chapter is to test the effect of length scale of mixing on the production of fine-grained composites from the mixed nanoparticle and nanocomposite nanoparticle route. Within this objective, we are specifically interested in how the length scale of mixing in the initial mixture affects the sintering behavior and the

final microstructure of the composite. A secondary objective is to determine if a third phase leads to a reduction in grain size due to the aforementioned pinning effect. In this chapter, we will begin with characterization of the as-produced nanopowders, then discuss the sintering behavior and final microstructures along with hardness measurements. Sintering studies in this chapter targeted densities of 95 %TD, which represents a starting point for HIPing studies.

5.3.1 Powder characterization

All nanopowders were produced under standard LF-FSP conditions. Table **5-1** contains the compositional data for the three compositions studied in both vol% and mol% of the final composite phases. Within this chapter, the nomenclature will be vol% YSZ, along with the mol% YSZ. Full compositions can be referred back to Table **5-1**.

Table 5-1. Phase compositions for the three composites synthesized.

YSZ vol% (mol%)	YAG vol% (mol%)	Al_2O_3 vol% (mol%)
15 (10)	29 (70)	56 (20)
23 (16)	26 (65)	51 (19)
32 (23)	24 (60)	44 (17)
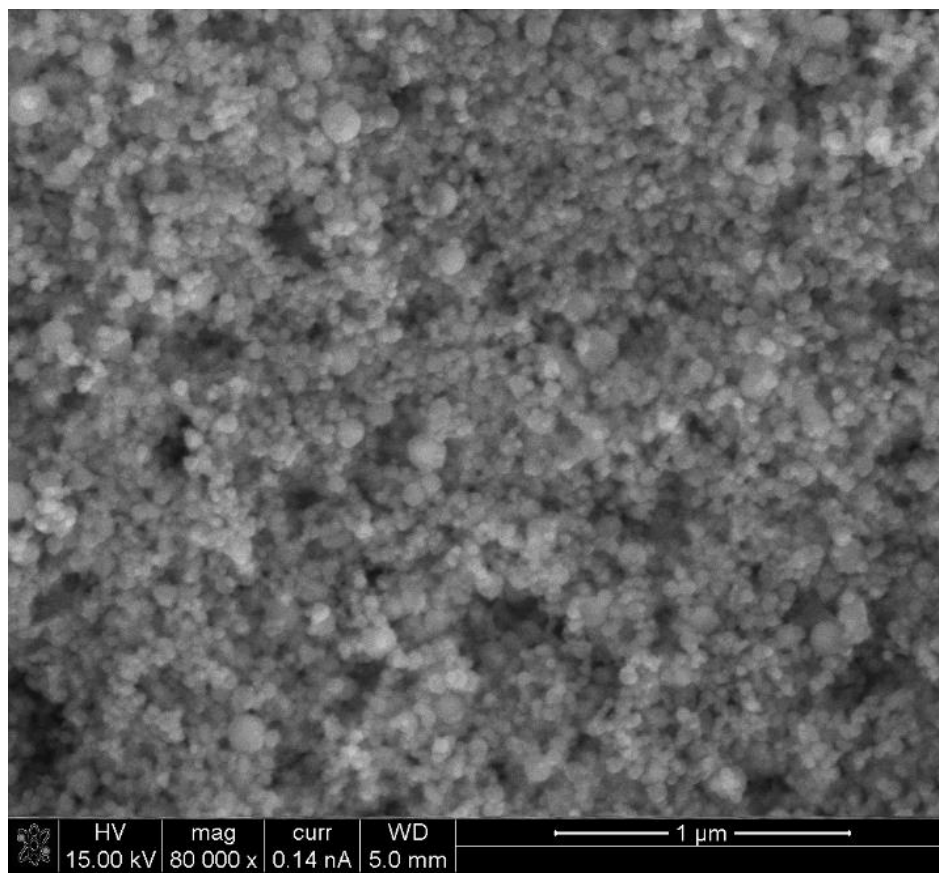
Figure 5.1. SEM image 15 vol% (10 mol%) YSZ nanocomposite nanopowder.

Figure **5.1** shows an SEM micrograph of 15 vol% (10 mol%) YSZ as-produced nanocomposite nanopowder. The powders are typical of LF-FSP synthesis with no fraction of larger particles. Table **3-1** shows the BET SSAs for each powder and a corresponding APS. BET SSAs are typical for LF-FSP nanopowders, and the single metal oxide particles have similar APSs (20-30 nm) as the nanocomposite nanopowders.

Table 5-2. BET SSA and APS for all powders used in this study. (NN = nanocomposite nanopowder)

	SSA [m²/g]	APS [nm]
15 vol% YSZ NN	33	30
23 vol% YSZ NN	39	26
32 vol% YSZ NN	46	22
Al_2O_3	65	26
Y_2O_3	53	23
ZrO_2	32	31
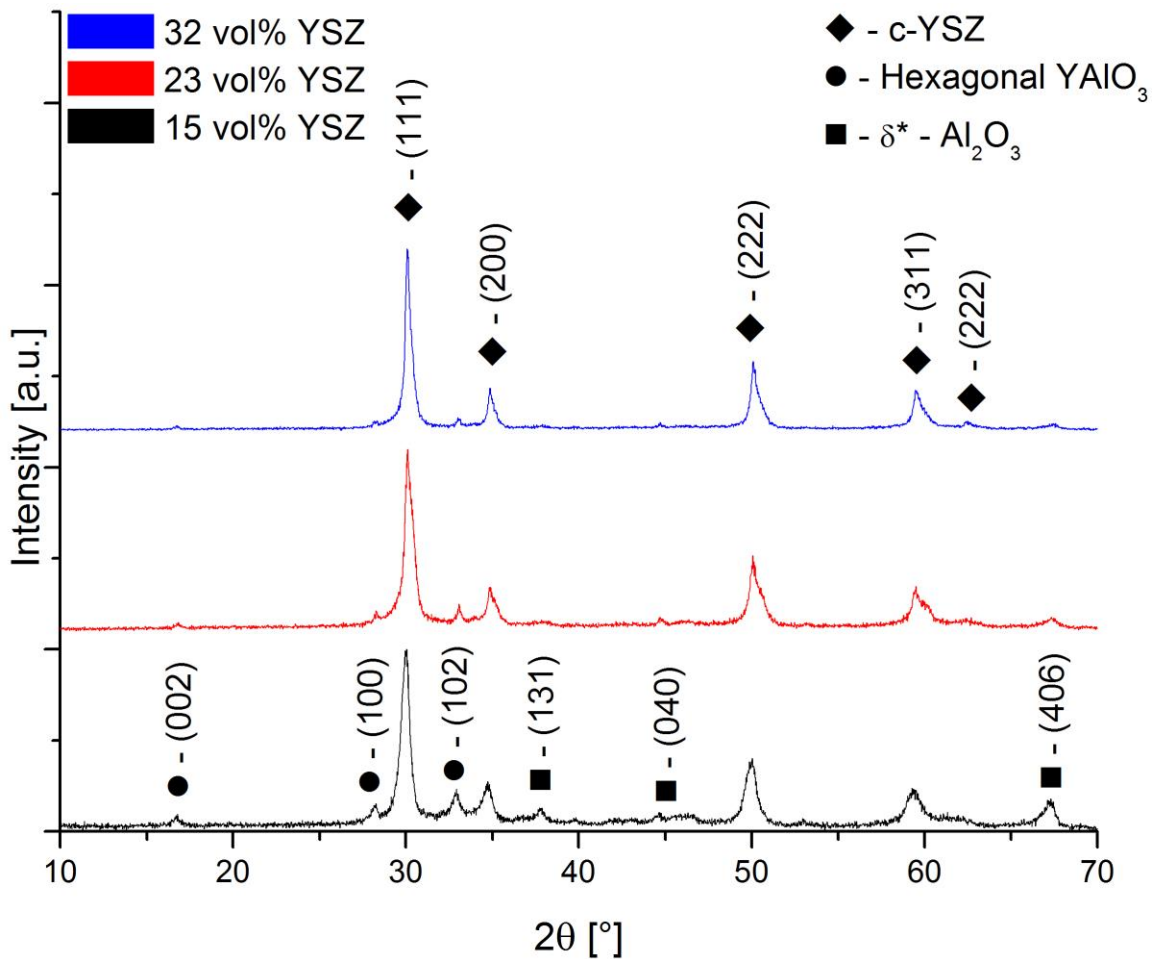
Figure 5.2. XRD patterns for as-produced 15 (10), 23 (16), and 32 vol% (23 mol%) YSZ nanocomposite nanopowders.

Figure **5.2** shows the XRD patterns for the as-produced nanocomposite nanopowders.

Cubic yttria stabilized ZrO_2 is the primary phase visible by XRD, along with hexagonal

YAlO$_3$ and δ*-Al$_2$O$_3$. As discussed in Chapters 3 and 4, hexagonal YAlO$_3$ is a common intermediate phase in the synthesis of YAG, and δ*-Al$_2$O$_3$ is the most common phase in LF-FSP produced Al$_2$O$_3$ nanopowders.[10,11] For the mixed nanoparticle case, ZrO$_2$ is a mixture of 48 wt % monoclinic ZrO$_2$ and 52 wt % tetragonal ZrO$_2$. Y$_2$O$_3$ is a mixture of 10 wt% monoclinic and 90 wt% cubic phases. Al$_2$O$_3$ is a mixture of transition Al$_2$O$_3$ phases, at 57 wt % δ*-Al$_2$O$_3$, 30 wt % δ-Al$_2$O$_3$, and 15 wt % γ-Al$_2$O$_3$.
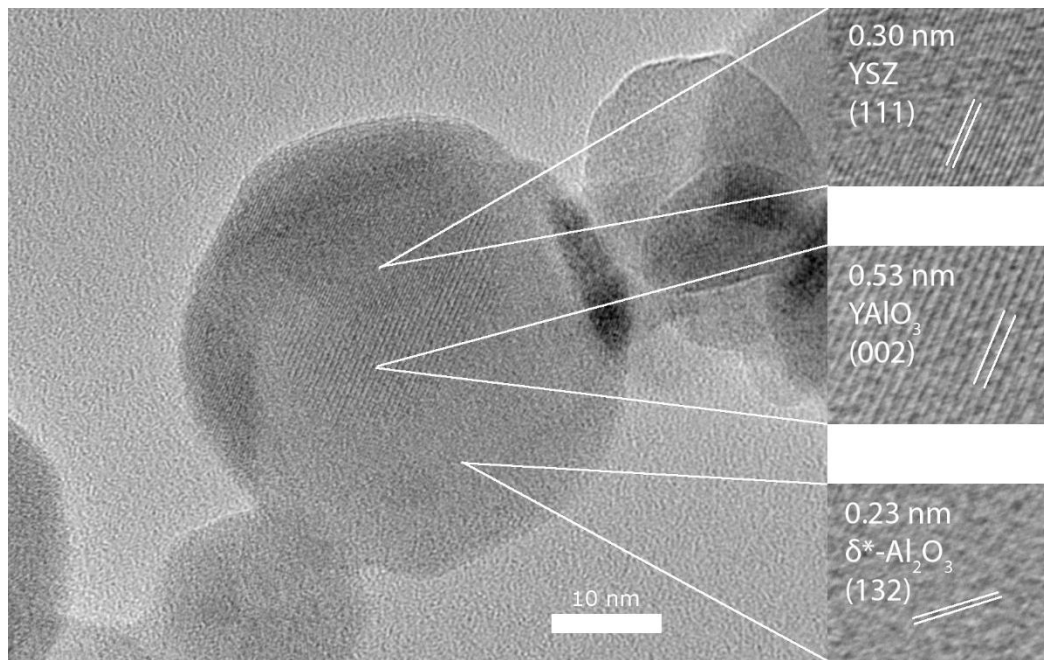
Figure 5.3. HRTEM of 15 vol % (10 mol %) YSZ nanocomposite nanoparticle, with inset high magnification TEM micrographs. A spacing of 0.30 nm corresponds to the YSZ (111), a spacing of 0.53 nm corresponds to YAlO$_3$ (002), and a spacing of 0.23 nm corresponds to δ*-Al$_2$O$_3$ (132). Inset not shown to scale.

Figure **5.3** shows a TEM micrograph of a nanocomposite nanoparticle with inset close-up micrographs of the three major crystalline regions within the particle. Fast Fourier transforms (FFTs) of each crystalline region provide the lattice spacings given on the inset micrographs. The crystalline region with a spacing of 0.30 nm corresponds to the (111) c-YSZ planar spacing, the region with a spacing of 0.53 nm corresponds to the (002)

75

hexagonal $YAlO_3$ spacing, and the region with a spacing of 0.23 nm corresponds to the

(132) δ^*-Al_2O_3. The lattice spacings in this figure match with the phases observed by XRD.

FFTs were used in lieu of selected area electron diffraction (SAED) due to the difficulty in

producing usable SAED patterns from such small regions.
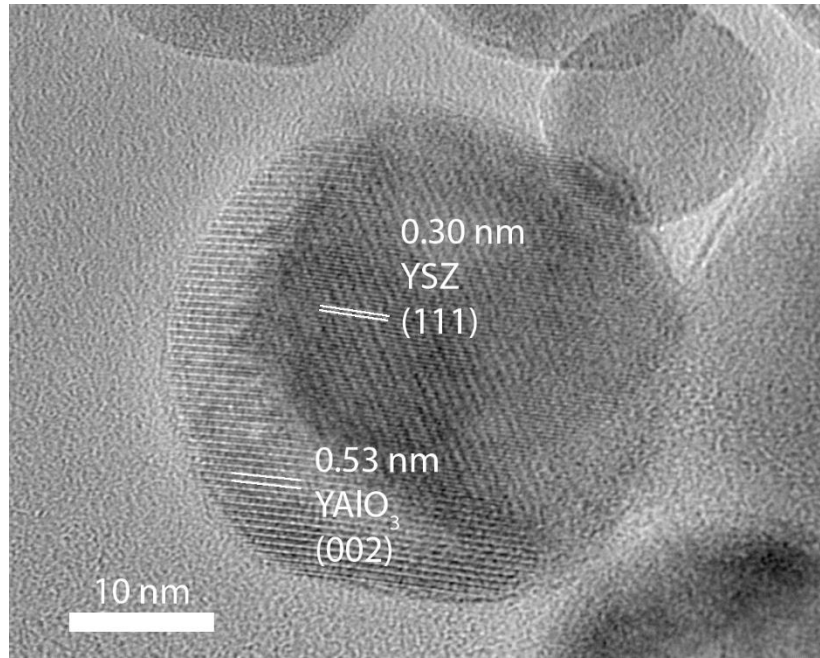
Figure 5.4. HRTEM micrograph showing 15 vol% (10 mol%) YSZ nanocomposite nanoparticle showing crystallite with 0.30 nm spacing, corresponding to the YSZ (111), and a region showing a lattice spacing of 0.53 nm, corresponding to $YAlO_3$ (002).

Other particles show the same three phase particle morphology, although it is difficult

to resolve the δ^*-Al_2O_3 phase. Figure **5.4** shows another particle with two clear crystalline

regions. FFTs give a lattice spacing for the left region of 0.53 nm, consistent with the

hexagonal $YAlO_3$ (002) spacing, and secondary FFT points in the same orientation at 0.26

nm correspond to the (004) spacing. In the other crystalline region, FFTs give a lattice

spacing of 0.30 nm, consistent with the c-YSZ (111) plane. Figure **5.5** provides four more

particles with similar morphology. Together, these micrographs provide a strong example

of nanocomposite nanoparticles. This novel result has implications beyond the composite

processing presented here. With multiple phases in contact in each particle, the interface between the phases becomes a large volume fraction of each particle, which may lead to novel properties. In Chapter 7, we investigate the LF-FSP formation of other nanocomposite nanoparticles.
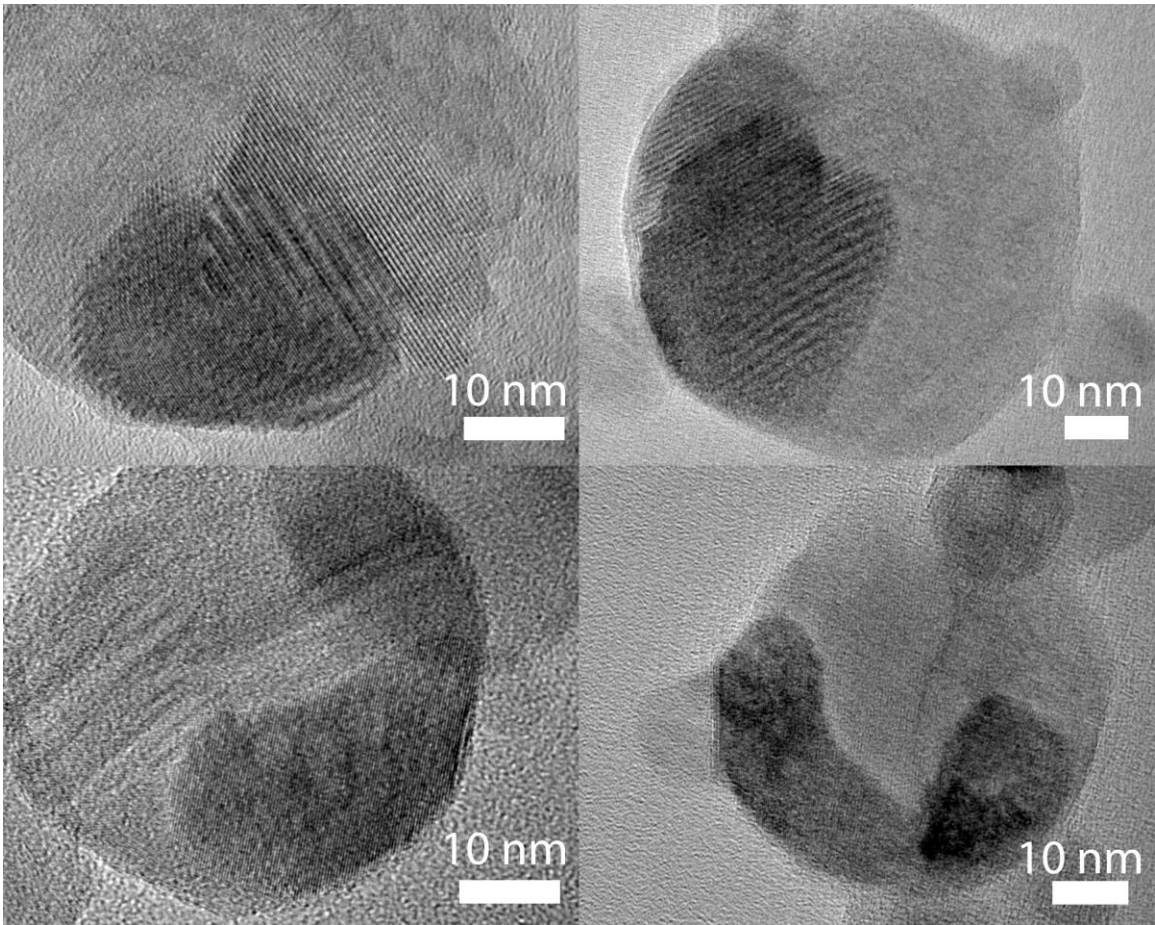
Figure 5.5. TEM micrographs of 15 vol% (10 mol%) showing nanocomposite nanoparticle morphology.

5.3.2 Dilatometry
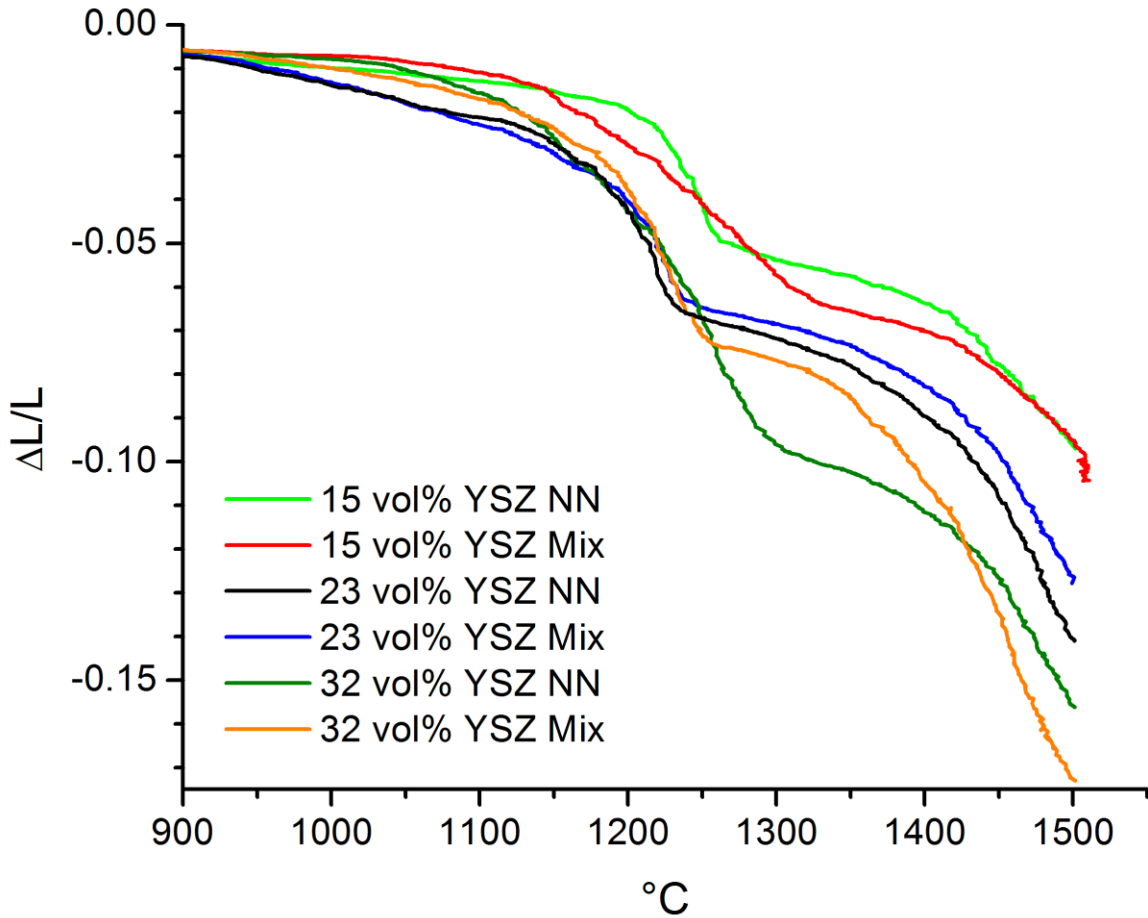
Figure 5.6. Dilatometry for all mixed nanoparticle and nanocomposite nanoparticle (NN) samples.

Figure **5.6** shows the dilatometry traces for both nanocomposite nanoparticle and mixed nanoparticle processing approaches. The first trend seen is increasing YSZ content is associated with higher densification up to 1500° C. For the nanocomposite nanoparticle samples, linear densification goes from 9 to 17% on increasing the YSZ volume fraction from 15 to 32 %. In the mixed nanoparticle samples, linear densification goes from 9 to 15% as YSZ volume fraction is increased from 15 to 32%. The second trend is that, nanocomposite nanoparticle processing provides higher densification up to 1500° C than the mixed nanoparticle approach for a given composition. This is in contrast to Chapters 3

and 4, where the reactive sintering or mixed nanoparticle approach led to higher densification than the nanocomposite nanoparticle case.

5.3.3   Final microstructure
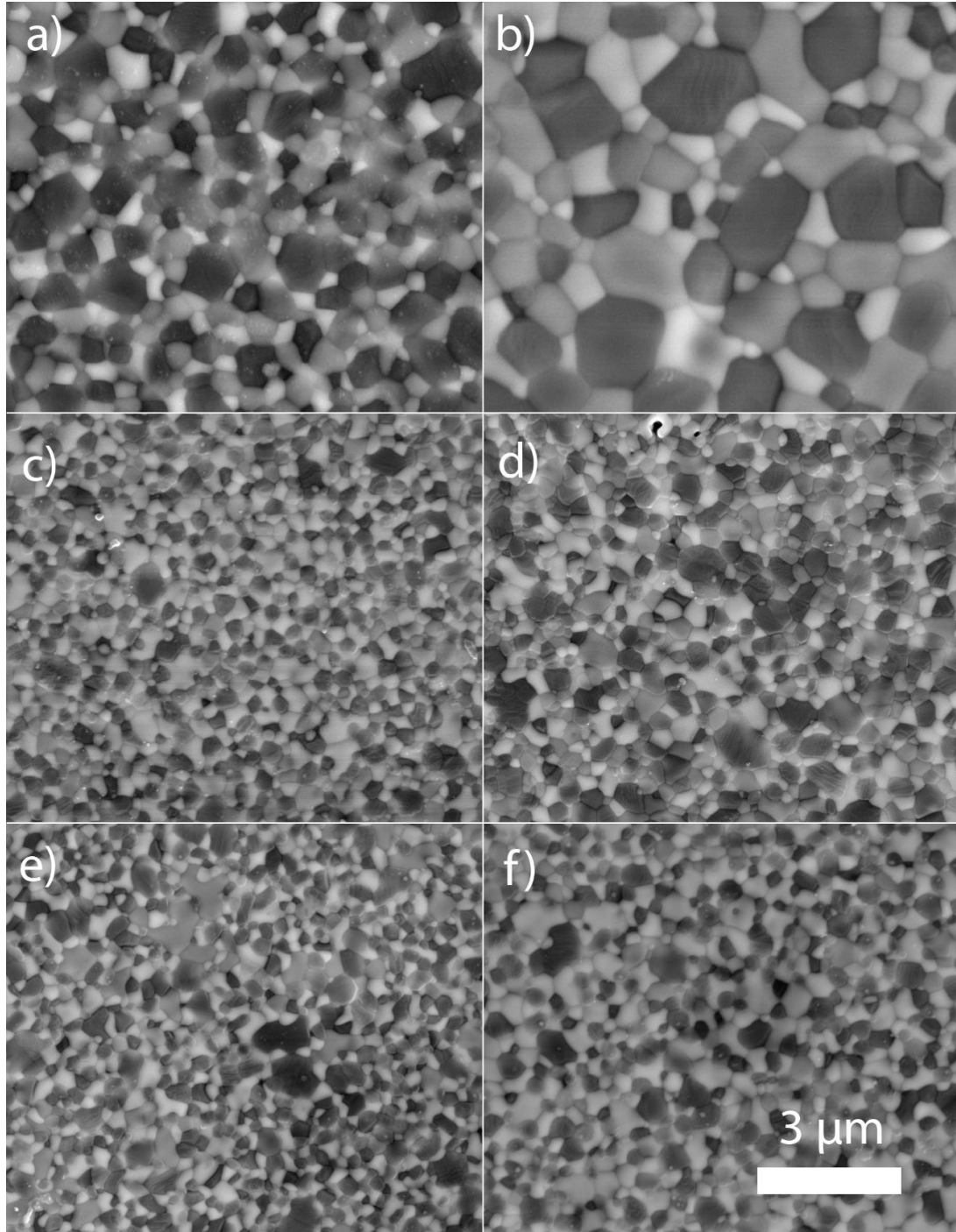
Figure 5.7. Polished SEM micrographs for a) 15 vol % (10 mol %) YSZ nanocomposite b) 15 vol % (10 mol %) YSZ mixed c) 23 vol % (16 mol %) YSZ nanocomposite d) 23 vol % (16 mol %) YSZ mixed e) 32 vol% (23 mol %) YSZ nanocomposite f) 32 vol % (23 mol %) YSZ mixed.

Figure **5.7** shows polished SEM micrographs for all the composites, with AGSs measured for each phase tabulated in Table **5-3**. Phases can be delineated by Z-contrast, with YSZ appearing white, YAG appearing gray, and α-Al_2O_3 appearing black. As dilatometry showed, densification up to 1500° C increases as ZrO_2 content increases. As the ZrO_2 content increases, lower sintering temperatures were required to reach at least 95% TD, and is reflected in finer grain sizes. In relative proportion, YSZ generally has the finest grain sizes, followed by YAG and then Al_2O_3. At 32 vol % (23 mol %) YSZ, the average grain size for all three phases is under 410 nm. Although the nanocomposite nanoparticle approach leads to finer grain sizes than the mixed nanoparticle case, the effect is lessened as the ZrO_2 content is increased. The finest grain sizes here, 410±210 nm, are ≈ 100 nm less than the finest grain sizes reported in the literature achieved by pressureless sintering.

Table 5-3. AGSs for individual phases for nanocomposite nanoparticle (NN) and mixed nanoparticle (mix) samples. Sintering schedule required to reach 95-97 %TD also provided.

	Al₂O₃ [nm]	YAG [nm]	YSZ [nm]	Schedule
15 vol% YSZ NN	1200 ± 400	820 ± 320	630 ± 310	1500° C 8 h
15 vol% YSZ Mix	1800 ± 490	1700 ± 360	1200 ± 440	1600° C 4 h
23 vol% YSZ NN	520 ± 170	540 ± 180	500 ± 170	1500° C 8 h
23 vol% YSZ Mix	550 ± 200	550 ± 170	550 ± 260	1500° C 8 h
32 vol% YSZ NN	410 ± 210	410 ± 180	340 ± 170	1400° C 8 h
32 vol% YSZ Mix	510 ± 190	450 ± 220	440 ± 180	1500° C 4 h

5.3.4 Vickers microhardness

Vickers microhardness measurements were taken on samples of each composition and tabulated in **Table 5-4**. The microhardness doesn't vary much with composition, with all samples within a 0.6 GPa range. In Chapter 4, we saw significant shift in hardness with

composition, which we attributed to alumina dominating the observed hardness values. Here we do not see the same effect, although here the change in vol % Al_2O_3 across the three compositions is $\Delta12$ vol %, where in Chapter 4 it was $\Delta37$ vol %. For the same composition as the 23 vol % YSZ composite, Oelgardt et al obtain hardnesses ranging from 16-19 GPa, slightly above the hardness measured here at equivalent grain sizes obtained by pressureless sintering.[8] As in Chapter 4, the hardness is likely dominated by the Al_2O_3 volume fraction, which agrees with the hardnesses here that are well above those of YSZ (12.3 GPa) or YAG (13.7 GPa).[12]

Table 5-4. Vickers microhardness for each composition (NN = nanocomposite nanoparticle, Mix = mixed nanoparticle).

	Hardness [GPa]
15 vol% YSZ NN	16.0 ± 0.9
15 vol% YSZ Mix	16.2 ± 1.4
23 vol% YSZ NN	15.7 ± 1.4
23 vol% YSZ Mix	15.6 ± 0.5
32 vol% YSZ Mix	15.4 ± 0.5
32 vol% YSZ Mix	15.6 ± 1.5

The results show nanocomposite nanopowders sinter to higher densities at lower temperatures giving finer grain sizes at than mixed nanopowders at equivalent densities or 95 %TD. This is in contrast to Chapters 3 and 4, in which the mixed nanopowder processing approach gave better results. In this case, the bottom up approach to composites was the optimal processing strategy. In the mixed nanoparticle approach, initial phase separation obtained from ball milling gives a minimum separation distance of the particle sizes or ~ 40 nm. The maximum phase separation is likely on the scale of the agglomerate size, which could be 100-800 nm. In the nanocomposite nanoparticle processing approach, the maximum phase separation distance is less than the average particle size of 40 nm. These

results imply phase separation on the nanoscale during sintering does have a significant effect on the final microstructure of the composite, despite significant microstructure coarsening. From a different perspective, we can calculate the approximate number of nanoparticles needed to represent the final volume of the three phases in the dense composite using the average grain sizes and average particle sizes for the nanocomposite nanoparticle 32 vol % YSZ composition. Assuming that grains are tetradecahedral, the volume of a tetradecahedron is given by Eq. 1, where D, the average grain size, is related to the tetradecahedron edge length, l, by the relationship $D = 3l$.[13]

Equation 2 $$V = 8\sqrt{2}l^3$$

Assuming spherical particles, we find an approximate volume coarsening ratio of 8000. This means for the finest grain sizes obtained here, three adjacent grains of separate phases started from an average of 8000 nanostructured nanoparticles. This figure illustrates the novelty of the difference observed between the two processing approaches. The finest grain sizes for YAG-Al_2O_3-YSZ in the composites also start with powders < 100 nm, giving a similar volume coarsening ratio from the green body.

Although the intermediate sintering mechanisms are unclear, it is clear that the addition of ZrO_2 is important in reducing the grain size, as the grain sizes (410 nm) here are much less than the > 1 μm AGSs presented for α-Al_2O_3/YAG composites in Chapter 4. For the nanocomposite particle case, the initial finer length scale of mixing may allow YSZ coalescence which promotes sintering in the 1200-1300° C range leading to higher final densities after the second significant densification regime of 1350-1500° C. Alternatively, the pinning effect of the third phase on the finest length scale, i.e. within the same

nanoparticle, may become an important factor where it was not a factor in two-phase composites produced in Chapter 2.

5.4 Conclusions

The bottom up approach postulates that best global properties are obtained from synthesis processes that start at the finest possible size. This approach, vis-à-vis the length scale of mixing, was tested here through two processing schemes, mixed single metal-oxide nanopowders, and nanocomposite nanopowders have the desired composition within single particles. We find that in the Al_2O_3-Y_2O_3-ZrO_2 ternary system, composites prepared from nanostructured nanoparticles sinter to finer grain sizes at equivalent densities of 95 %TD than those prepared from mixed nanoparticle processing. These results stand in contrast to Chapters 3 and 4, where mixed nanoparticle processing gave the best results. The final microstructures for both processing schemes consist of well dispersed composite phases.

Another major finding is clear evidence observed by TEM of nanostructured nanoparticles containing the metastable $YAlO_3$ and δ^*-Al_2O_3 phases along with c-YSZ. These are the first LF-FSP ternary phase particles directly observed to have such structure. Nanostructured nanoparticles are a promising avenue for LF-FSP studies, as intra-particle interfaces may give rise to novel properties. In Chapter 7, we investigate the general parameters of particle formation in LF-FSP and two more cases of nanostructured nanoparticle formation.

In Chapter 6, we apply the same processing approaches to $MAlO_4$/α-Al_2O_3 composites, where M = Mg, Co, and Ni. Unlike the ternary phase single particles used here, we began

with single phase metastable Al_2O_3 rich spinel particles, monitoring the exosolution of

Al_2O_3 and its impact on densification.

References

[1] D. Men and M.L. Mecartney, "Superplasticity and machinability in a four-phase ceramic," *Materials Research Bulletin*, **47** [8] 1925–1931 (2012).

[2] M. Kim and R.M. Laine, "Pressureless Sintering t-zirconia@δ-Al_2O_3 (54 mol%) Core–Shell Nanopowders at 1120°C Provides Dense t-Zirconia-Toughened α-Al_2O_3 Nanocomposites," *Journal of the American Ceramic Society*, **93** [3] 709–715 (2010).

[3] H. Su, J. Zhang, J. Yu, L. Liu, and H. Fu, "Rapid solidification and fracture behavior of ternary metastable eutectic Al_2O_3/YAG/YSZ in situ composite ceramic," *Materials Science and Engineering: A*, **528** [4–5] 1967–1973 (2011).

[4] F.J. Ester, A. Larrea, and R.I. Merino, "Processing and microstructural study of surface laser remelted Al_2O_3–YSZ–YAG eutectic plates," *Journal of the European Ceramic Society*, **31** [7] 1257–1268 (2011).

[5] J.M. Calderon-Moreno and M. Yoshimura, "Al_2O_3–$Y_3Al_5O_{12}$(YAG)–ZrO2 ternary composite rapidly solidified from the eutectic melt," *Journal of the European Ceramic Society*, **25** [8] 1365–1368 (2005).

[6] P.B. Oliete, J.I. Peña, A. Larrea, V.M. Orera, J. LLorca, J.Y. Pastor, A. Martín, and J. Segurado, "Ultra-High-Strength Nanofibrillar Al_2O_3–YAG–YSZ Eutectics," *Adv. Mater.*, **19** [17] 2313–2318 (2007).

[7] P. Palmero, V. Naglieri, G. Spina, M. Lombardi, *Ceramics International* **2011**, *37*, 139.

[8] C. Oelgardt, J. Anderson, J.G. Heinrich, and G.L. Messing, "Sintering, microstructure and mechanical properties of Al2O3–Y2O3–ZrO2 (AYZ) eutectic composition ceramic microcomposites," *Journal of the European Ceramic Society*, **30** [3] 649–656 (2010).

[9] D.-K. Kim and W.M. Kriven, "Processing and Characterization of Multiphase Ceramic Composites Part II: Triplex Composites with a Wide Sintering Temperature Range," *Journal of the American Ceramic Society*, **91** [3] 793–798 (2008).

[10] S.-M. Sim, K.A. Keller, and T.-I. Mah, "Phase formation in yttrium aluminum garnet powders synthesized by chemical methods," *Journal of Materials Science*, **35** [3] 713–717 (2000).

[11] T. Hinklin, B. Toury, C. Gervais, F. Babonneau, J.J. Gislason, R.W. Morton, and R.M. Laine, "Liquid-Feed Flame Spray Pyrolysis of Metalloorganic and Inorganic Alumina Sources in the Production of Nanoalumina Powders," *Chem. Mater.*, **16** [1] 21–30 (2004).

[12] A. Larrea, V.M. Orera, R.I. Merino, and J.I. Peña, "Microstructure and mechanical properties of Al_2O_3–YSZ and Al_2O_3–YAG directionally solidified eutectic plates," *Journal of the European Ceramic Society*, **25** [8] 1419–1429 (2005).

[13] M.I. Mendelson, "Average Grain Size in Polycrystalline Ceramics," *Journal of the American Ceramic Society*, **52** [8] 443–446 (1969).

Chapter 6

Dense MAl₂O₄/α-Al₂O₃ (M = Ni, Co, Mg) composites

from single phase spinels and mixed MAl₂O₄ + Al₂O₃ nanopowders

6.1 Introduction

Developing a detailed understanding of diffusion processes is one of the most important facets in properties optimization in ceramics science and engineering. The opportunity to start from nano-oxide powders that are atomically mixed offers the potential to develop unique perspectives about these processes when sintering to produce dense monoliths. A further opportunity presents itself when the nanopowders have compositions outside traditional thermodynamic phase diagrams, as observed in liquid-feed flame spray pyrolysis (LF-FSP) nanopowders. Given that the powders are crystalline yet metastable, the potential exists to study phase-segregation without passing through chemically derived precursors that must be calcined prior to sintering, such as in sol-gel processing.

In chapters 2 and 5, we described studies along these lines designed to explore the concept of "bottom-up" processing in $Y_3Al_5O_{12}$ compositions made both from atomically mixed nanopowders and ball-milled mixtures of Y_2O_3 and Al_2O_3 nanopowders, and nanopowders with a final composition of $NiO \cdot 3Al_2O_3$. Our findings were that the bottom-up concept was either not the optimal route to the targeted materials with controlled microstructures or gave the same microstructures despite significant differences in levels of mixing.

The bottom-up concept, pervasive in materials science, suggests that the finest scales of mixing should provide the shortest diffusion paths and therefore sintering times to fully dense materials with optimal control of final microstructures. In this study, we extend studies on the initial NiO•$3Al_2O_3$ system and now include two additional spinel systems with M = Mg and Co. Our objective here was to delineate microstructural and phase evolution in much greater detail than in the earlier study.

To this end, we have examined the sintering behavior of disordered MAl_2O_4/Al_2O_3 spinel solutions, in which the disorder gives rise to densification processes and rates different from that of the component systems, likely due to the high defect/vacancy contributions. In addition, we examine sintering of equivalent compositions from ball-milled powders to investigate the role of length scale of mixing in processing dense composites and its influence on control of final densities and microstructures.

$MgAl_2O_4$, $CoAl_2O_4$, and $NiAl_2O_4$ spinels are of significant technological interest for their inherent mechanical, optical, and catalytic properties.[1,2,3,4,5,6,7,8] Nanosized MgAl2O4, $CoAl_2O_4$, and $NiAl_2O_4$ spinel powders have been synthesized using a variety of methods including co-precipitation of metal hydroxides,[9,10] wet impregnation,[10] sol-gel processing,[11] and spray pyrolysis.[12] High surface area (50 m^2/g) spinel powders are of interest for both catalytic applications where surfaces exhibit high activity and sintering of ceramic monoliths in which reduction in surface area provides added driving force for densification.

Metal aluminate spinels having the general formula MAl_2O_4 are a class of materials with a wide range of properties dependent on the divalent cation. Metal aluminates belong to the cubic space group Fd3m. The unit cell is composed of a pseudo-cubic closed packed

oxygen lattice with 64 tetrahedral and 32 octahedral sites for divalent metal and aluminum cations. In normal spinel 1/8 of the tetrahedral sites are filled by divalent atoms and 1/2 of the octahedral sites are occupied by aluminum atoms. In the unit cell of a fully inverted spinel, the aluminum atoms occupy 8 tetrahedral sites and 8 octahedral sites with the remaining 8 octahedral sites occupied by the divalent metal atoms.[13,14,15]

In metal aluminate spinels i, the inversion parameter, is defined as the fraction of tetrahedral sites occupied by aluminum atoms; thus it follows that in a normal spinel $i = 0$ and in a fully inverted spinel $i = 1$. In practice the cation distribution is of a mixed nature with $0 < i < 1$, a function of the octahedral site preference energy (OSPE) of the constituent cations. The OSPE is a measure of the preference of a cationic species to be located on an octahedral site.[16,17]

The spinel structure consists of a rigid anion lattice through which cations diffuse.[18] Diffusional processes are dependent on the mobility of the divalent and trivalent cations through the octahedral and tetrahedral sites formed by the oxygen lattice. From a mechanistic perspective, there are two major interactions to account for when considering cation diffusion. The lattice strain energy imposed by the diffusing cation and the preference of the diffusing cation to occupy a tetrahedral or octahedral site. Therefore the mobility of a specific cation through the spinel oxygen lattice is a function of the cation radii and the OSPE of the cations.[19,20]

Liquid-feed flame spray pyrolysis (LF-FSP) offers access to a variety of metal and mixed metal oxide nanopowders over a wide range of ceramic systems. In LF-FSP, alcohol solutions of metalloorganic precursors are aerosolized with oxygen, combusted, and the resultant nanopowders are collected downstream in electrostatic precipitators.[21]

Combustion produces oxide nanopowders with identical compositions to the precursor solution and high surface area powders due to a rapid quench from flame temperatures of 1200°C-2000°C to downstream temperatures of 300°C-400°C within nanoseconds. The resulting nanopowders are crystalline, having no microporosity, and good dispersability, with average particle sizes (APSs) of 15-40 nm.[22,23,24,25,26,27,28]

Previous work has shown the high quench rate of LF-FSP provides routes to kinetic products. In the case of certain $MO-Al_2O_3$ [M = Mg, Co, Ni] systems, LF-FSP can produce single-phase MAl_2O_4 powders at Al_2O_3-rich compositions well outside the thermodynamically defined single-phase region. The Al_2O_3-rich MAl_2O_4 materials are single-phase and can be considered a solid solution of the isostructural phases, γ-Al_2O_3 and MAl_2O_4.[29]

Here we use single-phase $MO \cdot 3Al_2O_3$ powders to form Al_2O_3/MAl_2O_4 composites and com-pare the sintering behavior to ball-milled Al_2O_3 and MAl_2O_4 powders to investigate the effects of length scale of mixing on the sintering behavior of Al_2O_3/MAl_2O_4 composites. We then further examine the sintering behavior of the single-phase Al_2O_3-rich MAl_2O_4 powders in the context of the transition from a single-phase material to a duplex Al_2O_3/MAl_2O_4 composite.

6.2 Experimental

Cobalt propionate was used as a precursor for CoO. Alumatrane was used as precursor to Al_2O_3. Nickel acetate was used as a precursor to NiO. Magnesium acetate was used as a precursor to MgO.

6.3   Results and discussion

As noted above, we are interested in the microstructural evolution of $MO \cdot 3Al_2O_3$ (M = Mg, Co, and Ni) using nanopowders that offer a homogeneous composition at atomic length scales versus, mixtures of nanopowders of the same composition but with homogeneity defined by ball-milling of the same ratios of the two component nanooxide powders. In all instances the nanopowders used offer average particle sizes (APSs) of $\approx$ 30-40 nm. In the latter case, we believe that the homogeneity of mixing is submicron rather that atomic. Our goal has been to explore the potential utility of the "bottom up" synthesis paradigm to processing of bulk ceramics from nanopowders.[30]

Starting powders were synthesized by LF-FSP which provides a route to both atomically –mixed, single-phase Al_2O_3 – rich MAl_2O_4 [M = Mg, Co, Ni], hereafter referred to as $NiO \cdot 3Al_2O_3$, and stoichiometric MAl_2O_4 which was ball-milled with Al_2O_3 to produce materials of equivalent composition, hereafter referred to as $MAl_2O_4 + Al_2O_3$.

6.3.1   Powder Characterization

SEM was performed on all as-produced powders to assess the homogeneity of particle sizes and determine particle morphology. Powders were agglomerated due to electrostatic interactions but contained no micron-sized particles. The particles appeared largely homogenous in terms of particle size and spherical morphology. Figure **6.1** shows as-produced $MgO \cdot 3Al_2O_3$ powders, representative of all LF-FSP materials produced in this study. Figure **6.2** shows a HRTEM image of the as-produced $NiO \cdot 3Al_2O_3$ powders.
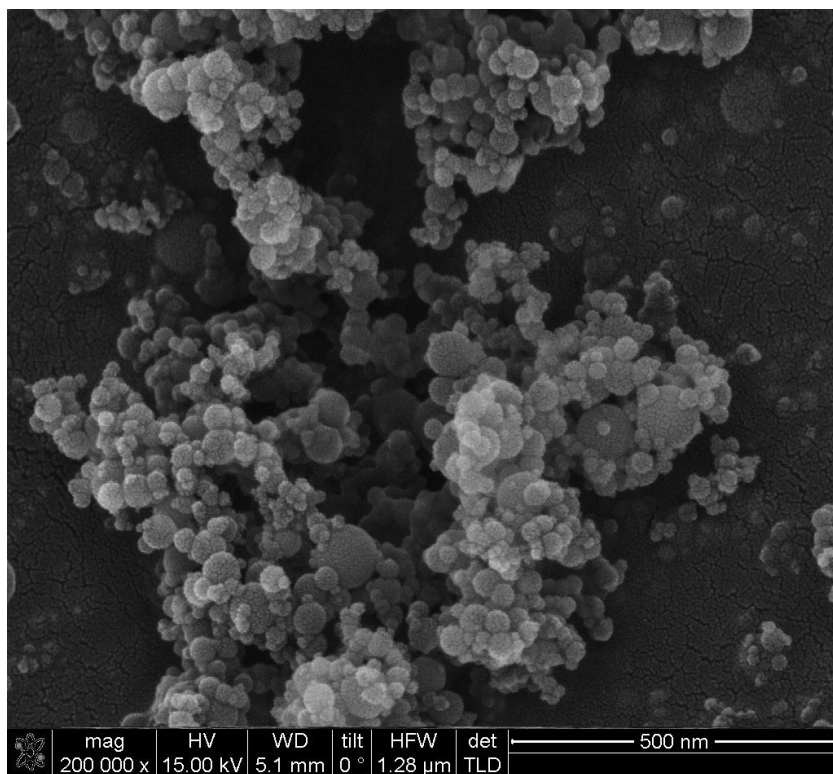
Figure 6.1. SEM micrograph of MgO•3Al$_2$O$_3$.
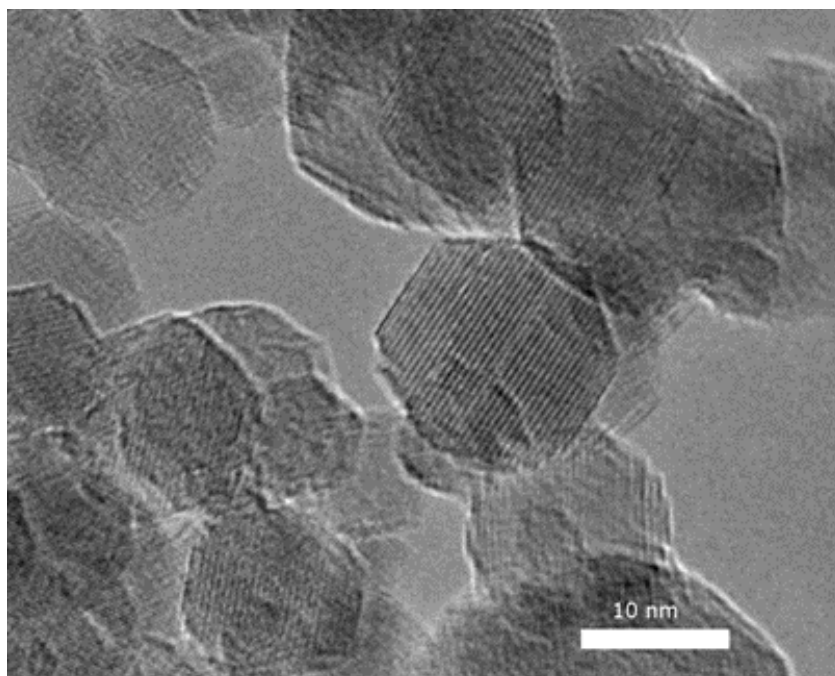
Figure 6.2. TEM micrograph of MgO•3Al$_2$O$_3$.

Table 1 presents SSAs of the as-produced powders. No hysteresis was observed in the BET adsorption/desorption isotherms indicating that the particles had no surface porosity.

Figure **6.3** shows powder XRD patterns for as-produced MO•3Al$_2$O$_3$ powders. As-produced powders are single phase and can be considered solid solutions of γ-Al$_2$O$_3$ and MAl$_2$O$_4$ as γ-Al$_2$O$_3$ has a defect spinel structure.[31,32] XRD patterns taken with Si (111) standards were used to determine the lattice parameters of the as-produced powders. The lattice parameters were found to be 7.99 Å for MgO•3Al$_2$O$_3$, 8.01 Å for CoO•3Al$_2$O$_3$, and 7.98 Å for NiO•3Al$_2$O$_3$, which correspond to points at 48% along the Al$_2$O$_3$-MgAl$_2$O$_4$ tie line, 54% along the Al$_2$O$_3$-CoAl$_2$O$_4$ tie line, and 51% along the Al$_2$O$_3$-NiAl$_2$O$_4$ tie line. The powders are generally in good agreement with the predicted lattice parameter as determined by Vegard's law of a 1:1 solid solution of γ-Al$_2$O$_3$ and MAl$_2$O$_4$.
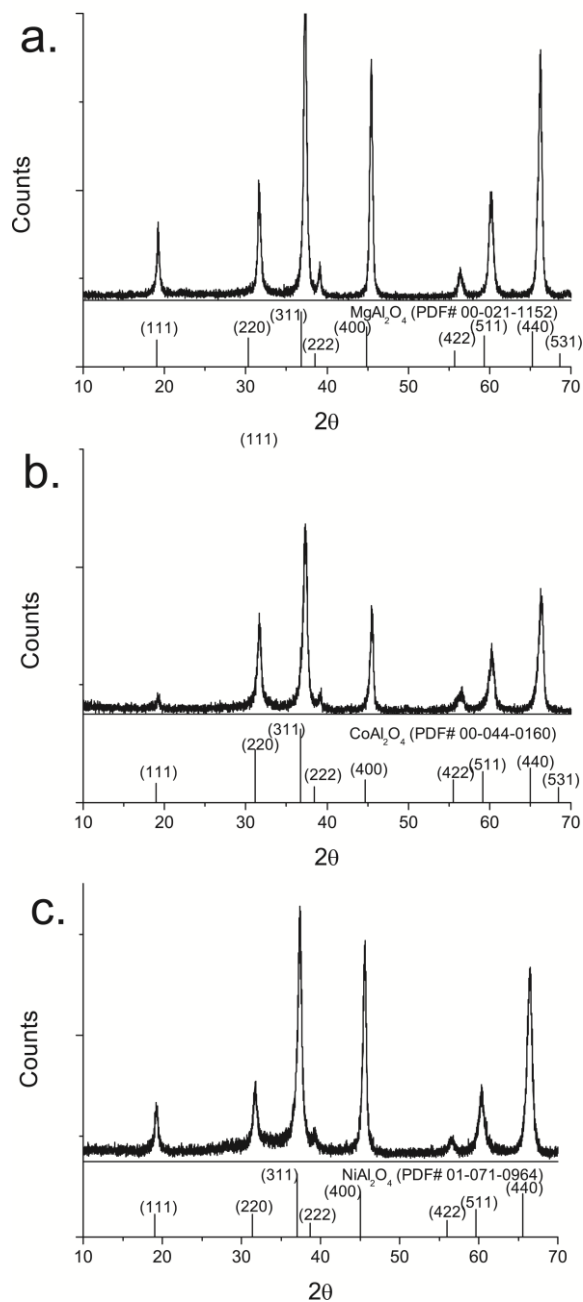
Figure 6.3. XRD patterns of as-produced MO•3Al$_2$O$_3$ powder with PDF for **a**. MgO•3Al$_2$O$_3$ **b**. CoO•3Al$_2$O$_3$ **c**. NiO•3Al$_2$O$_3$.

Although the deviations from Vegard's law are less than ± 4%, there is evidence to suggest the spinel inversion parameter can affect the lattice parameter in MgAl$_2$O$_4$.[33] Given the kinetic nature of particle formation in LF-FSP, the MgAl$_2$O$_4$ may have

significantly higher inversion than spinel synthesized by other methods. The deviation from Vegard's law could also arise from small stoichiometry deviations due to inhomogeneous precursors.

6.3.2 Final Microstructures

Samples of $MO \cdot 3Al_2O_3$ and $MAl_2O_4 + Al_2O_3$ were subjected to two sintering schedules both targeting practical densities of $\geq 95\%$ of theoretical density in all materials. The low temperature schedule (LT) with holds at 1150 °C - 4 h, 1300 °C - 8 h, and 1400 °C - 4h was intended to minimize grain growth during densification. The results are compared with a high temperature schedule (HT) comprised of a single hold at 1400 °C for 10 h. All sintering was performed in air as initial studies under O_2, N_2, and vacuum were found to have no effect on densification behavior. Figure **6.4** shows microstructures for $MgO \cdot 3Al_2O_3$ and $MgAl_2O_4 + Al_2O_3$ sintered at the HT and LT schedules. These microstructures are typical of all three systems studied. Figure **6.5** shows microstructures for $CoO \cdot 3Al_2O_3$ and $CoAl_2O_4 + Al_2O_3$ sintered at the HT and LT schedules. Figure **6.6** shows final microstructures for $NiO \cdot 3Al_2O_3$ and $NiAl_2O_4 + Al_2O_3$ sintered at the HT and LT schedules.
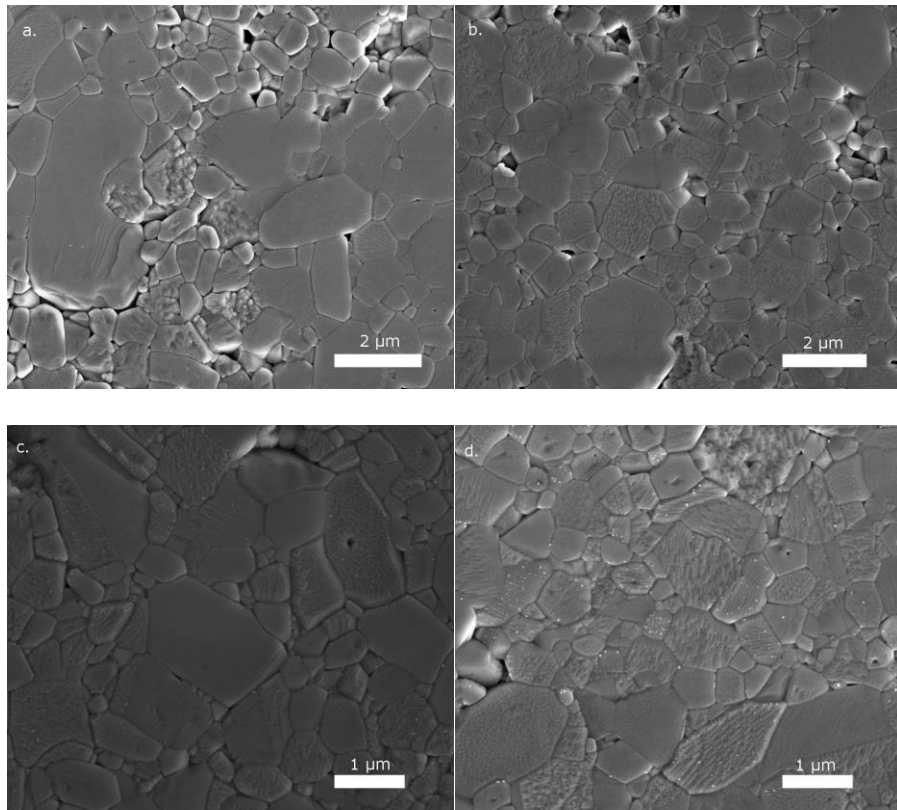
Figure 6.4. SEM micrographs of polished MgAl2O4 pellets **a**. MgO•3Al$_2$O$_3$ HT, **b**. MgAl$_2$O$_4$ + Al$_2$O$_3$ HT.
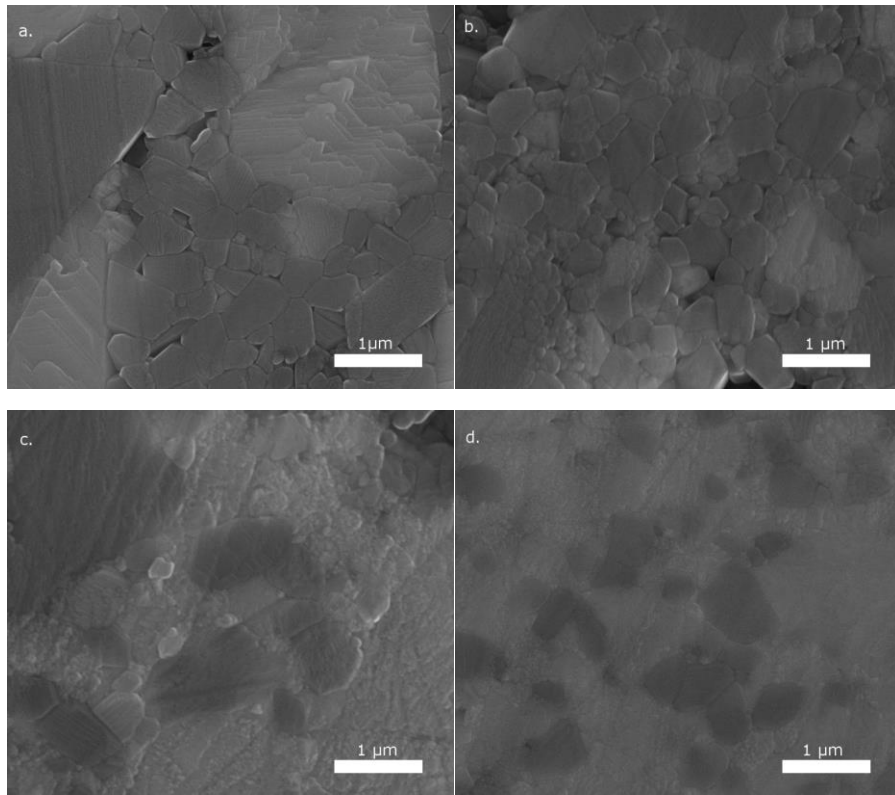
Figure 6.5. SEM micrographs of polished $CoAl_2O_4$ pellets a. $CoO \cdot 3Al_2O_3$ HT, b. $CoO \cdot 3Al_2O_3$ LT, c. $CoAl_2O_4 + Al_2O_3$ HT, d. $CoAl_2O_4 + Al_2O_3$ LT.
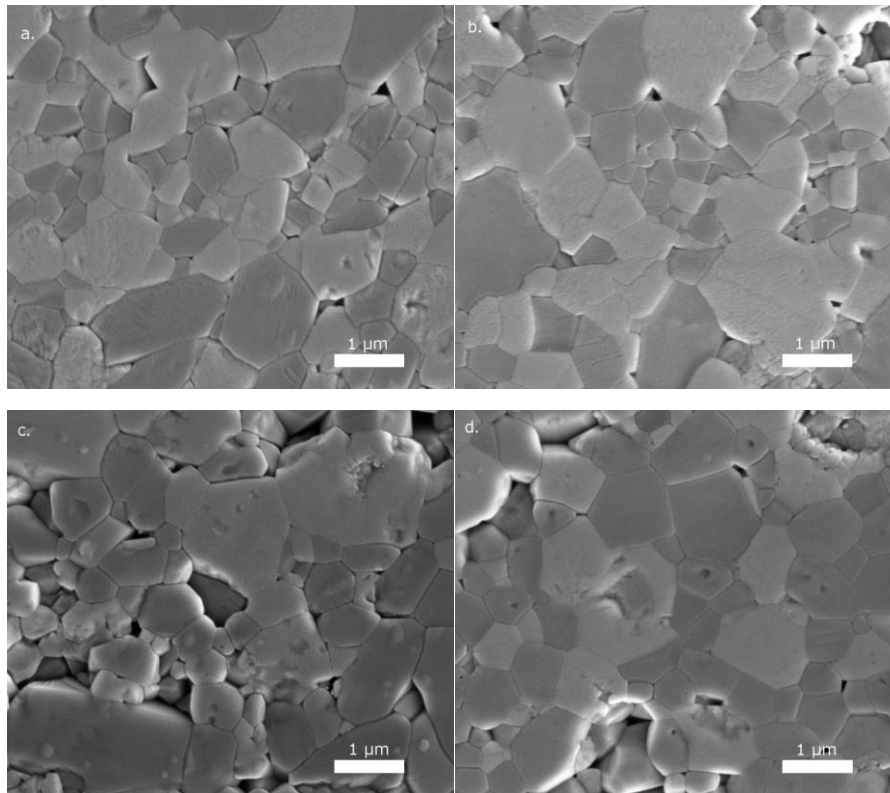
Figure 6.6. SEM micrographs of polished $NiAl_2O_4$ pellets a. $NiO \cdot 3Al_2O_3$ HT, b. $NiO \cdot 3Al_2O_3$ LT, c. $NiAl_2O_4 + Al_2O_3$ HT, d. $NiAl_2O_4 + Al_2O_3$ LT.

Average grain sizes (AGSs) were measured by the lineal intercept method. Included in the grain size plots of Figure **6.7**, Figure **6.8**, and Figure **6.9** are the 95% confidence interval (box) and variance (bars) of measurements taken for each sample.

With the exception of the ball-milled $NiAl_2O_4 + Al_2O_3$ samples, the lower temperature sintering schedule reduces the AGS by 240 nm ± 150 nm. However, the differences between the AGSs of the LT and HT samples are within the 95% confidence interval. Thus, the size difference is not statistically significant except in the case of the $MgO \cdot 3Al_2O_3$, where the single, high temperature sintering step results in grain sizes significantly larger than that of the low temperature sintering schedule. In this case, the high temperature sintering step may be above a temperature at which significant grain coarsening occurs.
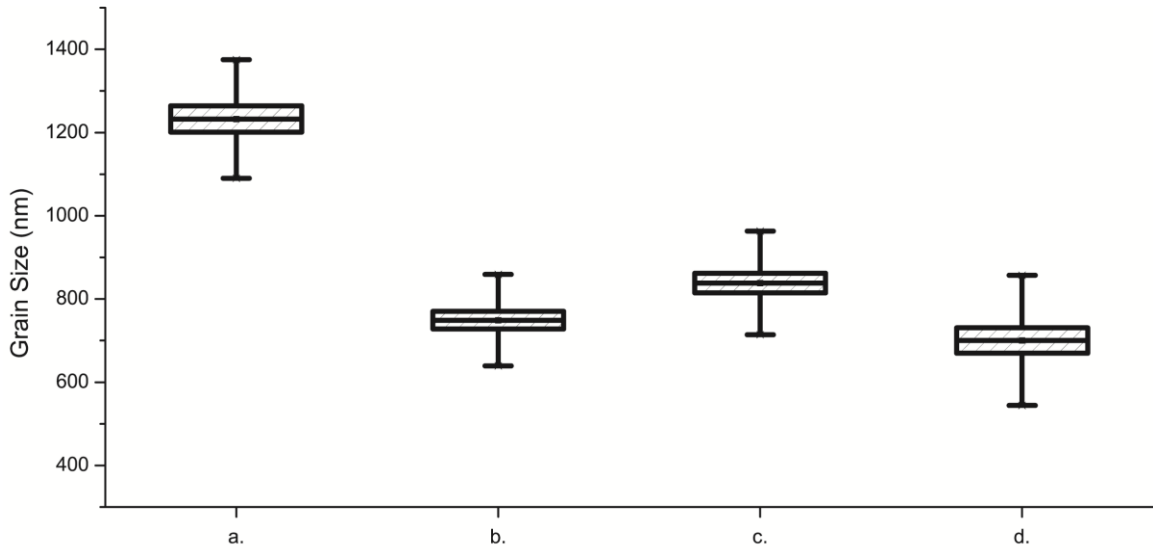
Figure 6.7. Grain sizes of Al_2O_3 – $MgAl_2O_4$ composites **a**. $MgO \cdot 3Al_2O_3$ HT, **b**. $MgO \cdot 3Al_2O_3$ LT, **c**. $MgAl_2O_4$ + Al_2O_3 HT, **d**. $MgAl_2O_4$ + Al_2O_3 LT.
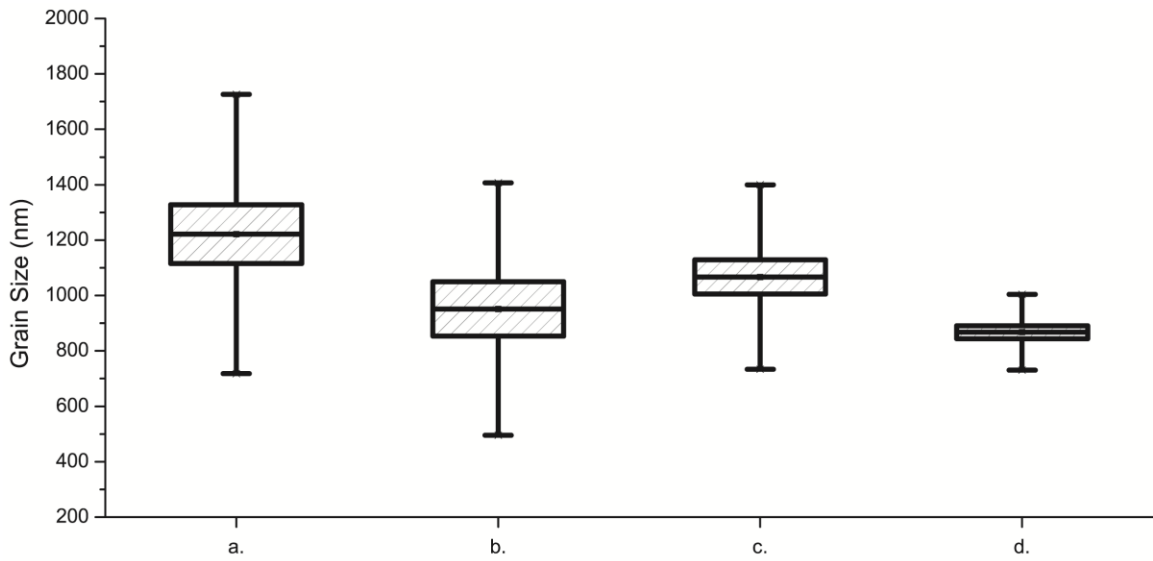
Figure 6.8. Grain sizes of Al_2O_3 - $CoAl_2O_4$ composites **a**. $CoO \cdot 3Al_2O_3$ HT, **b**. $CoO \cdot 3Al_2O_3$ LT, **c**. $CoAl_2O_4$ + Al_2O_3 HT, **d**. $CoAl_2O_4$ + Al_2O_3 LT.
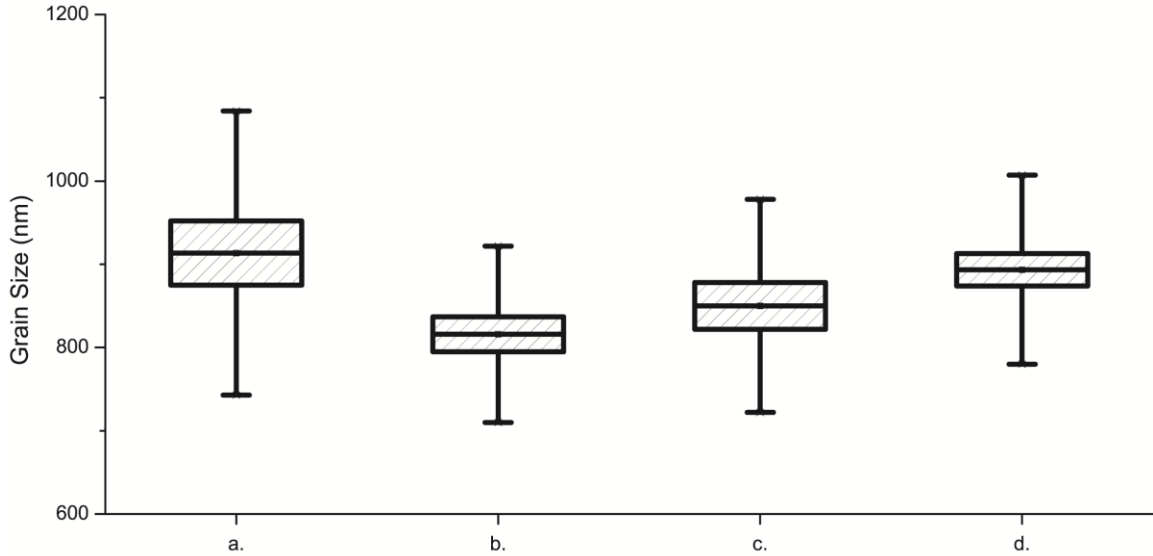
Figure 6.9. Grain sizes of Al_2O_3 - $NiAl_2O_4$ Composites **a**. $NiO \cdot 3Al_2O_3$ HT, **b**. $NiO \cdot 3Al_2O_3$ LT, **c**. $NiAl_2O_4 + Al_2O_3$ HT, **d**. $NiAl_2O_4 + Al_2O_3$ LT.

Surprisingly, samples made from the ball-milled $MAl_2O_4 + Al_2O_3$ powders produce compacts with AGSs equivalent to samples made from the atomically-mixed $MO \cdot 3Al_2O_3$ powder. This finding implies that mixing of constituent powders at atomic length scales does not correspond to finer grain sizes in the final microstructures of dense composites when compared to mixing at nanometer length scales. This observation seems counter to the widely accepted bottom up approach to processing that has been widely accepted throughout the literature.[30]

6.3.3   Phase exsolution and sintering behavior

The effects of exsolution on the sintering behavior of $MO \cdot 3Al_2O_3$ compacts were investigated by combined dilatometry and XRD studies of powders heated at 10 °C/min/air to selected temperatures with a 1 h dwell. The ramp rate for heating of all XRD samples was 10 °C/min.

100

Figure **6.10** and Figure **6.11** present XRD and dilatometry data for $CoO•3Al_2O_3$ and

$MgO•3Al_2O_3$, respectively. Here we observe $\alpha-Al_2O_3$ and MAl_2O_4 [M = Mg and Co]

exsolution directly from the as-produced Al_2O_3-rich MAl_2O_4. Dilatometry curves for these

two materials indicate similar, two stage, sintering behavior with the onset of densification

for the $CoO•3Al_2O_3$ and $MgO•3Al_2O_3$ at 1050 °C and 1160 °C respectively. In both

systems, considerable densification, approximately 20% TD (theoretical density) by

dilatometry, occurs prior to exsolution of $\alpha-Al_2O_3$, and the densification rate slows

significantly coincident with exsolution. It is likely that the $\alpha-Al_2O_3$ greatly slows sintering

following exsolution, either through slower sintering kinetics or by presenting a physical

barrier. A similar enhancement in densification in Al_2O_3 rich spinels was seen by Krell et

al.[34] in which sintering of $MgO•nAl_2O_3$ was promoted in samples where n > 1.5, although

n = 3.0 in this study, representing a significantly higher Al_2O_3 content.
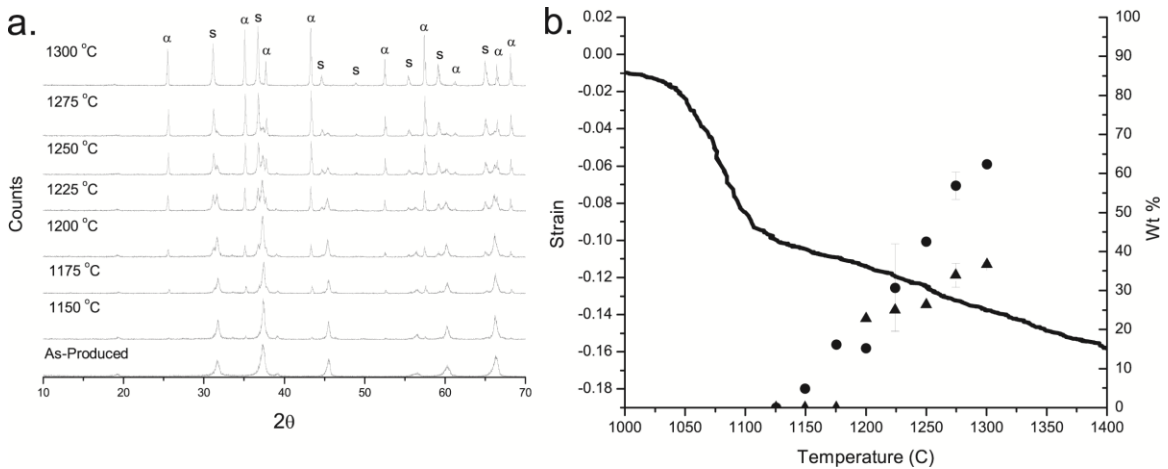
Figure 6.10. **a**. XRD results of phase separation of $\alpha-Al_2O_3$ (α) and $CoAl_2O_4$ (S) from $CoO•3Al_2O_3$ powders heated for 1 h. **b**. $CoO•3Al_2O_3$ dilatometry results plotted with amount of $\alpha-Al_2O_3$ (•) and $CoAl_2O_4$ (▲) from XRD patterns of powders heated for 1 h.
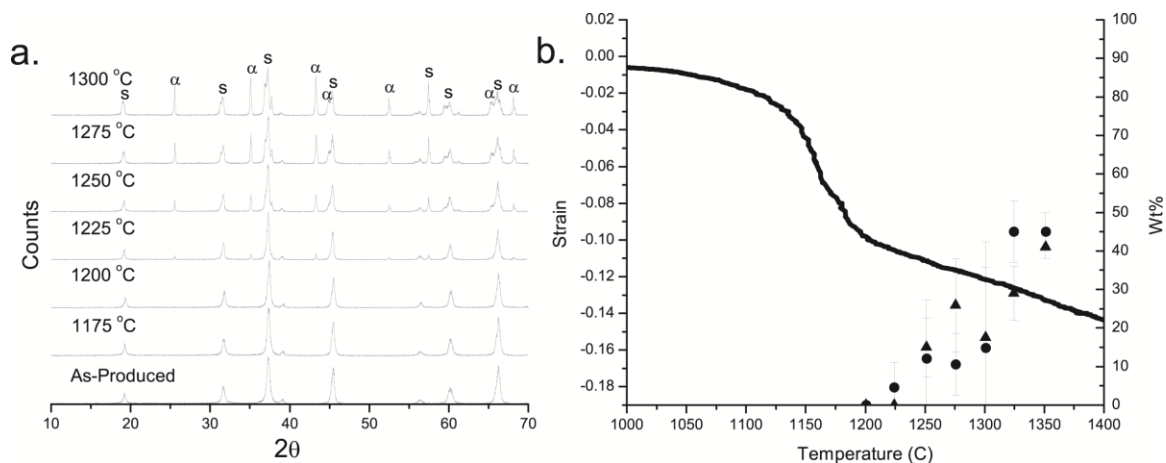
Figure 6.11. **a**. XRD results of phase separation of α-Al$_2$O$_3$ (α) and MgAl$_2$O$_4$ (S) from MgO•3Al$_2$O$_3$ powders heated for 1 h. **b**. MgO•3Al$_2$O$_3$ dilatometry results plotted with amount of α-Al$_2$O$_3$ (•) and MgAl$_2$O$_4$ (▲) from XRD patterns of powders heated for 1 h.
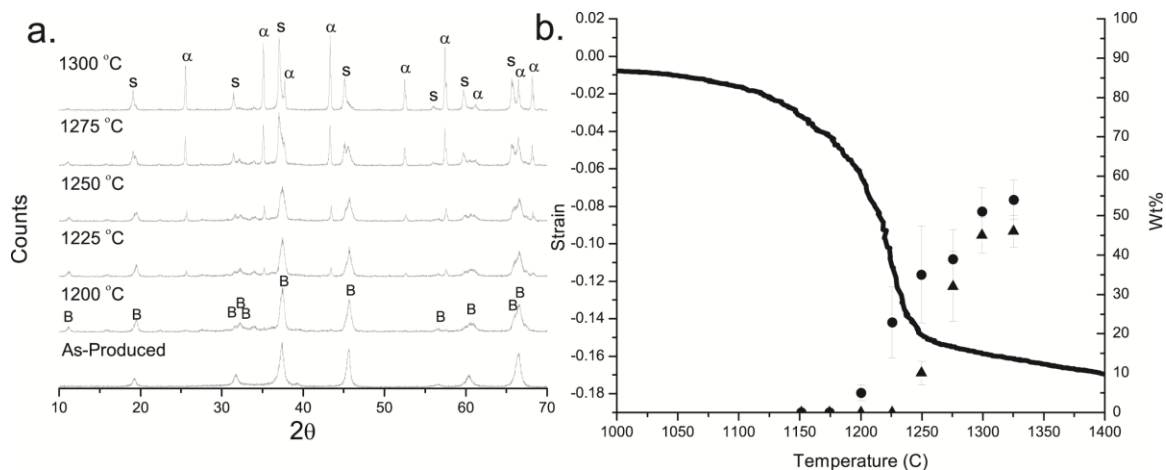
Figure 6.12. **a**. XRD results of phase separation of NiAl$_{10}$O$_{16}$ (B), α-Al$_2$O$_3$ (α) and NiAl$_2$O$_4$ (S) from NiO•3Al$_2$O$_3$ for powders heated for 1 h. **b**. NiO•3Al$_2$O$_3$ dilatometry results plotted with amount of α-Al$_2$O$_3$ (•) and NiAl$_2$O$_4$ (▲) from XRD patterns from powders heated for 1 h.

Figure **6.12** shows the XRD and dilatometry for NiO•3Al$_2$O$_3$. In the case of NiO•3Al$_2$O$_3$, an intermediate phase, NiAl$_{10}$O$_{16}$, forms prior to separation of α-Al$_2$O$_3$ and NiAl$_2$O$_4$. Bassoul and Gilles report that NiAl$_{10}$O$_{16}$ is monoclinic and exhibits a periodic antiphase boundary structure based on the (100)c plane of the NiAl$_2$O$_4$ structure.[35,36] Here we observe conversion of NiO•3Al$_2$O$_3$ to NiAl$_{10}$O$_{16}$ before phase separation of α-Al$_2$O$_3$

and, unlike the cobalt and magnesium systems, phase separation of Al_2O_3 does not immediately hinder densification, as seen in the combined dilatometry/XRD plots. The $NiAl_{10}O_{16}$ phase is Ni deficient compared to the original $NiO \cdot 3Al_2O_3$ composition, meaning the remaining spinel phase must be Ni rich. The conversion of the $NiO \cdot 3Al_2O_3$ material to $NiAl_{10}O_{16}$ is likely why densification continues after α-Al_2O_3 nucleates, in contrast to the cobalt and magnesium systems, where densification is slowed. To our knowledge, the sintering behavior of the metastable $NiAl_{10}O_{16}$ has not been studied.

Although the $NiAl_{10}O_{16}$ was previously described by Bassoul and Gilles, relatively few studies on this phase exist because it is difficult to access except in bulk. The work reported here, offers, for the first time, simple access to this phase from nanopowders, which may allow future researchers to explore their properties including for example, catalytic behavior.

Table 2 contains the dilatometry results for the first densification regime across all three systems. The $CoO \cdot 3Al_2O_3$ shows the lowest amount of densification in the initial densification regime, approximately 20% TD. The dilatometry trace for $MgO \cdot 3Al_2O_3$ is similar to that of the $CoO \cdot 3Al_2O_3$, but shows approximately 24% TD densification. As previously discussed, the $NiO \cdot 3Al_2O_3$ does not densify until after exsolution begins, with approximately 33% TD densification during the initial densification regime.

In a previously published study on $NiO \cdot 3Al_2O_3$, we looked at the degree of mixing of the starting materials vs. the final microstructure and densities. The current study represents a more in depth look at the sintering behavior of $NiO \cdot 3Al_2O_3$ throughout the exsolution process, which is shown by dilatometry to differ from that of the $MgO \cdot 3Al_2O_3\neg$ and $CoO \cdot 3Al_2O_3$ systems.

Diffusion in stoichiometric spinels is governed by oxygen mobility, which is reported to be several orders of magnitude smaller than the cation mobility.[37,38] However, the kinetic nature of the as-produced $MO\cdot 3Al_2O_3$ powders necessitates rearrangement of the cations to form the thermodynamically favored α-Al_2O_3/MAl_2O_4 composite. The as-produced powders likely deviate from the thermodynamically favored inversion levels due to the rapid quenching of LF-FSP. Since astoichiometry in Al_2O_3 rich spinels creates 1/8 cation vacancy per additional Al,[39,40] the Al_2O_3 rich materials studied here have a high number of cation vacancies. The role of cation vacancies in altering the densification behavior of these materials was investigated by comparing dilatometry curves of the component oxides, Al_2O_3 and MAl_2O_4, with the Al_2O_3-rich $MO\cdot 3Al_2O_3$, materials (Figure **6.13**).
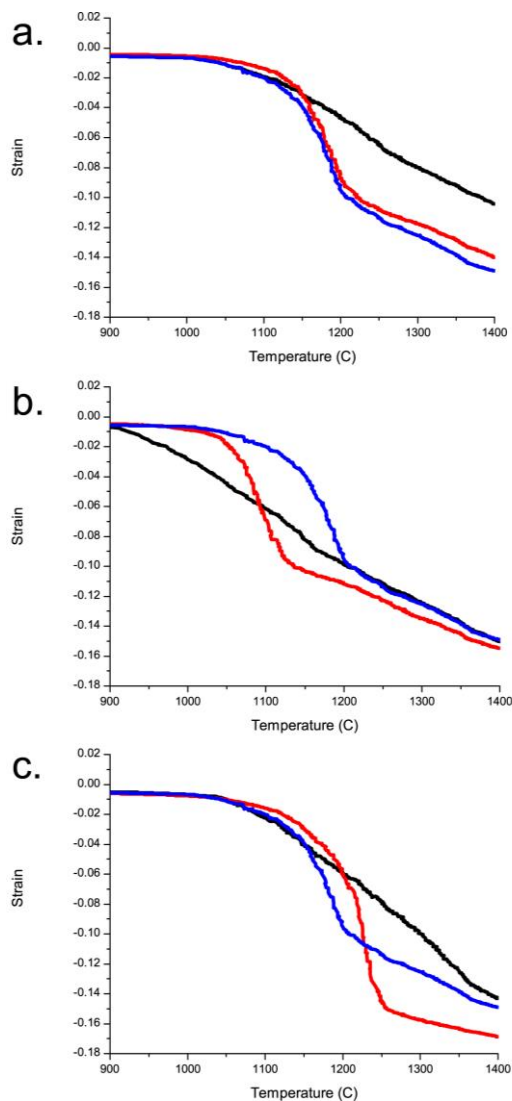
Figure 6.13. Dilatometry curves of Al_2O_3 (blue) and MAl_2O_4 (black), and $MO \cdot 3Al_2O_3$ (red) for **a**. M = Mg **b**. M = Co and **c**. M = Ni.

    The dilatometry results indicate that the initial onset of densification scales with the onset of densification for the respective stoichiometric MAl_2O_4. This is most pronounced in the cobalt sys-tem where we observe sintering of the $CoAl_2O_4$ at just above 900 °C and a much earlier onset of densification, 1050 °C, for $CoO \cdot 3Al_2O_3$ when compared to 1130 °C and 1160°C for $NiO \cdot 3Al_2O_3$ and $MgO \cdot 3Al_2O_3$ respectively.

Comparison of the densification behavior of Nanotek 70:30 δ/γ-Al_2O_3 with those of the MO•$3Al_2O_3$ materials seem to indicate that part of the initially enhanced densification the first densification regime, in the MO•$3Al_2O_3$ materials could arise due to the γ-Al_2O_3 to α-Al_2O_3 transformation. In the Nanotek δ/γ-Al_2O_3, the steep initial densification regime shown in blue in Figure 10 coincides with the γ-Al_2O_3 to α-Al_2O_3 phase transformation. The -0.06 linear strain in this densification region is larger than theory for the transformation, -0.034, indicating some densification coincides with the transformation. However, since XRD studies of the magnesium and cobalt materials do not show α-Al_2O_3 until after the as-produced powders enter the second densification regime, we argue that the first densification regime in these systems is likely a result of cation rearrangement in the MO•$3Al_2O_3$, enhanced by the high concentration of cation vacancies.

Given only that the Al_2O_3 content of the three materials is the same, the cation vacancy con-centration should be similar between these materials, however, the octahedral site preference of the divalent cation varies between the three materials such that $Ni > Co > Mg$ implying an in-creasing degree of inversion between the materials studied such that MgO•$3Al_2O_3$ < CoO•$3Al_2O_3$ < NiO•$3Al_2O_3$.[41,42,43] In this context, the earlier onset of densification in CoO•$3Al_2O_3$ when com-pared to MgO•$3Al_2O_3$ may be explained by the lower octahedral site preference of Co, allowing for a greater number of lattice sites to participate in diffusion.

This process is enhanced by a relatively higher concentration of cation vacancies in these Al_2O_3 rich materials when compared to their stoichiometric counterparts. Dilatometry shows the formation of the $NiAl_{10}O_{16}$ phase appears to retard densification

onset but leads to significant densification during exsolution in contrast to the other two systems.

Diffusion of cations during exsolution eventually leads to regions rich in the divalent cations, promoting nucleation of α-Al_2O_3. The $NiO \cdot 3Al_2O_3$ material densifies approximately 33% TD compared to the initial 20% TD densification for $CoO \cdot 3Al_2O_3$ and $MgO \cdot 3Al_2O_3$ materials which is accompanied by the appearance of α-Al_2O3 in the XRD studies. We attribute the defect-rich intermediate $NiAl_{10}O_{16}$ phase to the anomalous sintering behavior that allows for rapid diffusion in the first densification regime beyond the point at which we observe nucleation of α-Al_2O_3.

The sharp reduction in densification rate in the second regime for each of the $MO \cdot 3Al_2O_3$ materials can be interpreted as a shift in the densification rate limiting species from cations to oxygen anions, the rate limiting species in α-Al_2O_3. Once the $MO \cdot 3Al_2O_3$ materials precipitate MAl_2O_4 and α-Al_2O_3, diffusional processes are dominated by oxygen mobility and the rate of densification is slowed.

To clarify, each $MO \cdot 3Al_2O_3$ shows a similar initial densification regime not seen in the corresponding phase pure spinels. For the $MgO \cdot 3Al_2O_3$ and $CoO \cdot 3Al_2O_3$ systems, this densification regime happens prior to exsolution of α-Al_2O_3. For $NiO \cdot 3Al_2O_3$, an intermediate $NiAl_{10}O_{16}$ phase forms, and the initial densification regime is concomitant with α-Al_2O_3 exsolution. The cause of the initial densification regime is not immediately clear, and may arise due to a number of factors. The first being the high number of cation vacancies necessarily present in the Al_2O_3 rich spinel. In addition, the highly kinetic LF-FSP synthesis process may introduce further defects that drive this densification process. The kinetic nature of the synthesis process may also provide spinels with inversion levels

different than the thermodynamically favored inversion level. The rearrangement of cations to the thermodynamically favored inversion level may facilitate densification.

6.4   Conclusions

Al_2O_3 rich MAl_2O_3 [M = Ni, Co, Mg] single-phase nanopowders were produced by LF-FSP at the composition of $MO \cdot 3Al_2O_3$. Upon heating, the powders phase separate to α-Al_2O_3 and MAl_2O_3. Compacts of the $MO \cdot 3Al_2O_3$ powders were produced that resulted in dense α-Al_2O_3/MAl_2O_4 composites after sintering. Compacts of the same composition were prepared by ball-milling MAl_2O_4 and Al_2O_3 nanopowders. Despite the difference in initial length scales of compositional mixing, both routes produce microstructures with average grain sizes that are not statistically different.

Through a combined dilatometry and XRD study, we establish that in the Mg and Co systems, densification occurs prior to nucleation of α-Al_2O_3 from the solid solution phase. We attribute the initial densification to cation rearrangement in the solid solution. Once α-Al_2O_3 is nucleated, densification is slowed. In the $NiO \cdot 3Al_2O_3$ system, the solid solution transforms to a metastable $NiAl_{10}O_{16}$ phase. The $NiAl_{10}O_{16}$ phase then densifies while retarding the nucleation of α-Al_2O_3.

In the Mg and Co systems, an initial densification region is present by dilatometry that does not appear in the stoichiometric spinel dilatometry. We attribute this densification region to a combination of rearrangement of the cations in the highly disordered Al_2O_3 rich spinel lattice and the corresponding density increase upon transformation to α-Al_2O_3. In the Ni system, this densification regime is delayed until the intermediate $NiAl_{10}O_{16}$ phase transforms to α-Al_2O_3.

References

[1] C. Otero Are_an, M. Pe~narroya Mentruit, A. J. Lopez Lopez, and J. B. Parra, "High Surface Area Nickel Aluminate Spinels Prepared by a Sol-Gel Method," *Colloids Surf. A Physicochem. Eng. Asp.*, **180**, 253–8 (2001).

[2] J. R. H. Ross, M. C. F. Steel, and A. Zeini-Isfahani, "Evidence for the Participation of Nickel Aluminate Sites in Steam Reforming of Methane over Nickel/Alumina Catalysts," *J. Catal.*, **52**, 280–90 (1978).

[3] Z. Chen, E. Shi, W. Li, Y. Zheng, and W. Zhong, "Hydrothermal Synthesis and Optical Property of Nano-Sized $CoAl_2O_4$ Pigment," Mater. Lett., **55**, 281–4 (2002).

[4] W.-S. Cho and M. Kakihana, "Crystallization of Ceramic Pigment $CoAl_2O_4$ Nanocrystals from Co-Al Metal Organic Precursor," *J. Alloys Compd.*, **287** [1–2] 87–90 (1999).

[5] A. Sirijaruphan, A. Horv_ath, J. G. GoodwinJr, and R. Oukaci, "Cobalt Aluminate Formation in Alumina-Supported Cobalt Catalysts: Effects of Cobalt Reduction State and Water Vapor," *Catal. Lett.*, **91** [1–2] 89–94 (2003).

[6] S. Rojanapipatkul and B. Jongsomjit, "Synthesis of Cobalt on Cobalt-Aluminate Via Solvothermal Method and its Catalytic Properties for Carbon Monoxide Hydrogenation," *Catal. Commun.*, **10**, 232–6 (2008).

[7] D. P. Jiang, Y. Q. Zou, L. B. Su, H. L. Tang, F. Wu, L. H. Zheng, H. J. Li, and J. Xu, "A Co^{2+}-Doped $Mg_{0.4}Al_{2.4}O_4$ Spinel Crystal as Saturable Absorber for a LD Pumped Er: Glass Microchip Laser at 1535 nm," *Laser Phys. Lett.*, **8**, 343–8 (2011).

[8] C. Wang and Z. Zhao, "Transparent $MgAl_2O_4$ Ceramic Produced by Spark-Plasma Sintering," *Scripta Mater.*, **61** [2] 193–6 (2009).

[9] L. Dussault, J. C. Dupin, C. Guimon, M. Monthioux, N. Latorre, T. Ubieto, E. Romero, C. Royo, and A. Monzon, "Development of Ni-Cu-Mg-Al Catalysts for the Synthesis of Carbon Nanofibers by Catalytic Decomposition of Methane," *J. Catal.*, **251**, 223–32 (2007).

[10] I. E. Achouri, N. Abatzoglou, C. Fauteux-Lefebvre, and N. Braidy, "Diesel Steam Reforming: Comparison of Two Nickel Aluminate Catalysts Prepared by Wet-Impregnation and Co-Precipitation," *Catal. Today*, **207**, 13–20 (2013).

[11] N. Bayal and P. Jeevanandam, "Synthesis of Metal Aluminate Nanoparticles by Sol-Gel Method and Studies on their Reactivity," *J. Alloy. Compd.*, **516**, 27–32 (2012).

[12] T. R. Hinklin, J. Azurdia, M. Kim, J. C. Marchal, S. Kumar, and R. M. Laine, "Finding Spinel in all the Wrong Places," *Adv. Mater.*, **20**, 1373–5 (2008).

[13] W. H. Bragg, "The Structure of the Spinel Group of Crystals," *Philos. Mag.*, **30** [176] 305–15 (1915).

[14] S. Nishikawa, "Structure of Some Crystals of the Spinel Group," *Proc. Math. Phys. Soc. Tokyo*, **8**, 199–209 (1915).

[15] K. E. Sickafus, J. M. Wills, and N. W. Grimes, "Spinel Compounds: Structure and Property Relations," *J. Am. Ceram. Soc.*, **82** [12] 3279–92 (1999).

[16] D. S. McClure, "The Distribution of Transition Metal Cations in Spinels," *J. Phys. Chem. Solids*, **3**, 311–7 (1957).

[17] J. K. Burdett, G. D. Price, and S. L. Price, "Role of the Crystal-Field Theory in Determining Structure of Spinels," *J. Am. Chem. Soc.*, **104**, 92–5 (1982).

[18] R. E. Carter, "Mechanism of Solid-State Reaction Between Magnesium Oxide and Aluminum Oxide and Between Magnesium Oxide and Ferric Oxide," *J. Am. Ceram. Soc.*, **44** [3] 116–20 (1961).

[19] P. H. Bolt, F. H. P. M. Habraken, and J. W. Geus, "Formation of Nickel, Cobalt, Copper, and Iron Aluminates From a- and c-Alumina-Supported Oxides: A Comparative Study," *J. Solid State Chem.*, **135**, 59–69 (1998).

[20] J. M. Fernandez Colinas and C. Otero Arean, "Kinetics of Solid-State Spinel Formation: Effect of Cation Coordination Preference," J. Solid State Chem., 109, 43–6 (1994).

[21] T. Hinklin, B. Toury, C. Gervais, F. Babonneau, J. J. Gislason, R. W. Morton, and R. M. Laine, "Liquid-Feed Flame Spray Pyrolysis of Metalloorganic and Inorganic Alumina Sources in the Production of Nanoalumina Powders," Chem. Mater., 16 [1] 21–30 (2003).

[22] C. R. Bickmore, K. F. Waldner, D. R. Treadwell, and R. M. Laine, "Ultrafine Spinel Powders by Flame Spray Pyrolysis of a Magnesium Aluminum Double Alkoxide," *J. Am. Ceram. Soc.*, **79** [5] 1419–23 (1996).

[23] R. M. Laine, R. Baranwal, T. Hinklin, D. Treadwell, A. Sutorik, C. Bickmore, K. Waldner, and S. S. Neo, "Making Nanosized Oxide Powders from Precursors by Flame Spray Pyrolysis"; pp. 17–24 in Novel Synthetic and Processing Routes to Ceramics. Key Engineering Materials, Vols 159–160, Edited by K. Uematsu and H. Otsuka. Trans Tech Publ. Ltd., Du¨ rten, Switzerland, 1998.

[24] J. A. Azurdia, J. Marchal, P. Shea, H. Sun, X. Q. Pan, and R. M. Laine, "Liquid-Feed Flame Spray Pyrolysis as a Method of Producing Mixed-Metal Oxide Nanopowders of Potential Interest as Catalytic Materials. Nanopowders Along the NiO-Al_2O_3 Tie Line Including $(NiO)_{0.22}(Al_2O_3)_{0.78}$, a New Inverse Spinel Composition," *Chem. Mater.*, **18**, 731–9 (2006).

[25] J. Azurdia, J. Marchal, and R. M. Laine, "Synthesis and Characterization of Mixed-Metal Oxide Nanopowders Along the CoO_x–Al_2O_3 Tie Line Using Liquid-Feed Flame Spray Pyrolysis," *J. Am. Ceram. Soc.*, **89** [9] 2749–56 (2006).

[26] T. R. Hinklin and R. M. Laine, "Synthesis of Metastable Phases in the Magnesium Spinel-Aluminum System," *Chem. Mater.*, **20**, 553–8 (2008).

[27] J. Marchal, T. John, R. Baranwal, T. Hinklin, and R. M. Laine, "Yttrium Aluminum Garnet Nanopowders Produced by Liquid-Feed Flame Spray Pyrolysis (LF-FSP) of Metalloorganic Precursors," *Chem. Mater.*, **16**, 822–31 (2004).

[28] R. Baranwal, M. P. Villar, R. Garcia, and R. M. Laine, "Synthesis, Characterization, and Sintering Behavior of Nano-Mullite Powder and Powder Compacts," J. Am. Ceram. Soc., 84 [5] 951–61 (2001).

[29] I. Levin and D. Brandon, "Metastable Alumina Polymorphs: Crystal Structures and Transition Sequences," *J. Am. Ceram. Soc.*, **81** [8] 1995–2012 (1998).

[30] C. M. Lieber, "Nanoscale Science and Technology: Building a Big Future from Small Things," *MRS Bull.*, **28** [7] 486–91 (2003).

[31] B. C. Lippens and J. H. De Boer, "Study of Phase Transformation During Calcination of Aluminum Hydroxides by Selected Area Electron Diffraction," *Acta Cryst.*, **17**, 1312–21 (1964).

[32] T. Hahn (Ed.), *International Tables of Crystallography*, Vol. A. Kluwer, London, UK. 1995.

[33] J. A. Ball, M. Pirzada, R. W. Grimes, M. O. Zacate, D. W. Price, and B.P. Uberuaga, "Predicting Lattice Parameter as a Function of Cation Disorder in $MgAl_2O_4$ Spinel*," J. Phys.: Condens. Matter*, **17**, 7621–31 (2005).

[34] A. Krell, K. Waetzig, and J. Klimke, "Influence of the Structure of $MgO\_nAl_2O_3$ Spinel Lattices on Transparent Ceramics Processing and Properties," *J. Eur. Ceram. Soc.*, **32**, 2887–98 (2012).

[35] P. Bassoul and J. C. Gilles, "Structure and Microstructure of the Metastable B Phase ($NiAl_{10}O_{16}$): I. Preparation and Structural Study by X-ray Diffraction," *J. Solid State Chem.*, **58**, 383–8 (1985).

[36] P. Bassoul and J. C. Gilles, "Structure and Microstructure of the Metastable B Phase ($NiAl_{10}O_{16}$): II. An Electron Microscopic Investigation of the Microstructure," *J. Solid State Chem.*, **58**, 389–97 (1985).

[37] R. J. Bratton, "Initial Sintering Kinetics of $MgAl_2O_4$," *J. Am. Ceram. Soc.*, **52** [8] 417–9 (1969).

[38] M. Rubat du Merac, H.-J. Kleebe, M. M. M€uller, and I. E. Reimanis, "Fifty Years of Research and Development Coming to Fruition; Unraveling the Complex Interactions During Processing of Transparent Magnesium Aluminate ($MgAl_2O_4$) Spinel," *J. Amer. Ceram. Soc.*, **96** [11] 3341–65 (2013).

[39] Y. M. Chiang and W. D. Kingery, "Grain-Boundary Migration in Nonstoichiometric Solid Solutions of Magnesium Aluminate Spinel: II, Effects of Grain-Boundary Nonstoichiometry," *J. Am. Ceram. Soc.*, **73** [5] 1153–8 (1990).

[40] S. T. Murphy, C. A. Gilbert, R. Smith, T. E. Mitchell, and R. W. Grimes, "Non-Stoichiometry in $MgAl_2O_4$ Spinel," *Phil. Mag.*, **90**, 1297–305 (2010).

[41] J. A. Ball, S. T. Murphy, R. W. Grimes, D. Bacorisen, R. Smith, B. P. Uberuaga, and K. E. Sickafus, "Defect Processes in $MgAl_2O_4$ Spinel," *Solid State Sci.*, **10**, 717–24 (2008).

[42] Mocala and A. Navrotsky, "Structural and Thermodynamic Variation in Nickel Aluminate Spinel," *J. Am. Ceram. Soc.*, **72** [5] 826–32 (1989).

[43] K. I. Lilova, A. Navrotsky, B. C. Melot, and R. Seshadri, "Thermodynamics of $CoAl_2O_4$–$CoGa_2O_4$ Solid Solutions," *J. Solid State Chem.*, **183**, 1266–71 (2010).

Chapter 7

LF-FSP particle formation studies

7.1 Introduction

Two decades of research have shown that LF-FSP is a robust technology that allows access to some of the highest quality mixed-metal oxide nanopowders as compared to solution based methods.[1,2,3,4] However, as previous chapters show, nanopowder quality is not the most important factor in developing dense, fine-grained ceramic monoliths. Few examples exist where final grain sizes are not dramatically larger than the starting materials despite decades of research on "ultrafine" or "nano" powder.[5,6] Alternately there is value in producing nanopowders by LF-FSP that can be used in the as-produced state, such as catalysts. As previously reported, LF-FSP can produce particles with novel morphologies and catalytic properties.[7,8,9] To this end, we endeavored to more fully understand the fundamental processes of particle nucleation and growth in LF-FSP, as well as develop composite nanopowders.

The main goal of work reported in this chapter was to map LF-FSP parameters and track how they affect the as-produced nanoparticles. One important factor in flame spray pyrolysis is the flame temperature. Flame temperature is a function of the heat of the combustion of the fuel, but is also dependent on the equivalence ratio, Φ. Equation **3** describes Φ. For $\Phi > 1$, the flame conditions are fuel rich, and $\Phi < 1$ describes fuel lean combustion conditions. An equivalence ratio $\Phi = 1$ indicates stoichiometric combustion.

Along with mapping the effects of different alcohol fuels on the as-produced nanoparticle properties, molecular dynamics (MD) computational methods were developed to give insight into the relatively unexplored particle formation processes inherent to LF-FSP processing.

Equation 3. Equivalence ratio for combustion.

$$\Phi = \frac{n_{fuel}/n_{ox}}{\left(n_{fuel}/n_{ox}\right)_{st}}$$

Previous LF-FSP work has shown that certain oxide combinations form core-shell particles in a single step, for example ZrO_2-Al_2O_3 and CeO_2-Al_2O_3.[9,10] The formation of core-shell particles is attributed to large differences in the vapor pressure between the two intermediate oxide species; the oxide with the lowest vapor pressure would first nucleate from the gas phase, followed by a shell of the higher vapor pressure material.[10] Given this set of conditions, we identified immiscible binary systems to investigate core-shell particle formation. The two systems reported here are WO_3-TiO_2 and CuO-TiO_2. Both systems are immiscible, but WO_3 has a significant vapor pressure at LF-FSP flame temperatures. If the particle morphology is not core-shell, it likely is a nanocomposite nanoparticle, similar to the Al_2O_3-$YAlO_3$-YSZ particles described in Chapter 5.

TiO_2 is the basis for a number of photocatalysts, although the band gap (3.2 eV anatase) limits absorption to the UV range.[11] WO_3 has a band gap in the 400-700 nm visible light range (2.8 eV), but has a conduction band (CB) below that of the H_2 reduction potential (0V NHE), limiting its use as a photocatalyst.[11] In addition, WO_3 readily degrades in neutral or basic conditions.[12] Riboni et al. produced 3 mol% WO_3-TiO_2 that showed 31% acetaldehyde reduction after 2 h, compared to 18% for pure TiO_2 under 320 nm

irradiation.[13] Reyes-Gil and Robinson found a five-fold increase in methanol degredation under AM 1.5 illumination by a WO_3-TiO_2 composite nanotube photocatalysts compared to pure TiO_2 nanotubes.[14] Akurati et al. found 3.5 mol% WO_3 coated TiO_2 degraded 95% methylene blue in 15 minutes under UV irradiation while pure TiO_2 only degraded 85% of methylene blue.[15] Lalitha et al showed 160 mmol H_2 production over 10 h on 5 mol% CuO loaded TiO_2 under visible light, while TiO_2 showed no hydrogen evolution.[16] Jin et al. found a 5.1% quantum efficiency for H2 production on a dye sensitized 1.0 wt% CuO-TiO_2 catalyst under visible light irradiation.[17] Bandara et al. found up to 20 ml/h H_2 production from 7 mol% CuO-TiO_2 composite photocatalysts under UV irradiation where pure TiO_2 produced 0.625 ml/h.[18] The possibility of reduction to Cu_2O-TiO_2 particles provides access to another type of particle with considerable interest in the literature.[16] The materials described in this chapter were not tested for photocatalytic activity, but testing should be performed in the future.

7.2   Experimental

7.2.1   Particle formation studies

Alumatrane, $N[(CH_2CH_2O)_3]Al$ was used as a precursor to Al_2O_3. Yttrium propionate, $(CH_3CH_2COO)_3Y$, was used as a precursor to Y_2O_3. Synthesis of these precursors is further described in Chapter 2. Titanatrane, $N[(CH_2CH_2O)_3]Ti(Oi\text{-}Pr)$ (MP Biomedicals, Santa Ana, CA), was used as a precursor to TiO_2 and was used as received. All particle formation studies were conducted at 1.0 wt% ceramic loading in solution fed at 106 mL/min into the nozzle. The nozzle O_2 flow rate was 3.5 mol/min and the shield O_2 was 11.9 mol/min at 80 psi. Flame temperatures were measured by an A11C S-type thermocouple (Nanmac Inc.,

Holliston, MA) inserted directly into the flame. Flame measurements were also measured by an OS3750 optical pyrometer (Omega Engineering, Inc., Stamford, CT).

For core-shell particle studies, titanatrane was used as a precursor to TiO_2. Tungsten glycolate, $(OCH_2CH_2O)_3W$ and tungsten lactate, $(CH_3CH(OH)COO)_2WO_2$, were used as precursors to WO_3.[19] Tungsten glycolate was prepared by reaction ammonium metatungstate, $(NH_4)_6H_2W_{12}O_{40} \cdot xH_2O$, (Sigma-Aldrich, St. Louis, MO) with ethylene glycol (Sigma-Aldrich, St. Louis, MO).

Ammonium metatungstate (50 g, 17 mmol) was added to 250 mL (4.48 mol) of ethylene glycol and heated to 160° C for 3 h. The colorless solution turned from pale yellow to deep blue over the course of the reaction. The solution returned to yellow after several days aging. Tungsten glycolate had a ceramic yield of 11.8% in excess ethylene glycol and was not further isolated before using as a precursor.

Tungsten lactate was prepared by the reaction of ammonium metatungstate with lactic acid at 120° C. Ammonium metatungstate (50 g, 17.0 mmol) was added to 250 mL (3.36 mol) DL-lactic acid and heated to 120°C for 3 h. The as-produced tungsten lactate had a ceramic yield of 12.4% with excess lactic acid present. The deep blue solution was used as-produced.

Copper acetate (Sigma-Aldrich, St. Louis, MO), $(CH_3COO)_2Cu \cdot 1H_2O$ was used as-received as a precursor to CuO. Copper acetate had an experimentally observed ceramic yield of 38.2% by TGA, where copper acetate monohydrate has a theoretical ceramic yield of 39.8%.

Densities were calculated using phase fractions from Rietveld refinement of XRD patterns and the following densities: Rutile 4.22 g/cm^3, Anatase 3.89 g/cm^3, monoclinic WO_3 7.30 g/cm^3, tetragonal WO_3 7.219 g/cm^3, triclinic WO_3 7.30 g/cm^3, orthorhombic WO_3 7.30 g/cm^3, tenorite CuO 6.51 g/cm^3.

CuO-TiO_2 powders were also produced using a sol-gel synthesis method. Powders were prepared by slowly dripping 10.7 g (37.6 mmol) titanium (IV) tetraisopropoxide into a stirred 500 mL DI water solution containing 0.4 g (2.0 mmol) dissolved copper acetate at room temperature. TTIP immediately reacted with the solution to produce a green precipitate. The solution was rotovapped until dry, and ground.

7.2.2   X-ray photoelectron spectroscopy (XPS)

For XPS, approximately 4 mm^2 of powder was spread into a thin (0.5 mm) layer on conductive copper tape. XPS analysis was performed on a Kratos Axis Ultra XPS using monochromated Al X-ray source at 15 kV and 10 mA. Samples were flooded with electrons during data acquisition. A pass energy of 160 eV was used for survey scans and individual peak scans used a pass energy of 20 eV. Survey spectra were collected at 240 eV/min and individual peak spectra were an average of four scans at 4 eV/min. Spectra were analyzed using CasaXPS. Spectra were calibrated used the adventitious C 1s peak at 284.6 eV.

7.3   Results and Discussion

This section begins with discussion of particle formation studies as a function of flame temperature for four different alcohols with increasing heats of combustion: methanol, ethanol, 1-propanol, and n-butanol. This effort provides a baseline to identify the factors in LF-FSP that determine particle size, phase, and morphology. Next, modeling studies are briefly discussed. Finally, the formation of composite oxide nanoparticles by LF-FSP is discussed through studies on two systems, WO_3-TiO_2 and CuO-TiO_2. These studies were undertaken in light of the nanocomposite nanoparticles we observed by TEM in Chapter 5. Composite powders are referred to in mol% WO_3 and mol% TiO_2.

7.3.1   Particle formation studies

The study of LF-FSP particle formation began with mapping of particle formation holding all variables constant. Previously it had been established that particle formation was affected by the altering LF-FSP fuels.[20] Although LF-FSP often produces kinetic phase powders, we hypothesized that flame temperature could affect phase composition.[20] Our studies used constant 1.0 wt % ceramic yield solutions in progressively longer chain alcohol solvents/fuel: methanol, ethanol, 1-propanol, and n-butanol. The 1.0 wt % ceramic yield represents a standard concentration for LF-FSP nanopowders synthesis.

7.3.1.1 Flame temperature study

To properly characterize the effects of solvent on particle size and phase composition, flame temperature profiles were created for the four alcohols used in this study. For flame temperature studies, solvent/fuel was pumped at 106 mL/min with 15.4 mol/min of O_2 at 80 psi. The oxygen mass flow rate was not varied to avoid changing process variables. Flame temperatures were measured by an S-type thermocouple inserted directly into the

flame. Direct flame temperature measurements were supported by a standard: optical pyrometer measurements of an Al_2O_3 tube placed into the flame, calibrated to the emissivity of Al_2O_3. Figure **7.1** shows the flame temperature profile for each solvent.
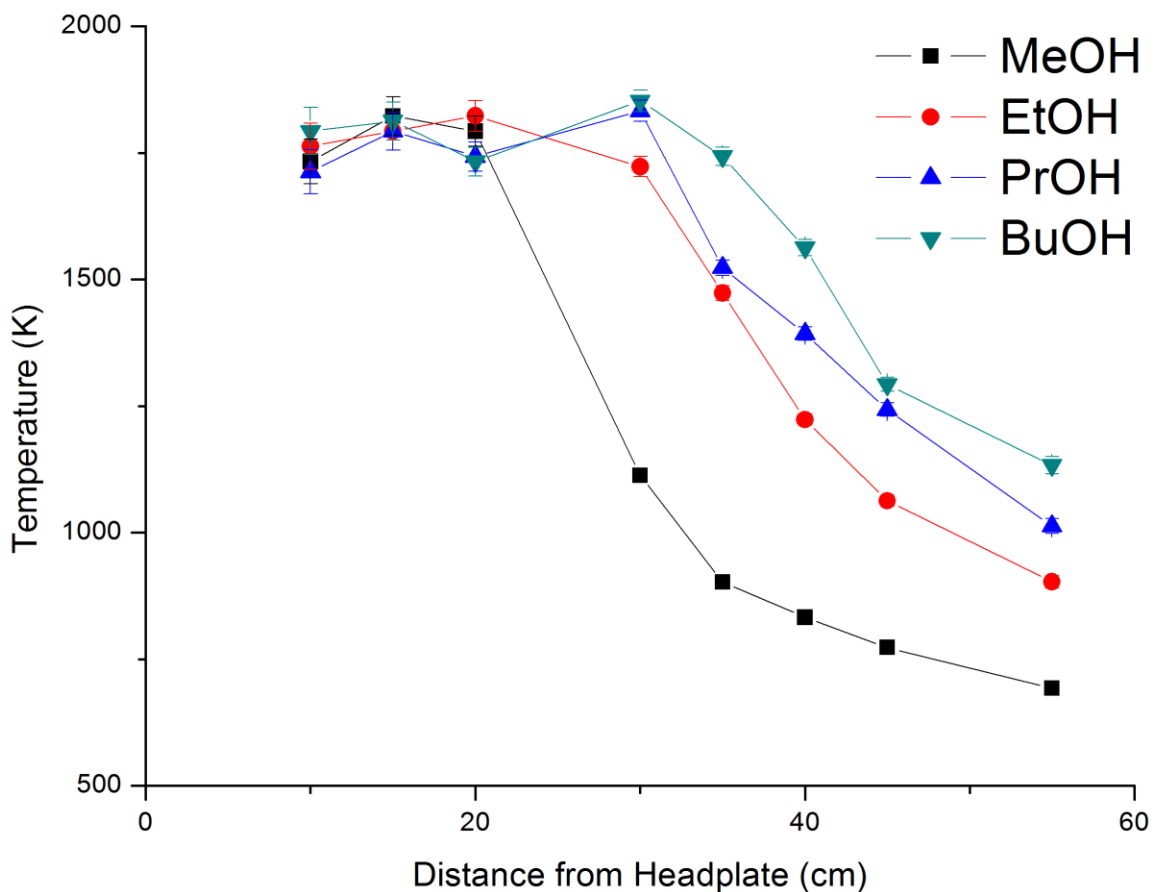
Figure 7.1. Flame temperatures for the four alcohol fuels studied.

The peak flame temperatures did not change significantly as combustion proceeded despite using longer chain alcohols with higher heats of combustion. Table **7-1** shows the standard heats of combustion ($\Delta cH°$) for the four solvents studied. Although the peak temperatures did not vary, the flame length increased as alcohol chain length increased. In LF-FSP, two sources of O_2 are available for combustion, the nozzle O_2, which is injected with the fuel and the shield O_2, which is injected around the flame. Assuming the nozzle

O_2 is the only gas involved in combustion, the flame equivalence ratio is $\Phi = 1.6$. At this equivalence ratio, typical adiabatic flame temperatures for the alcohol fuels used in this study are around 1900 K, which agrees well with peak measured flame temperatures of 1820-1850 K.[21]

Taking into account the total O_2 content, an equivalence ratio of $\Phi = 0.35$ is found. Flame temperatures are not typically characterized at such lean conditions, but at $\Phi = 0.5$, the fuels used here have adiabatic flame temperatures around 1500 K, below our experimentally measured flame temperatures. Although the shield O_2 is important in oxidizing any trace carbon soot formation, it is not likely a participant in the combustion process.

Table 7-1. Standard heats of combustion for alcohols used for particle formation studies.[22]

Fuel	$\Delta_c H°$ [kJ/mol]
MeOH	726
EtOH	1367
1-PrOH	2019
n-BuOH	2677

7.3.1.2 Particle size and phase composition as a function of flame length

Our particle size and phase composition experiments included three separate trials for each Al_2O_3, TiO_2, and Y_2O_3 data point. Phase composition was tracked by XRD of the products and average particle size was tracked by BET. Table **7-1** shows average BET surface areas for the three materials studied. All three materials show significant surface area reduction as the alcohol chain length increases, which is a consequence of higher coalescence rates due to longer residence times.

Table 7-2. BET SSAs for Al_2O_3, Y_2O_3, and TiO_2.

	Al_2O_3 [m^2/g]	Y_2O_3 [m^2/g]	TiO_2 [m^2/g]
MeOH	89±2	63±3	70±2
EtOH	67±3	53±7	58±4
1-PrOH	61±2	52±2	53±2
n-BuOH	56±5	39±7	49±2

Figure **7.2** shows the particle size as a function of flame length, derived from BET SSAs. A clear trend emerges: as flame length increases, the average particle size increases. This suggests higher particle flame residence times lead to higher coalescence rates. Table **7-3**, Table **7-4**, and Table **7-5** show phase compositions for Al_2O_3, TiO_2, and Y_2O_3, respectively. The Table **7-3** Al_2O_3 phase composition varies but is primarily δ* and δ-Al_2O_3. Note that Rietveld refinement of mixtures of transition Al_2O_3 phases is problematic, the phases are structurally similar, with different structures representing only small deviations in the location of cation vacancies.[23] Rietveld refinement is further complicated by Scherrer broadening of the peaks. Refinement improves by using an internal standard of 10 wt% LF-FSP MgO powder.
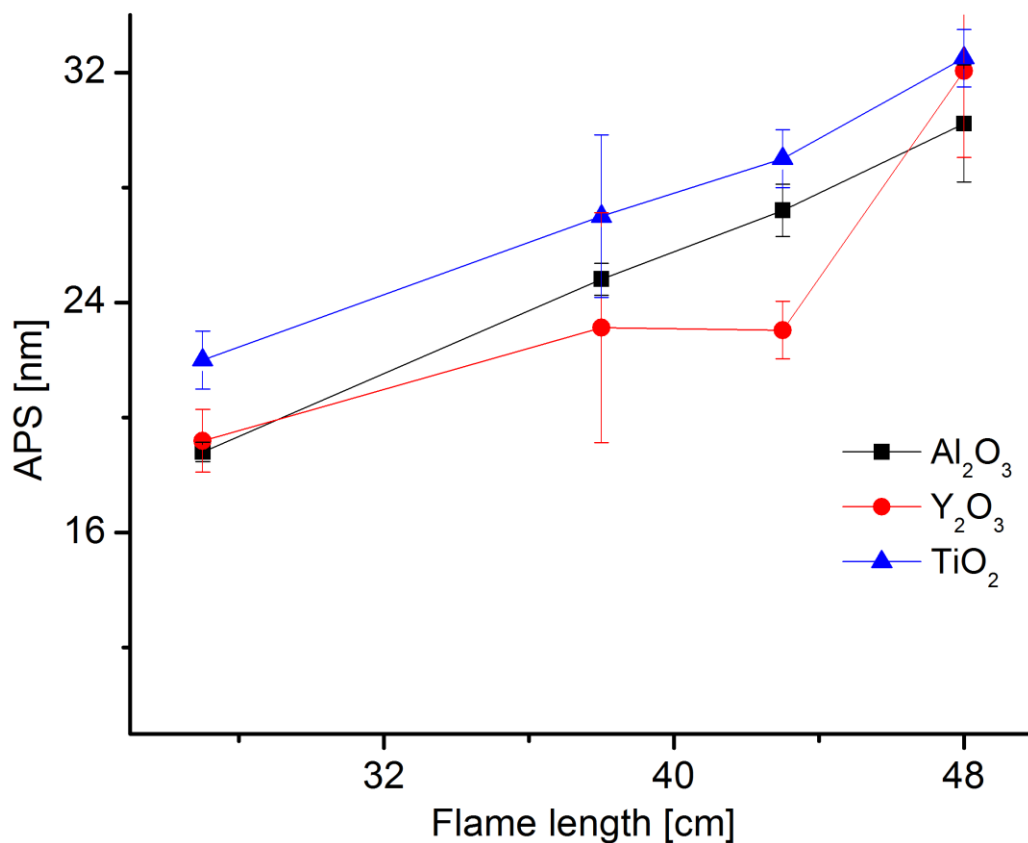
Figure 7.2. Average particle size by BET SSA as a function of flame length.

Table 7-3. XRD WPF phase composition of Al_2O_3 trial 1.

	α-alumina	θ-alumina	δ-alumina	δ*-alumina	γ-alumina	Amorphous
PDF #	10-1730	23-1009	46-1131	46-1215	50-0741	
MeOH	0	0	73.3	10.8	15.9	0
EtOH	0	0	75.6	18.2	15.9	0
PrOH	0	0	63.3	33.9	2.7	0
BuOH	0	0	65.9	27.1	6.1	0

Table **7-4** indicates that phase composition is typical of gas phase production of TiO_2. TiO_2 phase composition is constant within the error limits of Rietveld refinement. The 85:15 anatase to rutile ratio is not unexpected, even FSP of $TiCl_4$, such as the commercial Degussa P25 TiO_2 has a similar phase composition.

Table 7-4. XRD refinement for TiO_2 with standard deviation of three trials.

	Anatase	Rutile
PDF #	98-000-0081	98-000-0375
Is MeOH	85.1 (±1)	14.9 (±1)
EtOH	85.5 (±2)	14.5 (±2)
PrOH	85.8 (±1)	14.2 (±1)
BuOH	84.9 (±1)	15.1 (±1)

Table **7-5** shows the phase composition of Y_2O_3 for all three trials. The only phases present were cubic and monoclinic Y_2O_3. The monoclinic phase is often present in nanopowders and surface energy stabilized at particle sizes below 7±6 nm.[24]

Table 7-5. XRD refinement for Y_2O_3 with standard deviation of three trials.

	Cubic	Monoclinic
PDF #	01-074-7393	04-007-8278
MeOH	90.5 (±7)	9.5 (±7)
EtOH	88.7 (±8)	11.3 (±8)
PrOH	88.7 (±8)	11.3 (±8)
BuOH	89.4 (±7)	10.6 (±7)

The XRD patterns and Rietveld refinement results indicate that the particle phase compositions do not change as a function of flame residence time. Similarly, the particle phase composition does not change with increasing particle size. These results suggest the "window" in which kinetics determine the particle phase is still longer than the average particle residence time (< 100 ms), even with increasing flame length.[25] At a residence time longer than this kinetic window, we would begin to see a shift to equilibrium phases. We also find particle size does not determine particle phase composition. This again supports a kinetic phase formation conclusion, as particle size should affect particle phase.

7.3.2 Molecular dynamics results

Our original goal was to couple particle formation studies with MD simulations modeling particle nucleation and growth processes in LF-FSP. However, the combustion environment presents many issues that complicate modeling. First, the fluid dynamics of the flame are uncharacterized and present turbulent rather than laminar flames which are better understood. Second, the molecular/ionic species that form in the flame remain

unknown. Last, the time scales required for modelling of nucleation and growth are computationally intensive. In general, our computational collaborators were able to develop a number of generalized force fields that can model a number of metal oxide nanoparticle species. Force fields CuO and α-Al_2O_3 were developed that describe decreased melting point behavior of particles <5 nm.[26,27]

7.3.3   WO₃-TiO₂ particles

The first system we identified for possible core-shell particle formation was the WO_3-TiO_2 binary oxide system. WO_3 has a melting point of 1473° C and a boiling point of 1700° C, whereas TiO_2 has a melting point of 1843° C and a boiling point of 2972° C. In addition, the Figure **7.3** phase diagram shows the oxides are immiscible. From previous core-shell results, we would expect TiO_2 to nucleate first from the gas phase to form a core that is later coated by a WO_3 shell.
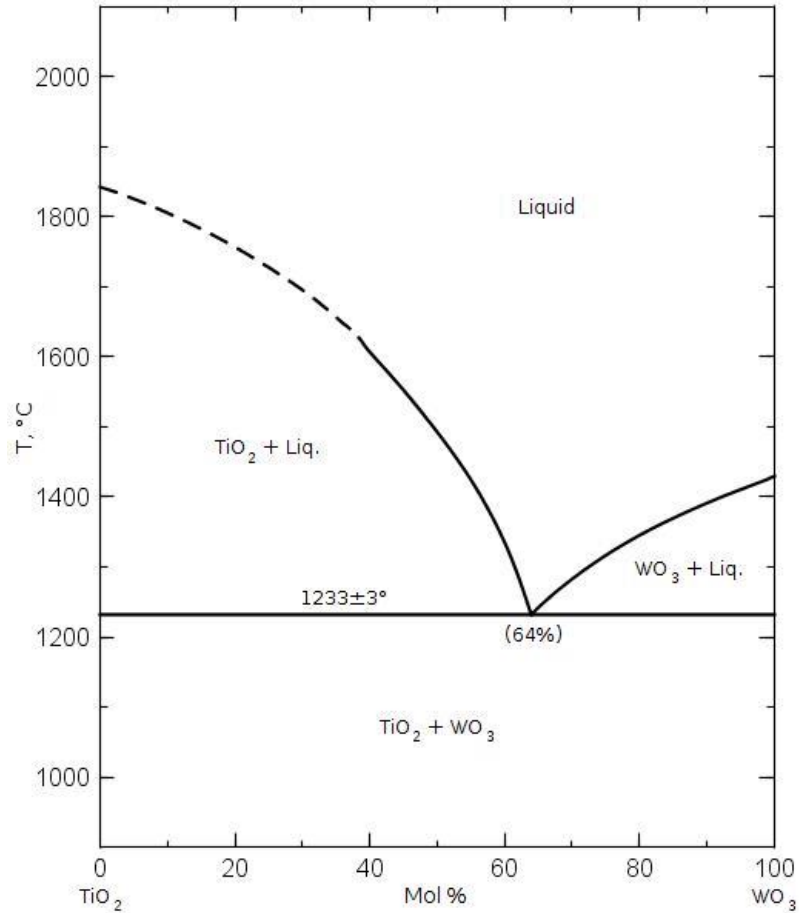
Figure 7.3. Phase diagram for the WO_3-TiO_2 system.[28]

Composite nanopowders of 1, 3, 5, 10, and 25 mol% WO_3-TiO_2 were produced by LF-FSP in addition to TiO_2 and WO_3 nanopowders. Table **7-6** shows the BET SSAs along with BET derived APSs with calculated powder densities. BET SSAs are relatively constant across all samples with an average of 56 m^2/g, but WO_3 is remarkably lower at 21 m^2/g. The low melting point of WO_3 may allow for greater particle coalescence in the flame before cooling into discrete particles.

Table 7-6. BET surface areas and APSs.

	SSA [m^2/g]	Density [g/cm^3]	APS (nm)
TiO$_2$	62	3.93	25
1 mol%	55	3.93	28
3 mol%	50	3.93	31
5 mol%	56	3.93	27
10 mol%	47	4.05	32
25 mol%	66	5.61	16
WO$_3$	21	7.28	39
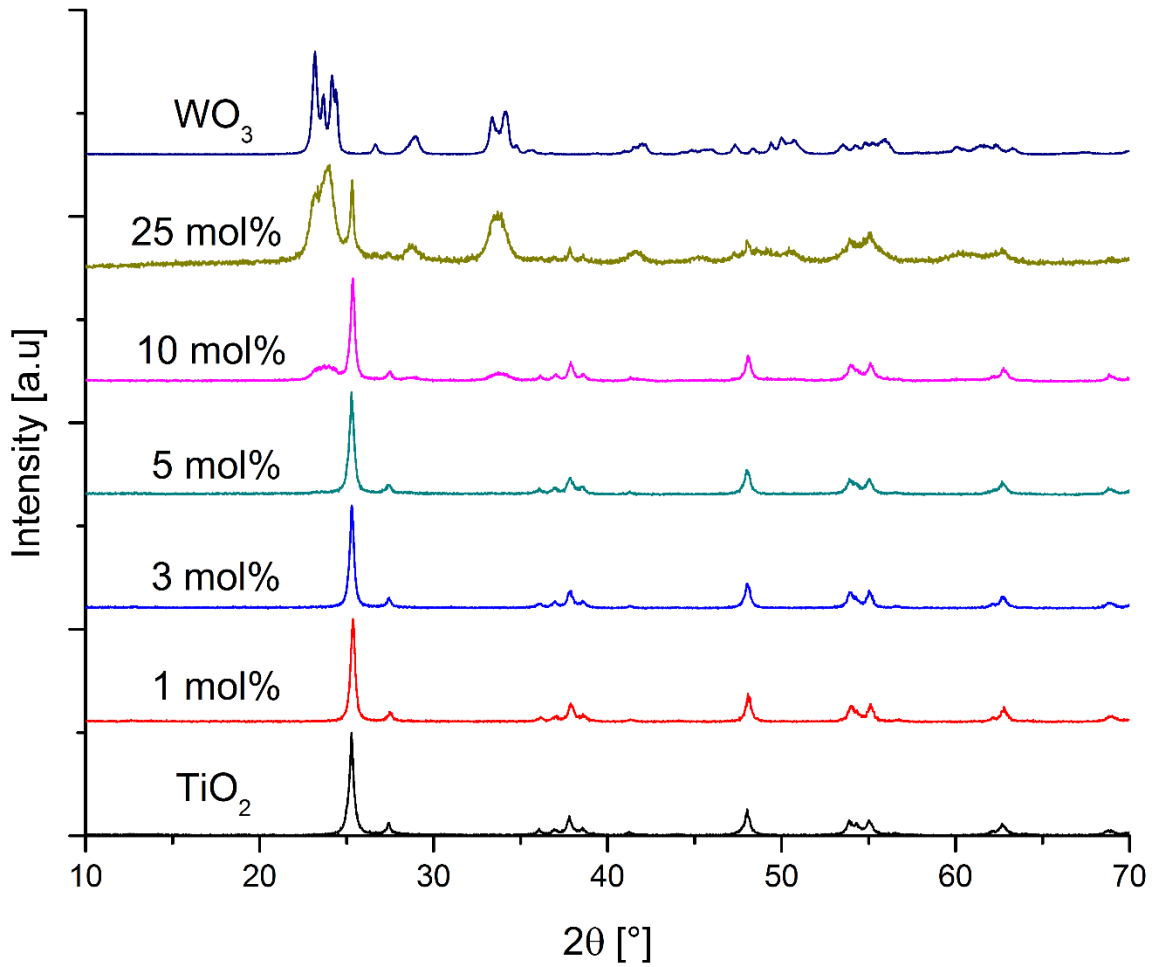
Figure 7.4. XRD patterns for TiO$_2$, 1 mol% WO$_3$-TiO$_2$, 3 mol% WO$_3$-TiO$_2$, 5 mol% WO$_3$-TiO$_2$, 10 mol% WO$_3$-TiO$_2$, 25 mol% WO$_3$-TiO$_2$, and WO$_3$.

Table **7-7** contains the phase composition of as-produced nanopowders derived from

Rietveld refinement of XRD patterns, along with Scherrer crystallite size. TiO$_2$ has a

composition of 88 wt % anatase, and 12 wt % rutile. This composition is typical of gas phase produced TiO_2, and stays constant as WO_3 is added. At 10 mol % WO_3, triclinic WO_3 is observed. At 25 mol % WO_3, triclinic, tetragonal, and orthorhombic WO_3 are observed by XRD. Pure LF-FSP WO_3 is a mixture of triclinic, monoclinic, and orthorhombic WO_3. WO_3 is tetragonal (P4/nmn) between 740-900°C, orthorhombic (Pmnb) between 330-740° C, monoclinic ($P2_1/n$) between 17-330° C, and triclinic ($P\bar{1}$) between -40-17° C.[29] Mixtures of these phases, even triclinic, are common in WO_3 nanopowders synthesized by various methods.[30, 31] Scherrer line broadening gives average crystallite sizes around 30 nm, consistent average particle sizes (APSs) in Table **7-6**.

Table 7-7. Phase compositions of as-produced nanopowders by XRD (XRD indicated crystallite size in ( ) in nm.

	Anatase	Rutile	Tetragonal WO_3	Triclinic WO_3	Monoclinic WO_3	Orthorhombic WO_3
TiO_2	88 (26)	12 (15)	--	--	--	--
1 mol%	87 (36)	13 (18)	--	--	--	--
3 mol%	87 (34)	13 (30)	--	--	--	--
5 mol%	88 (27)	12 (26)	--	--	--	--
10 mol%	81 (30)	13 (28)	--	6 (14)	--	--
25 mol%	31 (54)	4 (18)	18 (13)	25 (31)	--	22 (13)
WO_3	--	--	--	18 (50)	41 (23)	41 (32)

Visually, TiO_2 is bright white, and increasing WO_3 content gives a gradual bluish tint to the particles. This bluish tint is likely due to a reduced surface species of W^{5+}.[32] LF-FSP WO_3 exhibits a bluish tint in the lower electrostatic precipitators during collection (300° C), but oxidizes to a bright yellow on cooling to room temperature. $WO_{2.95}$ is blue, so the color change could be a consequence of slight carbothermal reduction of WO_3 by residual organics in the gas stream.[32] At lower temperatures, i.e. in the upper ESP, the powders are yellow during collection.

Figures **7.5** and **7.6** show typical nanopowder morphologies with no fraction of large particles present. Figure **7.5** shows SEM of 25 mol% WO_3-TiO_2. Figure **7.6** shows an SEM micrograph of LF-FSP WO_3. In contrast to the composite powders, which all have a spherical morphology, the WO_3 nanopowders are highly faceted. Octahedral WO_3 crystals are typical for both gas-phase and solution based synthesis methods.[33, 34]

HV	mag	WD	curr	tilt	HFW	——— 500 nm ———
15.00 kV	120 000 x	5.0 mm	0.14 nA	-0 °	2.13 μm	

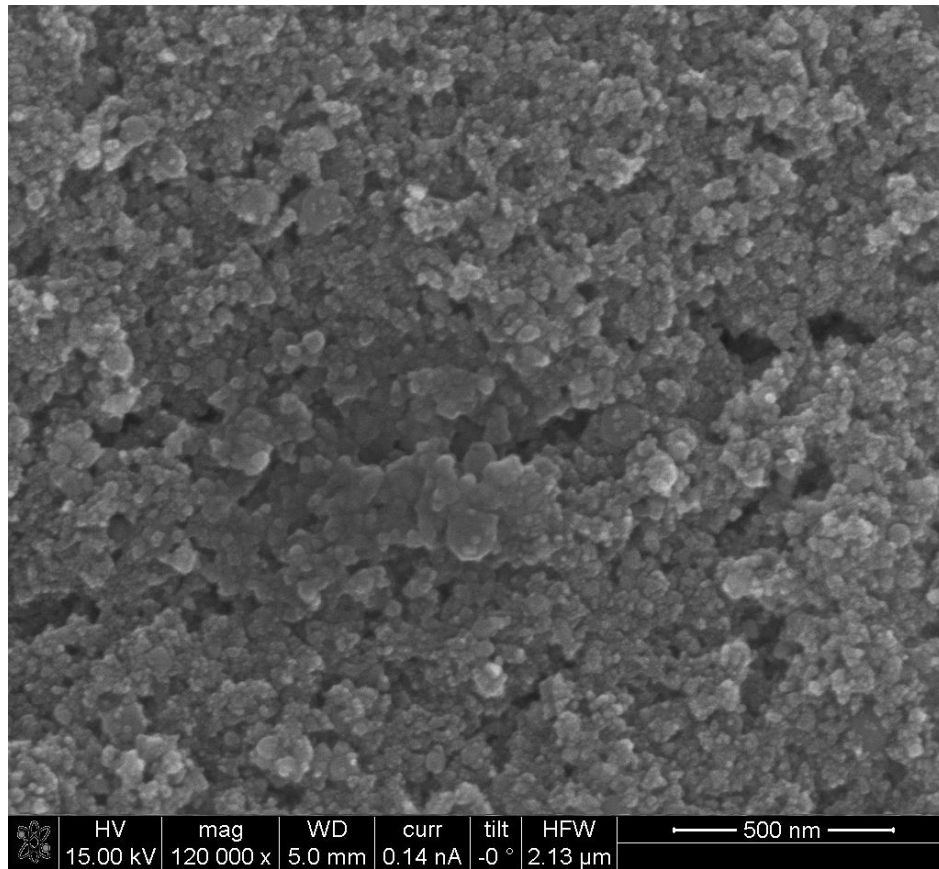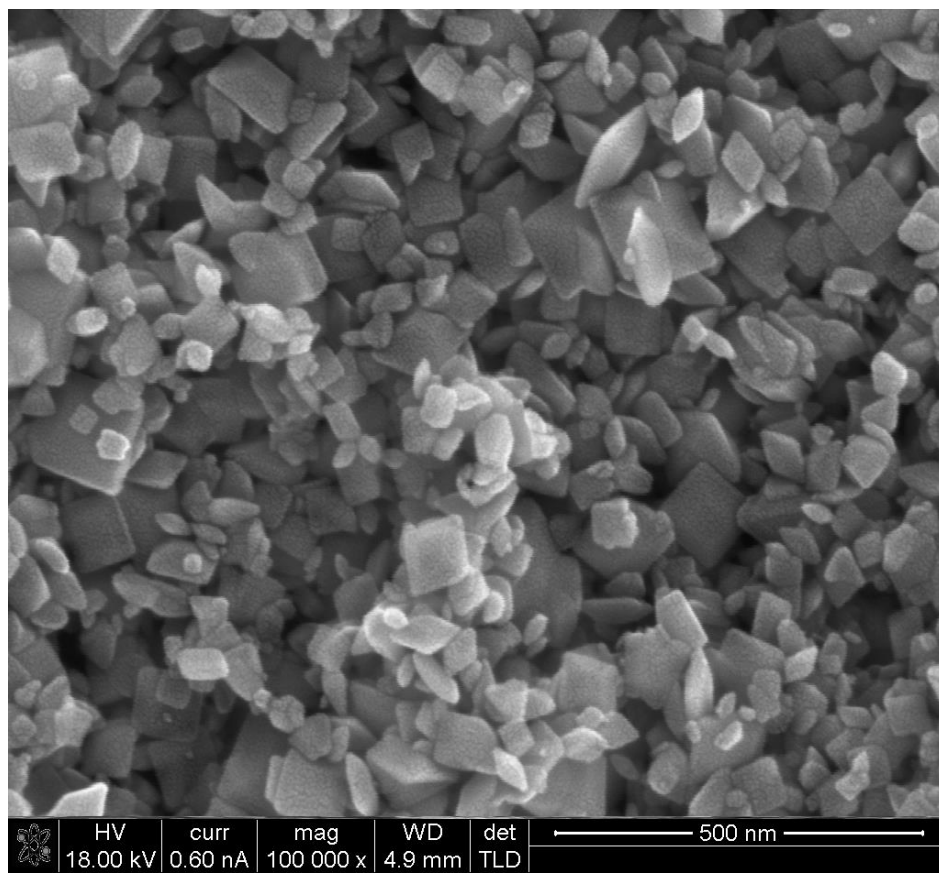**Figure 7.5**. SEM micrograph of 25 mol% WO_3-TiO_2 nanopowders.

Figure 7.6. SEM of WO$_3$ nanopowders.

TEM was used to probe individual particle morphology. Figure **7.7** shows an example

of a cluster of particles surrounded by a shell material that aggregates the particles together.
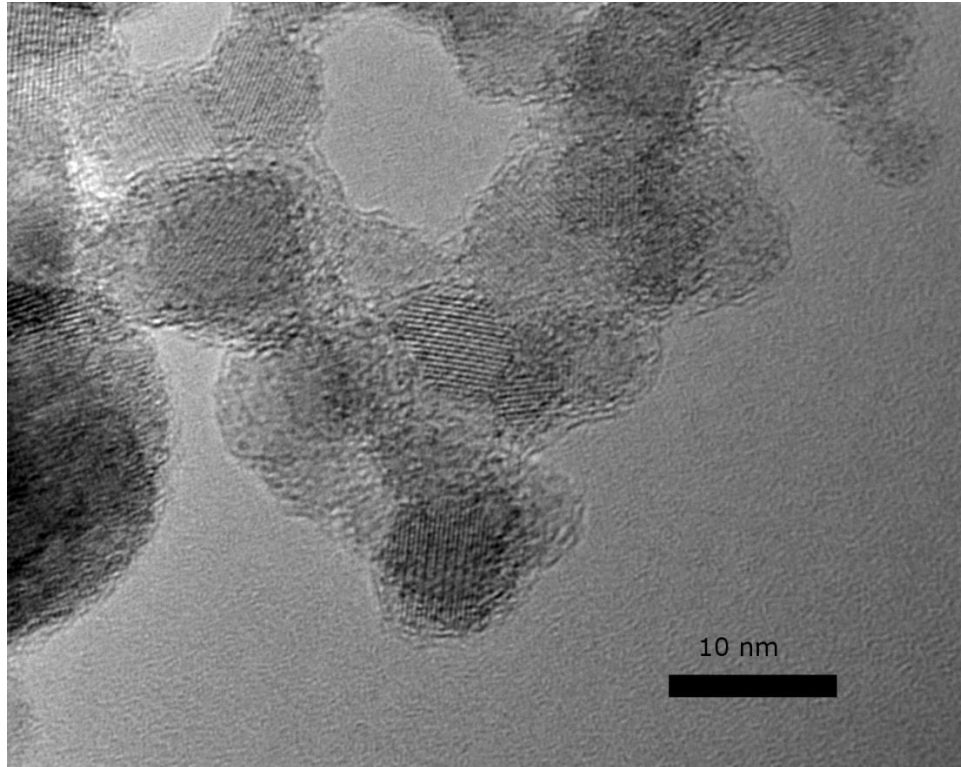
Figure 7.7. TEM micrograph of 25 mol % WO_3-TiO_2.
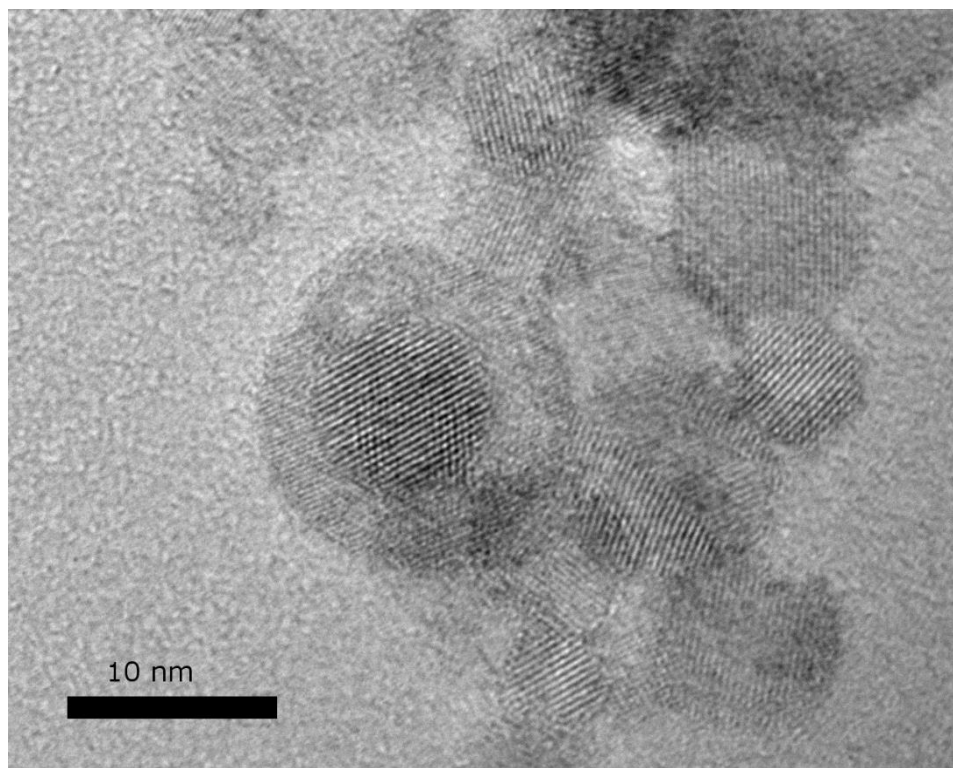
Figure 7.8. TEM micrograph 25 mol% WO_3-TiO_2.
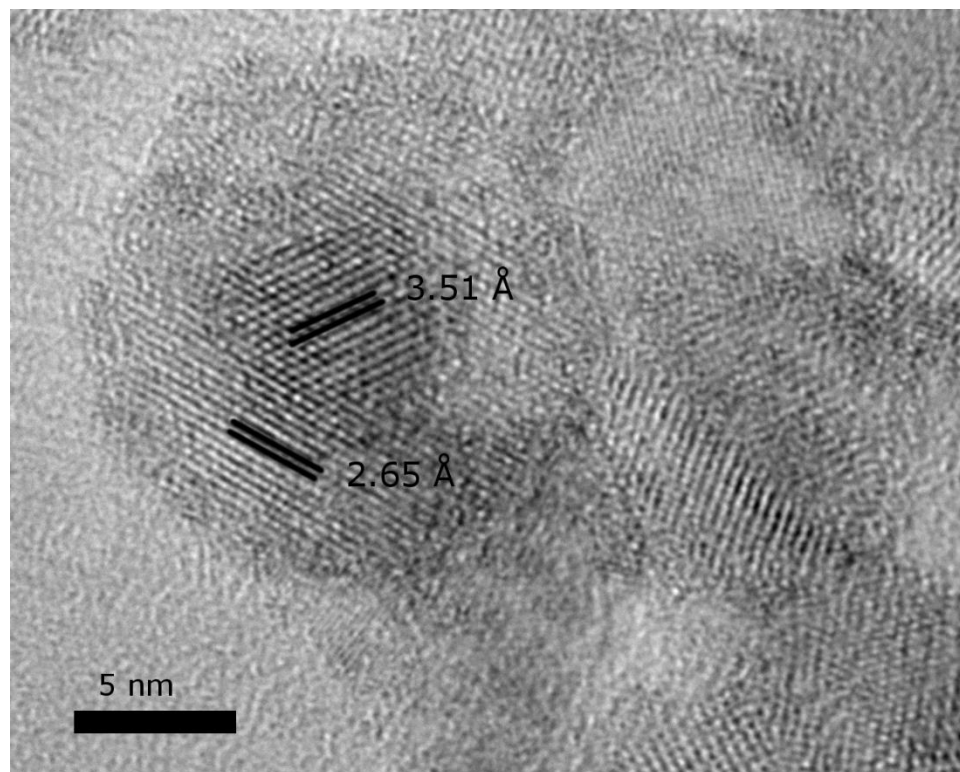
Figure 7.9. TEM micrograph of 25 mol% WO_3-TiO_2 showing core lattice spacing of 3.51 Å, (101) anatase, and shell lattice spacing of 2.65 Å, (200) tetragonal WO_3.

Figure **7.8** shows a second region of particles typical of 25 mol% WO_3-TiO_2, and Figure **7.9** shows a closer magnification of the same region. Fast Fourier transforms (FFT) of the crystalline regions show a core with a lattice spacing of 3.51 Å, consistent with that of the (101) interplanar spacing of anatase TiO_2. A FFT of the shell region gives a lattice spacing of 2.65 Å. This spacing is most consistent with that of the (200) plane of tetragonal WO_3, but is also within 0.02 Å of the (022) and (202) triclinic and (201) orthorhombic WO_3 d-spacings. This spacing is not consistent with that of any TiO_2 phase.

These TEM results strongly support our prediction that the WO_3-TiO_2 system would form core-shell particles. Whereas LF-FSP particles are typically unaggregated, the TEM suggests the TiO_2 particles physically bonded by the WO_3 shell layer.

To further validate the core-shell particle morphology, we used XPS measurements to confirm the composition. XPS is a surface sensitive technique, as photoelectrons generated deeper than a few nanometers of the surface will be inelastically scattered before being ejected. In addition, the X-ray spot size provides square microns of analysis area. XPS compositional analysis of the W 4f and Ti 2p gives the composition contained in Table **7-8**. XPS measurements have significant error, but still indicate surface enrichment of WO_3 when compared to the compositional data obtained by Rietveld refinement of XRD patterns.

Table 7-8. Compositional data for 25 mol% WO_3-TiO_2 by XRD and XPS.

	wt% WO_3	wt% TiO_2
XRD	50±2	50±2
XPS	78±20	22±20
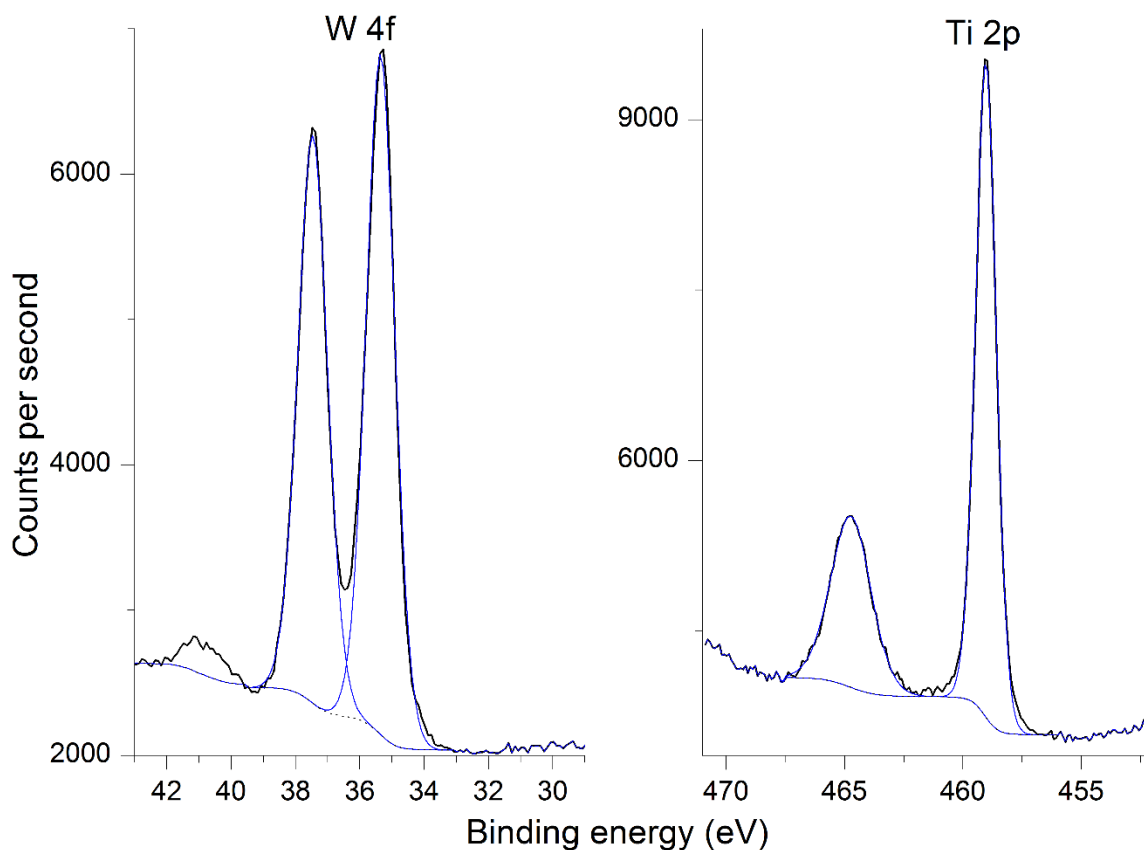
Figure 7.10. W 4f and Ti 2p XPS spectra for 25 mol% WO_3-TiO_2.

The W 4f 7/2 and 5/2 peaks are located at 35.4 and 37.5 eV, respectively, which are consistent with WO_3.[35] Although the powders appear blue, there is no evidence of W^{5+}, which would appear at a lower binding energy. The peak around 41 eV is typical of a satellite shakeup peak. The Ti 2p 3/2 and 1/2 peaks appear at 459.0 and 464.7 eV, respectively, which are typical of TiO_2.[36]

The core-shell growth process is attributed to a large difference in vapor pressure of the two oxide components. The WO_3 trimer is the most likely vapor phase species.[37] Using the Clausius-Clapeyron equation in Equation **4**, we calculate a $(WO_3)_3$ vapor pressure of 860 Pa at 1800 K, near the peak flame temperature.[37] The actual vapor pressure may be higher with water generated from ethanol combustion contributing to formation of WO_3 •

1H$_2$O, which has a higher vapor pressure than the oxide.[38] For TiO$_2$, the congruently vaporizing Ti$_3$O$_5$ phase and likely gas-phase species has a vapor pressure of 6.0E-7 Pa at 1800 K per the relation in Equation **5**.[39] This strongly supports the vapor pressure argument for core-shell formation, as vapor phase (WO$_3$)$_3$ is abundant while TiO$_2$ is expected to nucleate quickly from the gas phase.

Equation 4. Clausius-Clapeyron relation for WO$_3$ (P in atm, T in K).

$$4.56 \log P(WO_3)_3 = -\frac{90156}{T} + 40.52 \pm 0.59$$

Equation 5. Clausius-Clapeyron relation for TiO$_2$ (P in atm, T in K).

$$\log P\,(TiO_2) = -\frac{32393}{T} - 0.48\,X\,10^{-3}T + 10.51$$

Both TEM and XPS indicate that LF-FSP WO$_3$-TiO$_2$ particles form as a TiO$_2$ core with a WO$_3$ shell. We attribute this morphology to the high vapor pressure of WO$_3$ at temperatures encountered within the flame. In the next section, we examine the morphology of composite CuO-TiO$_2$ nanoparticles produced by LF-FSP.

7.3.4   CuO-TiO$_2$

Given the success of the WO$_3$-TiO$_2$ core-shell studies, we extended our approach to other possible systems. The CuO-TiO$_2$ system was attractive as the phase diagram (Figure **7.11**) did not indicate significant solubility and we had already seen success with a TiO$_2$ based system. One composite composition was produced, at 25 mol % CuO-TiO$_2$, which would provide enough surface enrichment to be easily identified.
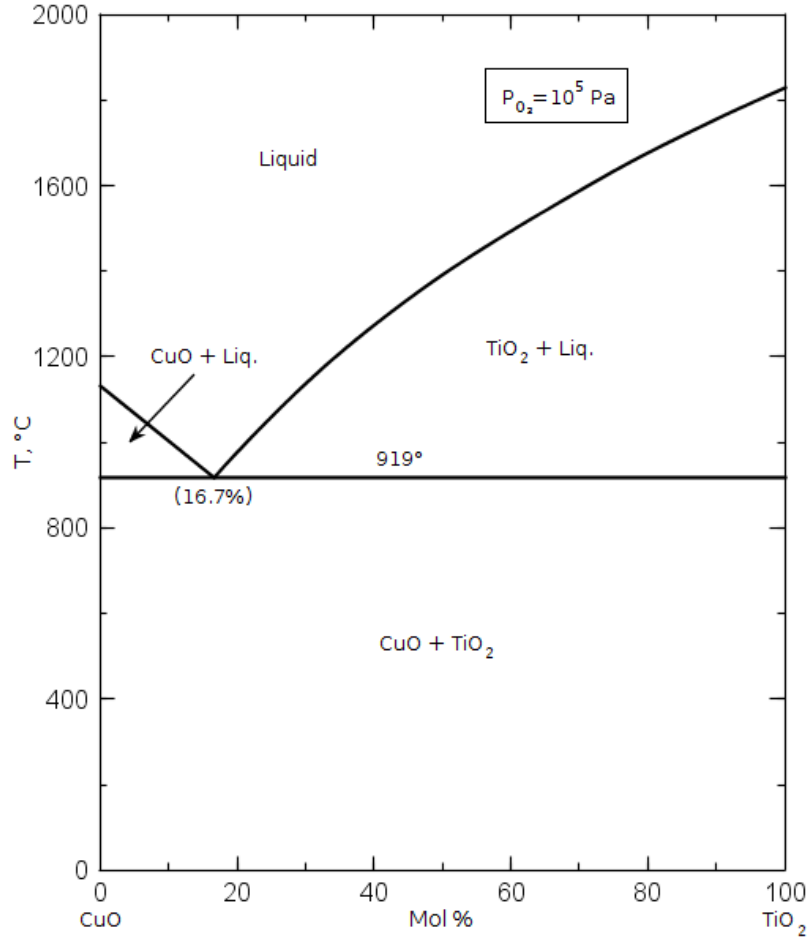
Figure 7.11. Phase diagram for the CuO-TiO₂ system.[40]

Figure **7.12** gives an SEM micrograph of as produced 25 mol% CuO-TiO₂ nanopowders. The SEM is typical of LF-FSP nanopowders. The XRD pattern for 25 mol % (25 wt %) CuO-TiO₂ is shown in Figure **7.13**. Surprisingly, the XRD pattern shows an 8:92 anatase to rutile ratio, as opposed to the typical 88:12 anatase to rutile ratio seen in TiO₂ and the WO₃-TiO₂ studies. Rietveld refinement gives a composition of 31 wt % CuO-69 wt % TiO₂.
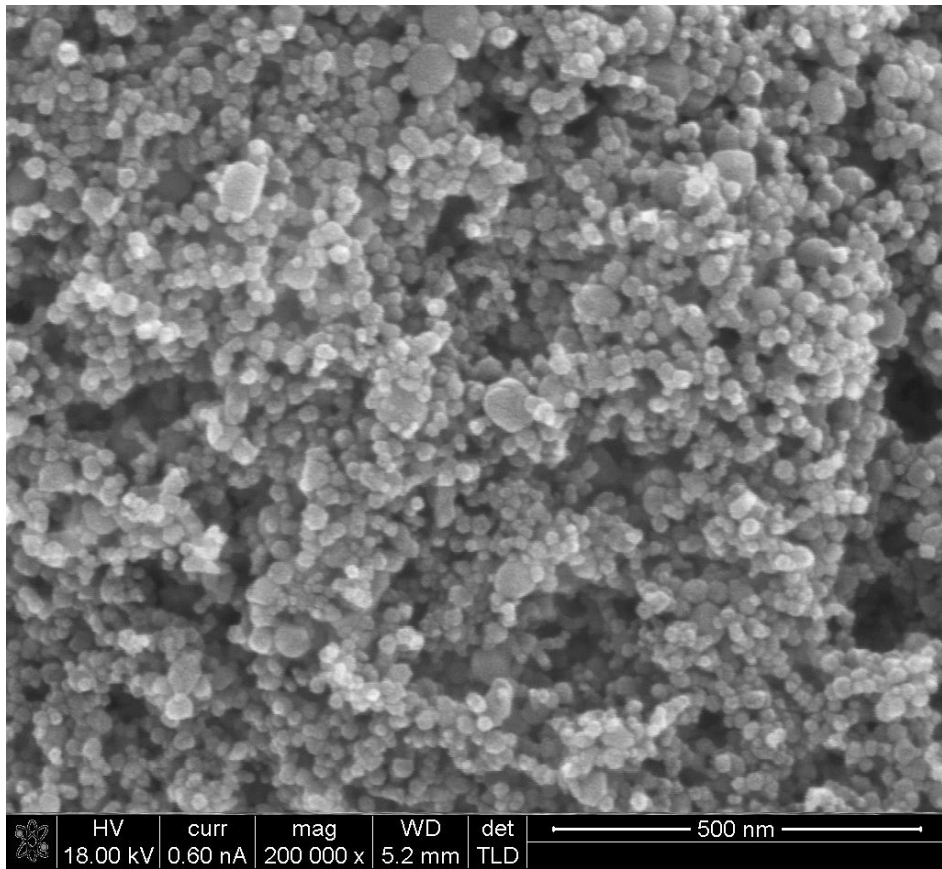
Figure 7.12. SEM micrograph of as-produced 25 mol% CuO-TiO$_2$ LF-FSP nanopowder.
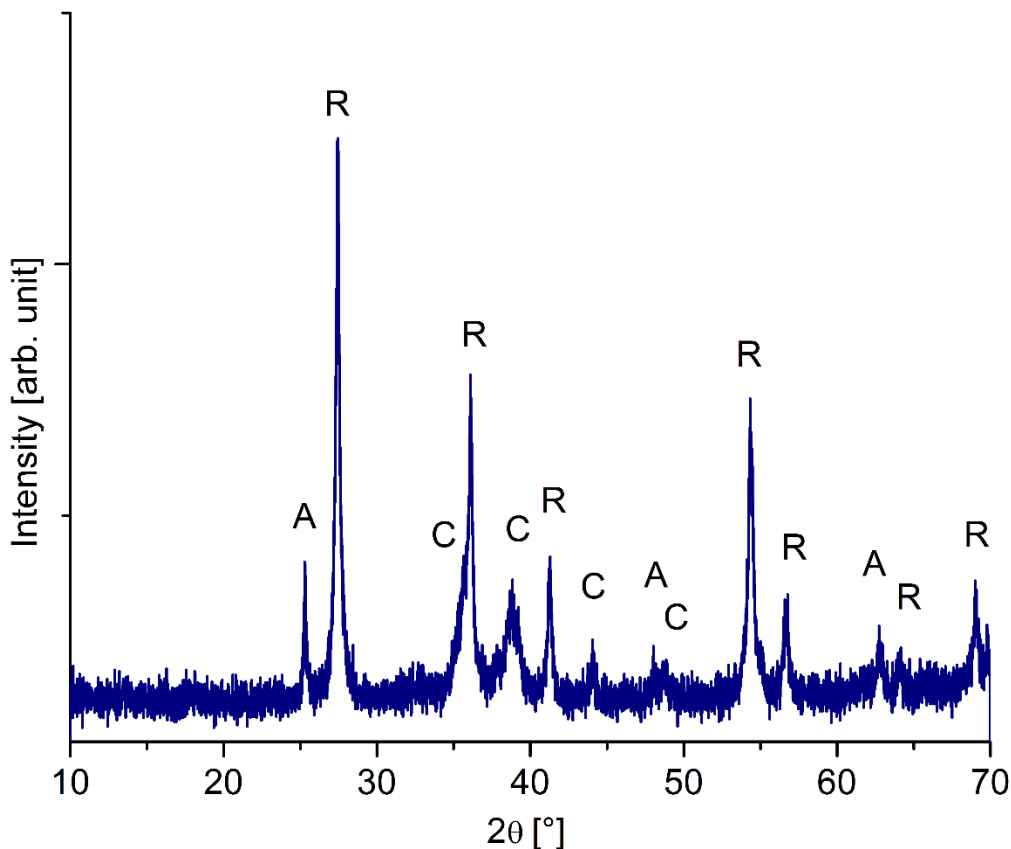
Figure 7.13. XRD pattern for as-produced 25 mol% CuO-TiO_2. (R = Rutile TiO_2, A = Anatase TiO_2, C = Tenorite CuO).

From the XRD pattern and the literature, we can infer the high amount of rutile is a consequence of Cu doping of the TiO_2. While the onset of the anatase to rutile phase transformation typically begins around 600° C, subvalent substitutional dopant cations can be transformation promoters.[41] To ascertain if CuO doping readily decreases the transformation temperature, we prepared sol-gel CuO-TiO_2 powders at a doping level of 5 mol% CuO, well above the solubility limit of CuO in TiO_2. The initially amorphous powders were calcined at 400° C to produce powders that were pure anatase by XRD with no observable CuO phase. No phase attributed to CuO was detected by XRD. Figure **7.14** shows TGA/DTA of the 5 mol% CuO-TiO_2 sol gel powders, with a DTA exotherm peak at 461° C, corresponding to the anatase to rutile transformation. This represents a 140° C

139

reduction in the transformation temperature, which is likely the source of a significant amount of rutile in the as-produced powders.[41]

Other groups have also reported CuO promotion of the anatase to rutile transformation.[42] Substitutional doping of Cu creates oxygen vacancies, as shown in Eq. 2, which tend to oxygen diffusion through the oxygen sublattice necessary for the reconstructive anatase to rutile transformation.[41]

Equation 6. CuO doping defect reaction

$$CuO \xrightarrow{TiO_2} Cu''_{Ti} + V_O^{\bullet\bullet} + O_O$$
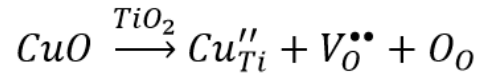
Earlier in this chapter, it was established that flame residence time does not affect the rutile:anatase ratio in LF-FSP TiO_2, but in this case, CuO doping is likely the cause of the high rutile content in the as-produced powders. The anatase to rutile transformation may happen in the flame, but could also occur in the ESP at temperatures of 300° C for 1 h and may be seeded by rutile phase in the as-produced powder.
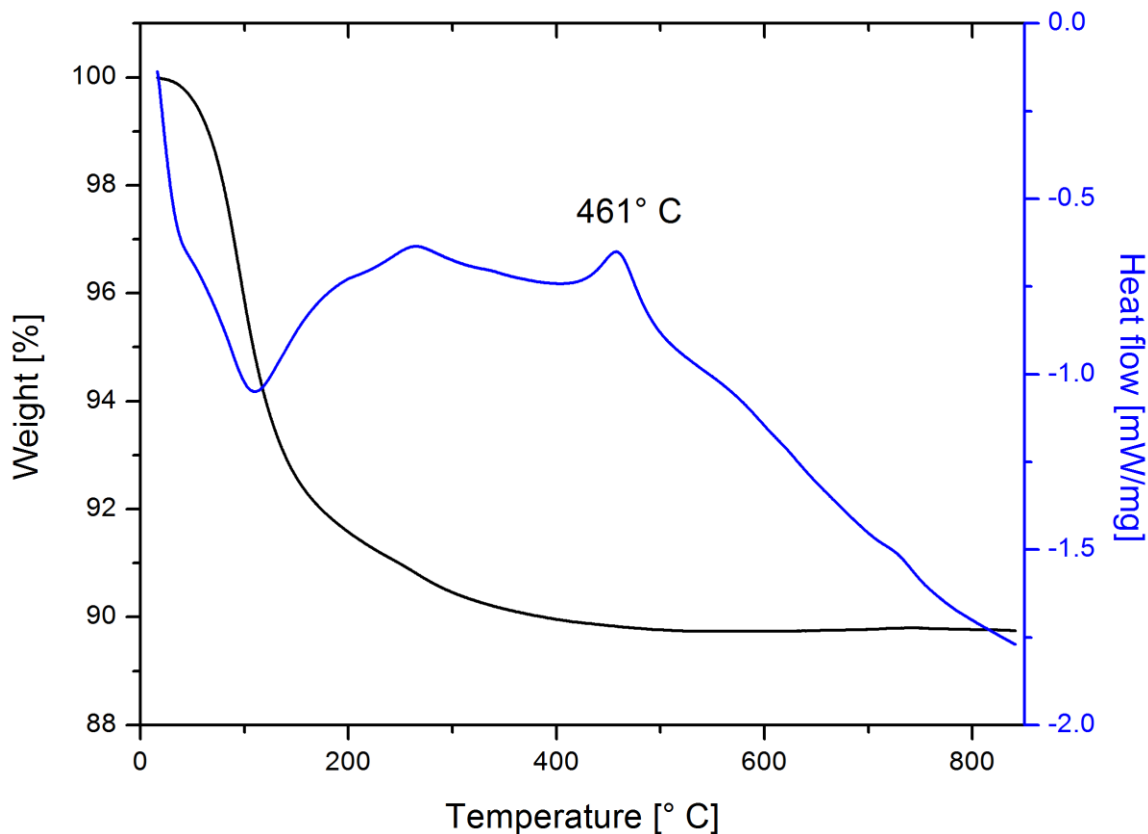
Figure 7.14. TGA/DTA for sol-gel 5 mol% $CuO\text{-}TiO_2$.

The as-produced powders were studied by TEM to ascertain the particle morphology. Figure **7.15** shows TEM images of $CuO\text{-}TiO_2$ composite particles. Unlike the $WO_3\text{-}TiO_2$ particles, the $CuO\text{-}TiO_2$ particles appear to be nanocomposite nanoparticles. The (200) rutile and (111) tenorite d-spacings are 2.30 and 2.32 Å, respectively, so lattice spacings cannot be used to specify individual crystallites in HRTEM. The majority of particles exhibit the nanostructured nanoparticle morphology, with both CuO and TiO_2 phases likely present in the same particle. These results are similar to that of the $YAG\text{-}Al_2O_3\text{-}ZrO_2$ particles seen in Chapter 4, and suggest that this is the default morphology for multi-phase LF-FSP particles.
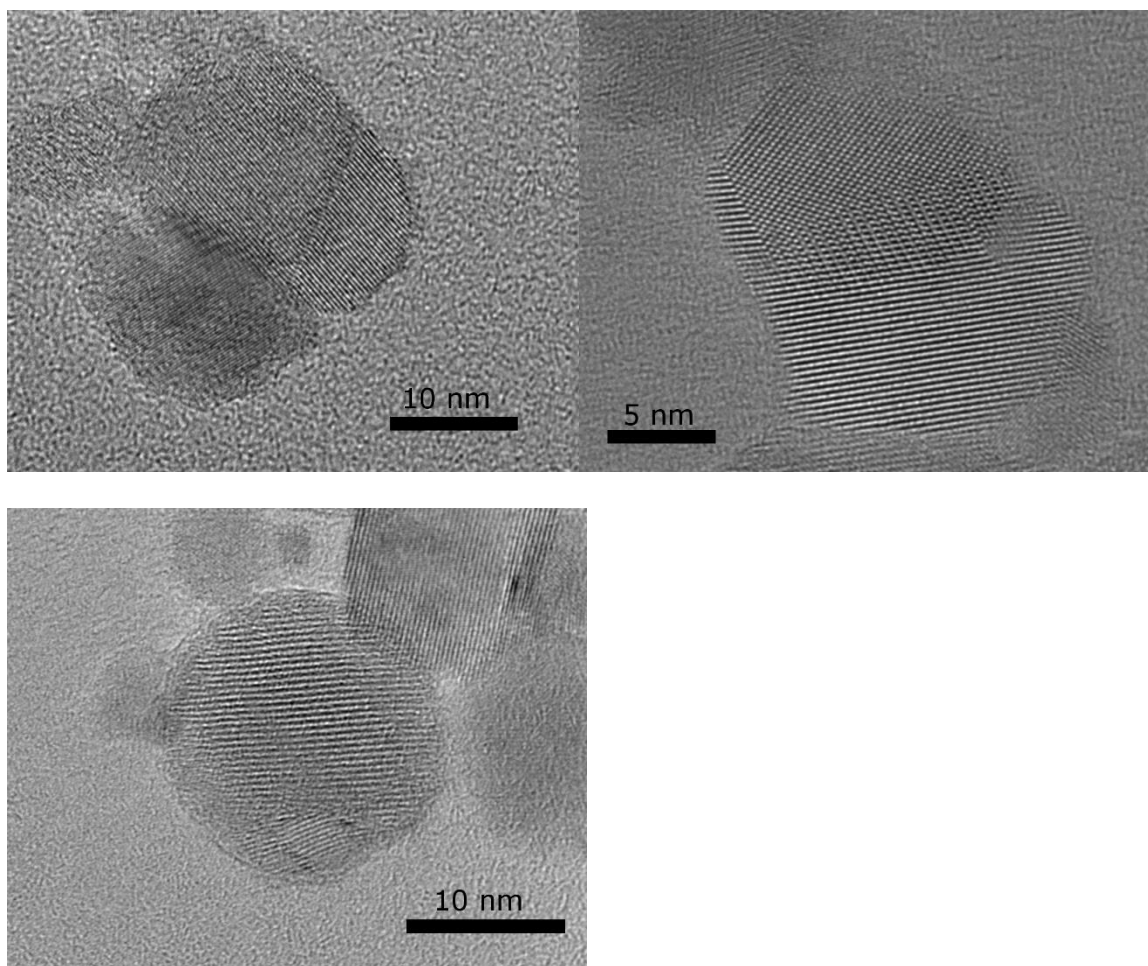
Figure 7.15. TEM images of 25 mol% CuO-TiO$_2$ particles.

XPS compositional analysis coupled with Rietveld refinement provide data summarized in Table **7-9**. The XPS composition closely matches that of the XRD, unlike the core-shell WO$_3$-TiO$_2$, which supports the nanostructured nanoparticle morphology seen by TEM.

Table 7-9. Compositional data for 25 mol% CuO-TiO$_2$ in wt% by XRD and XPS.

	CuO	TiO$_2$
XRD	31±2	69±2
XPS	28±20	72±20

Since the precursors are dissolved in a stirred alcohol solution, we assume complete chemical mixing of the precursors. Once the precursors are injected into the turbulent flame, a good distribution of the molecular species in the gas phase is assumed, which would make discrete particles of separate phases unlikely. Unlike WO_3-TiO_2, where WO_3 had a significant vapor pressure at 1800 K, CuO has a vapor pressure of 1.6E-2 Pa at 1800 K.[43] Although this value is well above the TiO_2 vapor pressure of 6.0E-7 Pa at 1800 K, the vapor pressure is low enough that CuO shell formation is not seen.[39]

Both TEM and XPS suggest that LF-FSP CuO-TiO_2 nanoparticles form as nanostructured nanocomposites. This is in contrast to the WO_3-TiO_2 system, where core-shell particles form as a result of the high vapor pressure of WO_3. Typical gas-phase TiO_2 has a anatase to rutile ratio of 88:12, where the CuO-TiO_2 composite nanopowders have an anatase to rutile ratio of 8:92. We attribute the high amount of rutile to Cu doping of the anatase, which lowers the rutile transformation temperature. The particles may transform in the flame or in the sustained 300° C heat of the electrostatic precipitators.

7.4 Conclusions

Mapping of LF-FSP flame temperature shows that the temperature is largely independent of the heat of the solvent combustion, and peak flame temperatures agree with adiabatic flame temperatures for the alcohols studied here. Increasing alcohol chain length increases total flame length. As a consequence, at constant concentration conditions, particle sizes increase with total flame length due to longer flame residence time. The most important finding that increasing residence time has little effect on nanopowder phase in LF-FSP. This demonstrates that regardless of LF-FSP conditions, one can expect similar phase nanopowders to be produced. This suggests all conditions tested are still within a

kinetic envelope, and that while thermodynamic surface energies may be a factor in nanopowder phase, they do not appear to control phase selection in LF-FSP. MD simulations of the in-flame particle nucleation and growth mechanisms proved too difficult, but generalized force fields for metal oxides developed in the course of the study hold promise for future modeling.

In this chapter, we also demonstrated that the WO_3-TiO_2 system creates particles with a TiO_2 core and WO_3 shell. The core-shell claim is backed up by TEM and composition measurements by XPS. This particle morphology is likely a direct consequence of the high vapor pressure of the WO_3. Additional studies on CuO-TiO_2 show the system produces nanocomposite nanopowders, similar to those seen for Al_2O_3-$YAlO_3$-YSZ particles in Chapter 5. Future work should focus on photocatalytic testing of the WO_3-TiO_2 and CuO-TiO_2 composite nanoparticles.

Regardless of the morphology, we have demonstrated several composite particle systems in which individual particles contain interfaces of various materials. These hold promise for novel properties due to the interfaces contained within the Janus-type particles. From a synthesis standpoint, we have shown that LF-FSP offers single-step synthesis to a variety of nanostructured nanoparticles, which may be difficult to achieve via solution based synthesis techniques.

References

[1]. C.R. Bickmore, K.F. Waldner, R. Baranwal, T. Hinklin, D.R. Treadwell, and R.M. Laine, "Ultrafine titania by flame spray pyrolysis of a titanatrane complex," *Journal of the European Ceramic Society*, **18** [4] 287–297 (1998).

[2]. R. Baranwal, M.P. Villar, R. Garcia, and R.M. Laine, "Flame Spray Pyrolysis of Precursors as a Route to Nano-mullite Powder: Powder Characterization and Sintering Behavior," *Journal of the American Ceramic Society*, **84** [5] 951–961 (2001).

[3] J. Marchal, T. John, R. Baranwal, T. Hinklin, and R.M. Laine, "Yttrium Aluminum Garnet Nanopowders Produced by Liquid-Feed Flame Spray Pyrolysis (LF-FSP) of Metalloorganic Precursors," *Chem. Mater.*, **16** [5] 822–831 (2004).

[4] T. Hinklin, B. Toury, C. Gervais, F. Babonneau, J.J. Gislason, R.W. Morton, and R.M. Laine, "Liquid-Feed Flame Spray Pyrolysis of Metalloorganic and Inorganic Alumina Sources in the Production of Nanoalumina Powders," *Chem. Mater.*, **16** [1] 21–30 (2004).

[5] M.J. Mayo, "Processing of nanocrystalline ceramics from ultrafine particles," *International Materials Reviews*, **41** [3] 85–115 (1996).

[6] I.-W. Chen and X.-H. Wang, "Sintering dense nanocrystalline ceramics without final-stage grain growth," *Nature*, **404** [6774] 168–171 (2000).

[7] M. Kim, T. R. Hinklin, and R.M. Laine, "Core−shell Nanostructured Nanopowders along $(CeO_x)_x(Al_2O_3)_{1−x}$ Tie-Line by Liquid-Feed Flame Spray Pyrolysis (LF-FSP)," *Chem. Mater.*, **20** [16] 5154–5162 (2008).

[8] B. Weidenhof, M. Reiser, K. Stöwe, W.F. Maier, M. Kim, J. Azurdia, E. Gulari, E. Seker, *et al.*, "High-Throughput Screening of Nanoparticle Catalysts Made by Flame Spray Pyrolysis as Hydrocarbon/NO Oxidation Catalysts," *J. Am. Chem. Soc.*, **131** [26] 9207–9219 (2009).

[9] M. Kim and R.M. Laine, "One-Step Synthesis of Core−Shell $(Ce_{0.7}Zr_{0.3}O_2)_x(Al_2O_3)_{1−x}$ $[(Ce_{0.7}Zr_{0.3}O_2)@Al_2O_3]$ Nanopowders via Liquid-Feed Flame Spray Pyrolysis (LF-FSP)," *J. Am. Chem. Soc.*, **131** [26] 9220–9229 (2009).

[10] M. Kim and R.M. Laine, "Liquid-feed flame spray pyrolysis (LF-FSP) for combinatorial processing of nanooxide powders along the $(ZrO_2)_{(1-x)}(Al_2O_3)_x$ tie-line. Phase segregation and the formation of core-shell nanoparticles," *J. Ceram. Proc. Res.*, **8** [2] 129-136 (2007)

[11] A. Kudo and Y. Miseki, "Heterogeneous photocatalyst materials for water splitting," *Chem. Soc. Rev.*, **38** [1] 253–278 (2008).

[12] J.E. Yourey, J.B. Kurtz, and B.M. Bartlett, "Water Oxidation on a $CuWO_4$–WO_3 Composite Electrode in the Presence of $[Fe(CN)_6]^{3−}$: Toward Solar Z-Scheme Water Splitting at Zero Bias," *J. Phys. Chem. C*, **116** [4] 3200–3205 (2012).

[13] F. Riboni, L.G. Bettini, D.W. Bahnemann, and E. Selli, "WO_3–TiO_2 vs. TiO_2 photocatalysts: effect of the W precursor and amount on the photocatalytic activity of mixed oxides," *Catalysis Today*, **209** 28–34 (2013).

[14] K.R. Reyes-Gil and D.B. Robinson, "WO$_3$-Enhanced TiO$_2$ Nanotube Photoanodes for Solar Water Splitting with Simultaneous Wastewater Treatment," *ACS Appl. Mater. Interfaces*, **5** [23] 12400–12410 (2013).

[15] K.K. Akurati, A. Vital, J.-P. Dellemann, K. Michalow, T. Graule, D. Ferri, and A. Baiker, "Flame-made WO$_3$/TiO$_2$ nanoparticles: Relation between surface acidity, structure and photocatalytic activity," *Applied Catalysis B: Environmental*, **79** [1] 53–62 (2008).

[16] K. Lalitha, G. Sadanandam, V.D. Kumari, M. Subrahmanyam, B. Sreedhar, and N.Y. Hebalkar, "Highly Stabilized and Finely Dispersed Cu$_2$O/TiO$_2$: A Promising Visible Sensitive Photocatalyst for Continuous Production of Hydrogen from Glycerol:Water Mixtures," *J. Phys. Chem. C*, **114** [50] 22181–22189 (2010).

[17] Z. Jin, X. Zhang, Y. Li, S. Li, and G. Lu, "5.1% Apparent quantum efficiency for stable hydrogen generation over eosin-sensitized CuO/TiO$_2$ photocatalyst under visible light irradiation," *Catalysis Communications*, **8** [8] 1267–1273 (2007).

[18] J. Bandara, C.P.K. Udawatta, and C.S.K. Rajapakse, "Highly stable CuO incorporated TiO$_2$ catalyst for photocatalytic hydrogen production from H$_2$O," *Photochem. Photobiol. Sci.*, **4** [11] 857–861 (2005).

[19] J.J. Cruywagen, L. Kruger, E.A. Rohwer, "Molybdenum (VI) and Tungsten (VI) Complex Formation. Part 5. The Reaction with Lacate in 1.0 mol dm^{-3} Sodium Chloride Medium," *J. Chem. Soc. Dalton Trans.*, **1** 105-109 (1993)

[20] J.A. Azurdia, "Processing and Synthesis of Multi-metallic Nano Oxide Ceramics via Liquid-feed Flame Spray Pyrolysis"; Ph.D. Thesis. University of Michigan, Ann Arbor, MI 2009

[21] S. Torii, T. Yano, and Y. Tsunoda, "Adiabatic Flame Temperature and Specific Heat of Combustion Gases," *Kagoshima University Research Report*, **34** 1-15 (1992)

[22] J. Chao and F.D. Rossini, "Heats of Combustion, Formation, and Isomerization of Nineteen Alkanols.," *J. Chem. Eng. Data*, **10** [4] 374–379 (1965).

[23] I. Levin and D. Brandon, "Metastable Alumina Polymorphs: Crystal Structures and Transition Sequences," *Journal of the American Ceramic Society*, **81** [8] 1995–2012 (1998).

[24] P. Zhang, A. Navrotsky, B. Guo, I. Kennedy, A.N. Clark, C. Lesher, and Q. Liu, "Energetics of Cubic and Monoclinic Yttrium Oxide Polymorphs: Phase Transitions, Surface Enthalpies, and Stability at the Nanoscale," *J. Phys. Chem. C*, **112** [4] 932–938 (2008).

[25] B. Buesser and S.E. Pratsinis, "Design of Nanomaterial Synthesis by Aerosol Processes," *Annual Review of Chemical and Biomolecular Engineering*, **3** [1] 103–127 (2012).

[26] A. Ahmed, P. Elvati, and A. Violi, "Size-and phase-dependent structure of copper (II) oxide nanoparticles," *RSC Adv.*, **5** [44] 35033–35041 (2015).

[27] L. Pohl, A. Ahmed, P. Elvati, N.J. Taylor, R.M. Laine, and A. Violi, "Molecular dynamics investigation of the structure of Al_2O_3 nanoparticles," Unpublished manuscript (2015).

[28] L.L.Y. Chang, M.G. Scroger, and B. Phillips, "High-temperature, condensed-phase equilibria in the system Ti-W-O," *Journal of the Less Common Metals*, **12** [1] 51–56 (1967).

[29] R. Diehl and G. Brandt, "The Crystal Structure of Triclinic WO_3," *Acta. Cryst.*, **34** 1105-1111 (1978).

[30] W. Li, P. Da, Y. Zhang, Y. Wang, X. Lin, X. Gong, and G. Zheng, "WO_3 Nanoflakes for Enhanced Photoelectrochemical Conversion," *ACS Nano*, **8** [11] 11770–11777 (2014).

[31] M. Righettoni and S.E. Pratsinis, "Annealing dynamics of WO_3 by in situ XRD," *Materials Research Bulletin*, **59** 199–204 (2014).

[32] D.S. Venables and M.E. Brown, "Reduction of tungsten oxides with carbon. Part 1: Thermal analyses," *Thermochimica Acta*, **282–283** 251–264 (1996).

[33] O. Arutanti, T. Ogi, A.B.D. Nandiyanto, F. Iskandar, and K. Okuyama, "Controllable crystallite and particle sizes of WO_3 particles prepared by a spray-pyrolysis method and their photocatalytic activity," *AIChE J.*, **60** [1] 41–49 (2014).

[34] Z.-G. Zhao, Z.-F. Liu, and M. Miyauchi, "Nature-inspired construction, characterization, and photocatalytic properties of single-crystalline tungsten oxide octahedra," *Chem. Commun.*, **46** [19] 3321–3323 (2010).

[35] H. Al-Kandari, F. Al-Kharafi, N. Al-Awadi, O.M. El-Dusouqui, and A. Katrib, "Surface electronic structure–catalytic activity relationship of partially reduced WO_3 bulk or deposited on TiO2," *Journal of Electron Spectroscopy and Related Phenomena*, **151** [2] 128–134 (2006).

[36] S. Saied, J. Sullivan, T. Choudhury, and C. Pearce, "A comparison of ion and fast atom beam reduction in TiO_2," *Vacuum*, **38** [8–10] 917–922 (1988).

[37] P.E. Blackburn, M. Hoch, and H.L. Johnston, "The Vaporization of Molybdenum and Tungsten Oxides," *J. Phys. Chem.*, **62** [7] (1958)

[38] G. Meyer, J.F. Oosterom, and W.J. Van Oeveren, "The Vapor Pressure of Tungsten Trioxide in Gas Mixtures Containing Water Vapour," *Recuil des Travaux Chimiques des Pays-Bas*, **78** 417-423 (1959)

[39] W.O. Groves, M. Hoch, and H.L. Johnston, "Vapor-Solid Equilibria in the Titanium-Oxygen System," *J. Phys. Chem.*, **59** [2] 127-131 (1955)

[40] F.-H. Lu, F.-X. Fang, and Y.-S. Chen, "Eutectic reaction between copper oxide and titanium dioxide," *Journal of the European Ceramic Society*, **21** [8] 1093–1099 (2001).

[41] D.A.H. Hanaor and C.C. Sorrell, "Review of the anatase to rutile phase transformation," *J Mater Sci*, **46** [4] 855–874 (2010).

[42] Y. Iida and S. Ozaki, "Grain Growth and Phase Transformation of Titanium Oxide During Calcination," *Journal of the American Ceramic Society*, **44** [3] 120–127 (1961).

[43] M.W. Chase, Jr., C.A. Davies, J.R. Downey Jr., D.J. Frurip, R.A. MacDonald, and R.A. Syverud, "JANAF Thermochemical Table," *J. Phys. Chem. Ref. Data, Supp.*, **14** [1] (1985).

Chapter 8

Conclusions and future work

8.1   Composites

Chapters 4, 5, and 6 present the synthesis of dense composite structures from both mixed single metal oxide nanoparticles and nanocomposite nanoparticles. One future direction is to increase the number of phases to at least four, at which pinning may dramatically decrease grain sizes into the regime where nano-sized starting materials produce composites with novel properties. Although the composites studied in this work are given a fair amount of attention in the literature, future composites should focus on materials with inherent utility, such as for composites capable of superplastic deformation. The bulk of future work should focus on processing regimes. As we demonstrated, producing high quality nanopowders with a composition close to the desired composition is not as important as it initially seems. Processing factors are likely much more important in producing fine grain sized composites, and future research should focus on processing parameters. Pore size distribution is generally acknowledged as important, but is often overlooked in the processing of nanomaterials. Finally, despite the high quality nanopowders produced by LF-FSP, we have not investigated recently popular sintering methods such as pulsed electric current sintering (PECS), also known as "spark plasma sintering", or microwave sintering. These sintering technologies show great promise for grain size reduction and should be explored using LF-FSP nanopowders.

8.2   Multi-phase particles

In both Chapters 5 and 7, we demonstrate a variety of systems in which multi-phase ceramic particles are produced, with both core-shell and multi-phase polycrystalline morphologies. In the production of such particles, LF-FSP is unique. Namely, LF-FSP offers high production rates (100 g/h) and single step synthesis. Future work should focus on identifying collaborators with advanced characterization equipment that can demonstrate the utility of multi-phase particles produced by LF-FSP. The production of multi-phase particles is one of the most promising aspects of current LF-FSP research. Multi-phase nanoparticles could offer novel catalytic, optical, or electronic properties, and LF-FSP is uniquely positioned to offer a non-solution based route to these particles at high production volumes.

8.3   General directions

A relatively new direction for LF-FSP is the development of lithium battery materials, one in which LF-FSP has demonstrated great promise. In terms of both funding and scientific progress, battery material development should remain the primary focus of LF-FSP research.

During the course of this Ph.D. study, a great amount of research was put into the development of transparent ceramics. High demand exists for domestic sources of high-quality nanopowders for transparent ceramics primarily utilized in military applications. The most important factor in laser-quality nanopowders is extremely low contamination levels. In its current state, LF-FSP is ill-suited for producing extremely pure powders. As a research reactor, many different types of nanopowders are produced, all of which can serve as contaminants. For a research reactor, electrostatic precipitators are much better

than baghouse filters, as many different powders can be collected with limited contamination. However, the current electrostatic precipitator design offers the collection efficiencies which peak at 70% and often dip below 50%. With the cost of rare earths and other transparent ceramic precursors, these losses are significant. Finally, tracking down and eliminating impurities from raw materials or precursor processing is a time-intensive process of limited academic value, and as such, is better left as an industrial exercise.